ISSN 0503-1540

Tome 32 *Novembre 1994* Numéro 4

La mer

うみ

Proceedings of the Seventh Japan and East China Seas Study Workshop, 9-14 May 1993, Qingdao, China

1994 年 11 月

日 仏 海 洋 学 会

La Société franco-japonaise d'océanographie

Tokyo, Japon

Note pour la présentation des manuscrits

La mer, organe de la Société franco-japonaise d'océanographie, publie des articles et notes originaux, des articles de synthèse, des analyses d'ouvrages et des informations intéressant les membres de la société. Les sujets traités doivent avoir un rapport direct avec l'océanographie générale, ainsi qu'avec les sciences halieutiques.

Les manuscrits doivent être présentés avec un double, et dactylographiés, en *double interligne*, et au recto exclusivement, sur du papier blanc de format A4 (21×29,7 cm). Les tableaux et les légendes des figures seront regroupés respectivement sur des feuilles séparées à la fin du manuscrit.

Le manuscrit devra être présenté sous la forme suivante:

1° Il sera écrit en japonais, français ou anglais. Dans le cadre des articles originaux, il comprendra toujours le résumé en anglais ou français de *200 mots* environs. Pour les textes en langues européennes, il faudra joindre en plus le résumé en japonais de *500 lettres* environs. Si le manuscrit est envoyé par un non-japonophone, le comité sera responsable de la rédaction de ce résumé.

2° La présentation des articles devra être la même que dans les numéros récents; le nom de l'auteur précédé du prénom *en entier*, en minuscules; les symboles et abréviations standards autorisés par le comité; les citations bibliographiques seront faites selon le mode de publication: article dans une revue, partie d'un livre, livre entier, etc.

3° Les figures ou dessins originaux devront être parfaitement nettes en vue de la réduction nécessaire. La réduction sera faite dans le format 14,5×20,0 cm.

La première épreuve seule sera envoyée à l'auteur pour la correction.

Les membres de la Société peuvent publier 7 pages imprimées sans frais d'impression dans la mesure à leur manuscrit qui ne demande pas de frais d'impression excessifs (pour des photos couleurs, par exemple). Dans les autres cas, y compris la présentation d'un non-membre, tous les frais seront à la charge de l'auteur.

Cinquante tirés-à-part peuvent être fournis par article aux auteurs à titre gratuit. On peut en fournir aussi un plus grand nombre sur demande, par 50 exemplaires.

Les manuscrits devront être adressés directement au directeur de publication de la Société: Y. YAMAGUCHI, Université des Pêches de Tokyo, Konan 4-5-7, Minato-ku, Tokyo, 108 Japon; ou bien au rédacteur étranger le plus proche: H. J. CECCALDI, EPHE, Station marine d'Endoume, rue Batterie-des-Lions, 13007 Marseille, France; E. D. GOLDBERG, Scripps Institution of Oceanography, La Jolla, California 92093, Etats-Unis; T. ICHIYE, Department of Oceanography, Texas A & M University, College Station, Texas 77843, Etats-Unis; ou T. R. PARSONS, Department of Oceanography, University of British Columbia, Vancouver, B. C. V6T 1W5, Canada.

Preface

The Seventh JECSS (Japan and East China Seas Study)-PAMS (Pacific-Asian Marginal Seas) Workshop was held at Institute of Oceanology, Academia Sinica in Qingdao, China during May 9-14, 1993. The workshop was attended by more than one hundred scientists from China, Korea, Japan, the United States and Russia and as many as seventy-eight papers were presented as shown separately in the workshop program. This volume contains ten papers accepted after at least two rigorous and careful reviews. The editors of the workshop proceedings are thankfull to all revieweres of papers. They would also like to express their gratitude on behalf of all participants at the workshop to Dr. Yunshan QIN, chairman of the Local Organizing Committee, and its members for their warm hospitality. Editors are grateful to Prof. ARUGA for a kind arrangement to publish the Proceedings in this volume.

Kuh KIM
Seoul

Kenzo TAKANO
Tokyo

La mer 32: 225–234, 1994
Société franco-japonaise d'océanographie, Tokyo

A numerical study on currents in the Taiwan Strait during summertime

Sen JAN*, Ching-Sheng CHERN* and Joe WANG*

Abstract : A zonal sand ridge north of the Peng-hu Channel has a strong influence on flows in the Taiwan Strait. Previous summertime hydrographic surveys in this area suggest that lighter surface waters flow over the ridge and then hug the west coast of Taiwan, while heavier bottom waters are blocked upstream of the ridge and turn northwestward along the local isobath.

A three-dimensional baroclinic ocean circulation model is used to study the above mentioned processes. Model results indicate that the flow pattern around the ridge is mainly determined by the bottom topography and the inertia effect associated with the incoming flows. Stratification upstream affects flow patterns downstream of the ridge. As surface waters flow farther north, they tend to converge eastward due to both the baroclinic effect and topographic β-effect. Meanwhile, a wave-like structure in the density field is formed downstream of the ridge. The simulated flow patterns are in close agreement with observations.

1. Introduction

The flows in the Taiwan Strait (TS) are significantly affected by the topography. Fig. 1 shows isobaths in the TS. The major topographic features, as illustrated in this figure, are the Chang-yuen ridge (CYR) north of the Peng-hu Channel (PHC), the Formosa Banks in the southwestern TS, and the deepening topography in the northeastern TS. Past observations suggest that the circulation in the Strait is dynamically complex.

Irrespective of its driving mechanisms, a permanent northeastward flow was observed through PHC to the northern TS (CHUANG, 1985, 1986; WANG *et al.*, 1987, 1988). As this flow impinges on the CYR, the surface and bottom waters will flow in different directions upstream of the CYR, at least during the summer season. Figs. 2a and 2b show isopycnals at 10 m and 50 m depths, respectively, in the TS during September 1–6, 1988. Lighter surface waters, shown in Fig. 2a, may flow over the CYR and distribute along the eastern side of the TS, while heavier bottom waters, shown in Fig. 2b, are blocked and then separated from the Taiwan coast south of the CYR. The vertical density transect at a zonal section (line B in Fig. 2a) indicates that flows are well stratified in the southern PHC, as shown in Fig. 3a. Fig. 3b shows another density transect north of the CYR (line C in Fig. 2a). The original, vertically stratified waters become uniform in the eastern TS and remain stratified in the western TS. Typically, these hydrographic patterns last from May to early September (WANG *et al.*, 1988; WANG and CHERN, 1991, 1992).

The influence of topography on stratified flows has been studied extensively (e.g., HUPPERT and STERN, 1974; MERKINE, 1975, 1976; NOF, 1978). These theoretical analyses indicated that for a rotating stratified flow over a ridge, there will be a streamwise density gradient on the upstream side of the ridge. This density gradient can support a cross-stream vertical shear through the thermal wind relation. Hence the flow will be deflected to the left in front of this ridge at least at lower layers (MERKINE, 1975). This is a possible cause for the observed vertical veering of currents in front of the CYR. However, the topography in the TS is much more complex than that of these theoretical models. The adjustment processes induced by the shoaling topography in the PHC and the blocking of the CYR can magnify nonlinear effects and make the problem analytically intractable.

* Institute of Oceanography, National Taiwan University, Taipei, Taiwan, China

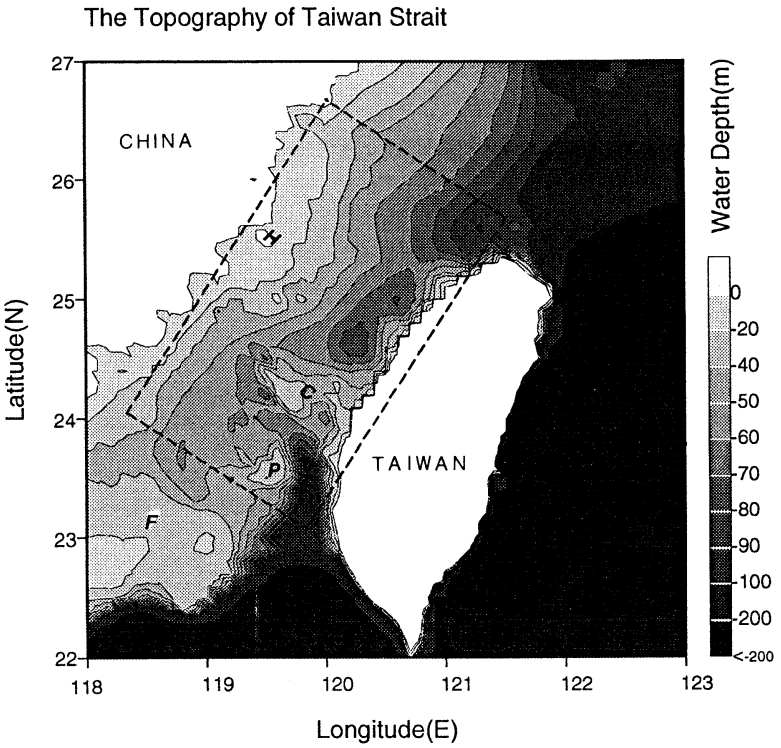

Fig. 1. Bottom topography of the Taiwan Strait, in which *F* is the Formosa Banks, *P* is the Peng-hu Islands, *PHC* is the Peng-hu Channel, *C* is the Chang-yuen ridge and *H* is Hai-tang Island. The dashed rectangle is the computation domain.

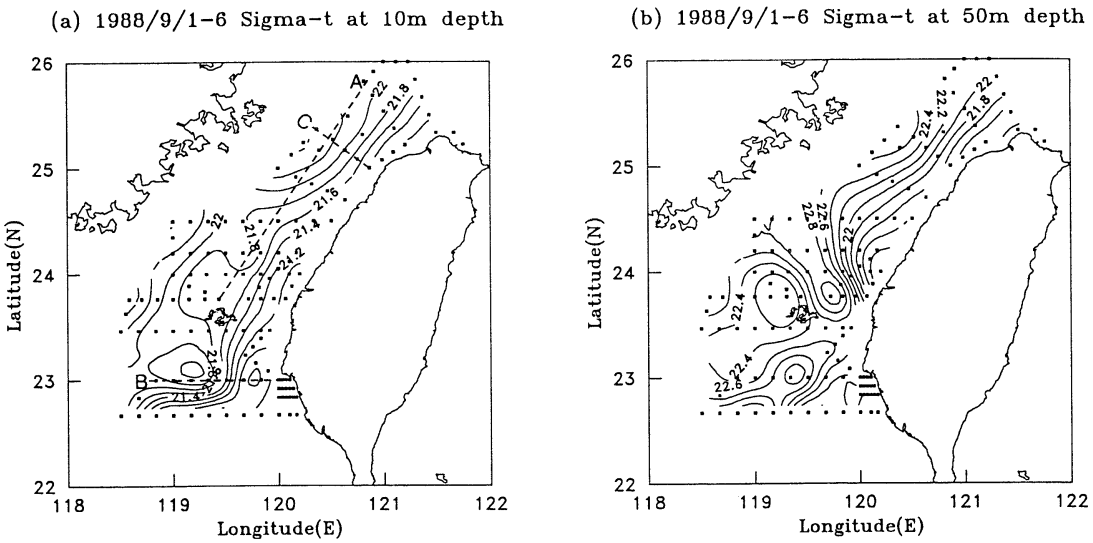

Fig. 2. Isopycnals (in σ_t) at depths 10 m and 50 m observed in the Taiwan Strait during September 1–6, 1988 (from WANG and CHERN, 1992). Dots denote locations of CTD cast.

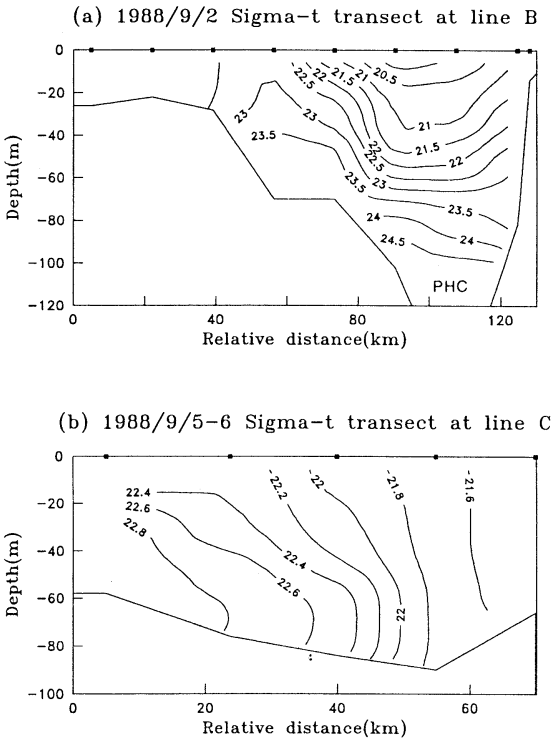

Fig. 3. Vertical density transects at lines B and C in Fig. 2.

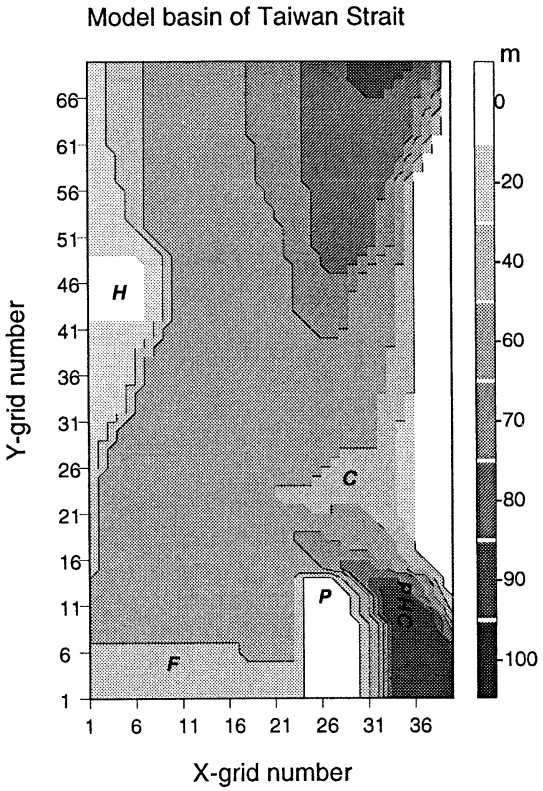

Fig. 4. Model basin of the Taiwan Strait with the same notations as in Fig. 1.

WANG and CHERN (1991) used a homogeneous, frictionless model, similar to the NOF's (1978) formulation, to study the current structure in the CYR area. They found that the Rossby number of the incoming flow is a dominant parameter affecting the flow pattern. As the Rossby number diminishes, the flow will separate from the east coast and turn northwestward. Following their study, a three-dimensional, baroclinic, ocean circulation model is used to investigate the effect of the upstream stratification on the summertime flow pattern in the TS. In order to identify the main mechanism controlling the flow field, the model ocean has a topography which resembles that of the TS. Influences of the stratification and inertia of the incoming flow are discussed.

2. Numerical model

The ocean general circulation model described by SEMTNER (1974, 1986) is used to study the summertime circulation in the TS. The dashed rectangle shown in Fig. 1 indicates our computation domain. For convenience, the x-axis is transverse to the Strait and the y-axis aligned along the Strait, which is about 32° clockwise from north. Fig. 4 shows the model basin, which retains essential features of the bottom topography of the TS. The model basin has 40 and 70 grid points in the x and y directions with a mesh size of 5 km. There are seven levels in the vertical with the level thickness being 20 m for the top three levels, reduced to 10 m for the lower four levels to better resolve the steep rise near the northern end of the PHC.

Under the Boussinesq, hydrostatic and rigid-lid approximations, the governing equations are as follows

$$\frac{Du}{Dt} - fv = -\frac{1}{\rho_0} P_x + \nu u_{zz} + A_M \nabla_H^2 u$$

$$\frac{Dv}{Dt} + fu = -\frac{1}{\rho_0} P_y + \nu v_{zz} + A_M \nabla_H^2 v$$

$$P_z = -\rho g$$

$$u_x + v_y + w_z = 0,$$

in which x, y, z form a right-handed Cartesian coordinate system with $z = 0$ at the sea surface and u, v, w are velocity components in the three directions respectively, t is time, P is pressure, ρ is density, ρ_0 is a reference density, f is Coriolis parameter, D/Dt is total time derivative, ∇_H is horizontal gradient operator, A_M and ν are horizontal and vertical eddy viscosities. For simplicity, the density diffusion equation is considered in the present model as,

$$\frac{D\rho}{Dt} = \nu\rho_{zz} + A_H\nabla_H^2\rho,$$

in which A_H is horizontal diffusivity.

Variables are calculated at the center of each grid box.

WANG and CHERN (1991) showed that the flow pattern around the CYR is mainly determined by the volume transport through the PHC. Unfortunately, there are no comprehensive current measurements in this channel. The actual transport in the PHC is still not clear. However, we can estimate the transport with current data acquired by CHUANG (1986). Since the observed near-bottom (80 m depth) flow is typically 30 cm/s northward in summer, the upper layer flow should be faster than this. Thus, a reasonable estimate of the vertically averaged velocity is 50 cm/s northward. We further assume that the current is 20 km wide and 100 m thick; a volume transport of about 1 Sv (10^6 m^3/s) is thus used to spin up the model. This value is the same as the total volume transport through the TS estimated by WYRTKI (1961). On the other hand, the observed hydrography (XIAO, 1988) shows that isotherms and isohalines on the Formosa Banks are nearly transverse to the Strait. Moreover, images of sea surface temperature and ocean color (LIU, 1993) also show that surface waters flow mostly through the PHC into the TS. The above evidences imply that the transport across the Formosa Banks is quite small. So the net transport through the southwestern boundary is specified zero.

The model ocean is quiescent and homogeneous initially. According to the density structure shown in Fig. 3a, a simplified two-layer, with a pycnocline at level 3, stratified flow is clamped at the entrance of the PHC. The northward transport in the PHC is gradually increased to 1 Sv during the first 10 days and then levels off. The zero normal gradient boundary condition for the density and horizontal velocity is imposed at the northern and southwestern open boundaries. At the rigid surface, $z = 0$,

$$\frac{\partial\rho}{\partial z} = 0, \quad w = 0, \quad \tau_s = 0,$$

in which τ_s is sea surface stress. Since the vertical level size is too coarse to resolve the bottom boundary layer, a quadratic stress law and density flux boundary conditions are used on the ocean floor, $z = -h(x, y)$,

$$\frac{\partial\rho}{\partial z} = 0,$$
$$(\tau_b^x, \tau_b^y) = C_d(u^2 + v^2)^{1/2}(u, v),$$

where τ_b is bottom stress, C_d is friction coefficient. The vertical velocity on the uneven bottom is $w = uh_x + vh_y$. The normal component of momentum and density fluxes are zeros on all solid walls. Numerical integration time step is 60 seconds and other parameters are $A_M = 2 \times 10^6$ cm^2/s, $\nu = 1$ cm^2/s, $A_H = 2 \times 10^5$ cm^2/s, and $C_d = 0.001$. In the present model, A_M and ν are assumed as small as possible provided the computation remains stable. It is hoped that this choice may reduce the frictional effect and make the model to be inertia dominant. Thus we can mainly examine the interaction between the topography and the inertia effect. In order to absorb the computational disturbances generated on the open boundary, a sponge layer is formed at 3 grid points adjacent to the northern boundary, where the horizontal eddy viscosity is 2, 4 and 8 times as large as the above A_M.

3. Model results

Two cases, SA and SB, with different stratification conditions for flows at the entrance of the PHC are considered in this study. Densities (σ_t) at levels 1 and 2, 3, and 4 to 7 at the open boundary south of the PHC are 21, 22.5 and 24 in case SA, and 21, 21.15 and 21.3 in case SB. A useful nondimensional parameter measuring stratification strength is the Burger number,

$$S = g\frac{\Delta\rho}{\rho}\frac{H}{f^2L^2},$$

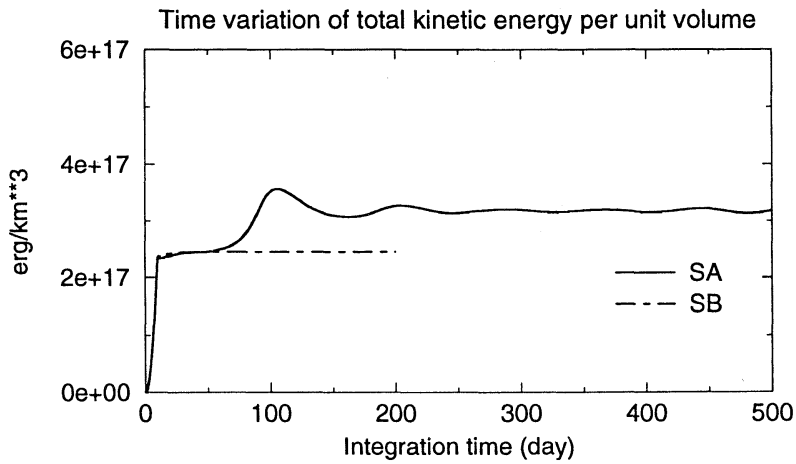

Fig. 5. Time variation of the total kinetic energy per unit volume (km^3) for cases SA and SB during the integration period.

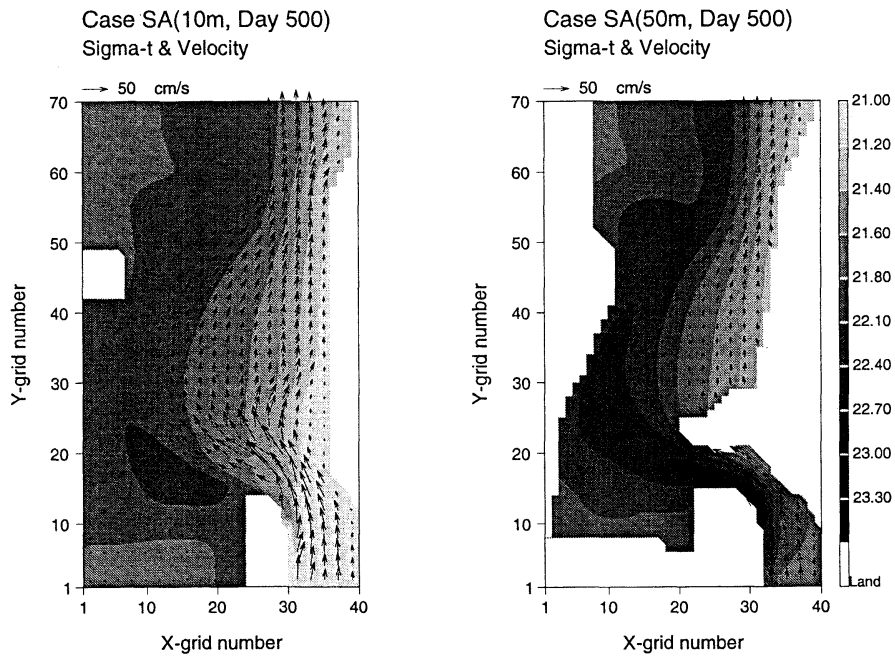

Fig. 6. Distribution of velocity and density (in σ_t) at 10 m and 50 m depths in case SA at day 500. Velocity vectors are plotted at every two grid points in both the x and y directions.

in which L is horizontal length scale of the topography rise and $\Delta\rho$ is density difference over the vertical length scale H. For fixed geometric scales, H = 60 m and L = 25 km, the Burger number is proportional to the density difference over H. So the Burger number in cases SA and SB is estimated 0.9 and 0.09, respectively, with $g = 9.8\ m^2/s$ and $f = 5.5 \times 10^{-5}\ s^{-1}$. The typical Burger number is around 1 in the PHC during summer.

Fig. 5 shows the time variation of the total kinetic energy per unit volume (km^3) during the integration period. This figure indicates that integration time needed to get a quasi-steady

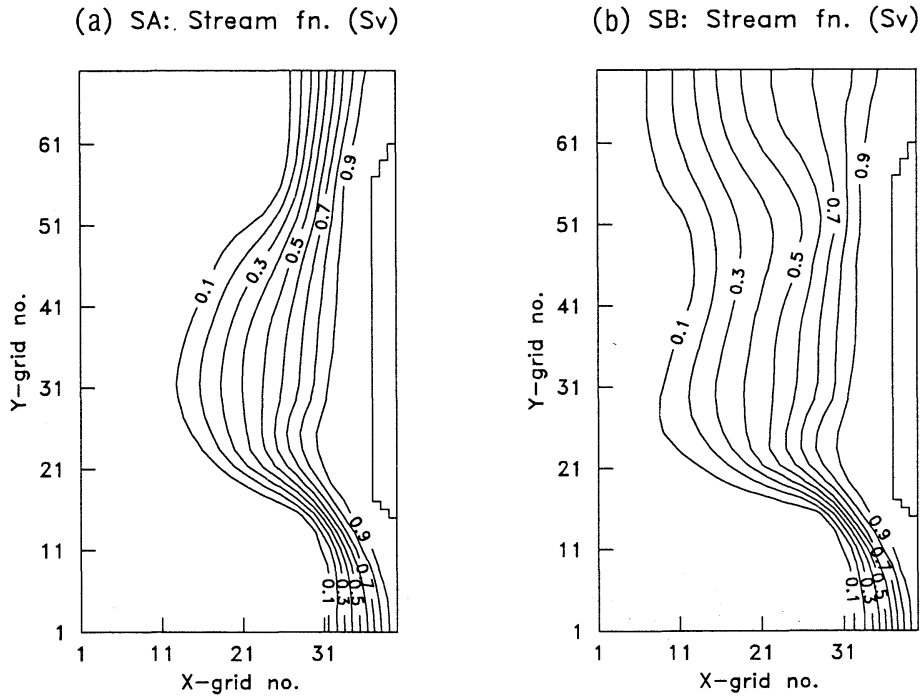

Fig. 7. Transport stream lines in cases SA and SB.

state is 350 days for SA and merely 100 days for SB. The strong baroclinicity is a possible cause for case SA to take a longer time.

There is no significant variation in flow fields after these 350 or 100 days.

Fig. 6 shows the horizontal distributions of velocity and density at 10 m (surface) and 50 m (bottom) depths in case SA at day 500. At the surface, the flow with a speed of about 25 cm/s at the entrance of the PHC is accelerated to about 50 cm/s as it reaches the northern end of the PHC. As surface waters flow over the CYR, a negative relative vorticity will be produced on the ridge due to the potential vorticity conservation associated with the shoaling topography. Thus, a stagnant region is formed in the nearshore area west of Taiwan. In the northern TS, surface flows gradually converge eastward to the Taiwan coast. The average velocity here is about 40 cm/s which is of the same order as that measured by WANG *et al.* (1988). Flows are relatively weak at the western portion of the Strait. Bottom flows, on the other hand, behave differently. The heavier waters upwelled from the lower layer of the PHC are deflected northwestward forming a cold water tongue to the northwest of the CYR. These bottom waters then flow by the western boundary to the northern TS, where the mean velocity is about 5 cm/s.

The flow pattern in the area south of the CYR in case SB is similar to that in case SA, but shows a different feature in the northern TS. Fig. 7 shows the distribution of stream lines in these two cases. In case SB, stream lines tend to move westward in the northern TS, as shown in Fig. 7; and so are isopycnals (not shown). This is inconsistent with the observed hydrography shown in Fig. 2. In case SA, however, the convergence of the transport streamlines in the northwestern TS is apparent. Theoretically, for a stratified rotating flow over a ridge, the vertical shear of the cross-stream velocity in front of the ridge depends on the upstream Burger number (MERKINE, 1975; CHERN and WANG, 1990). Since the Burger numbers in both cases are not greater than 1, the flow pattern around the CYR is determined mainly by the local Rossby number, similarly to the homogeneous case studied by WANG and CHERN (1991). However, this

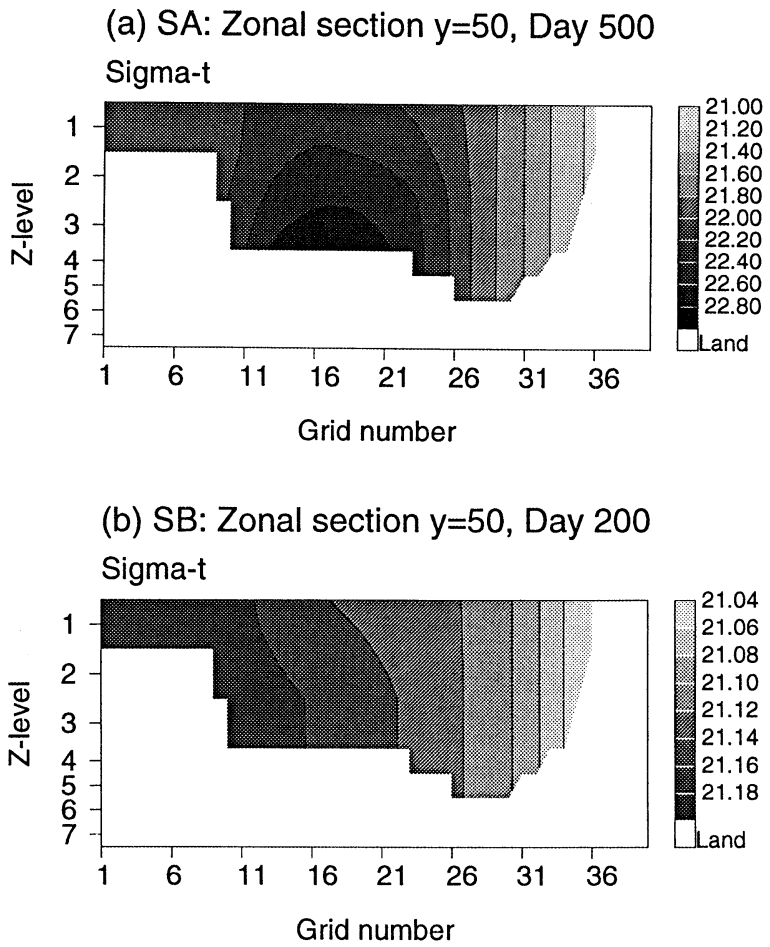

Fig. 8. Vertical density transect in cases SA and SB at the zonal section $y = 50$.

does not mean that the upstream stratification has no effect on the flow structure at all. North of the CYR, the original vertical stratification is transformed into a cross-stream density front. Fig. 8 shows vertical density transects at the zonal section $y = 50$ in cases SA and SB. Waters are vertically uniform in the eastern part and stratified in the western part of the northern TS in both cases. The thermal wind relation indicates that a larger cross-stream density gradient in case SA may induce a stronger streamwise vertical shear within the frontal region. Since this horizontal density front is in the eastern part of the northern TS, the intensification and convergence of flows here in case SA are partly due to this process. Furthermore, the deepening topography in this area relating to the topographic β-effect will also enhance the above mentioned process.

4. Discussion and concluding remarks

In addition to the mean flow pattern described in previous sections, we can also identify a wave-like structure in the density field downstream of the CYR. Fig. 9 shows density transects at the meridional section $x = 21$ in the two cases. The wave-like pattern is apparent in case SA and is relatively weak in case SB. According to model results, lighter surface waters subside immediately north of the CYR as bottom flows turn northwestward in front of this ridge. In the northern TS, the stratified waters

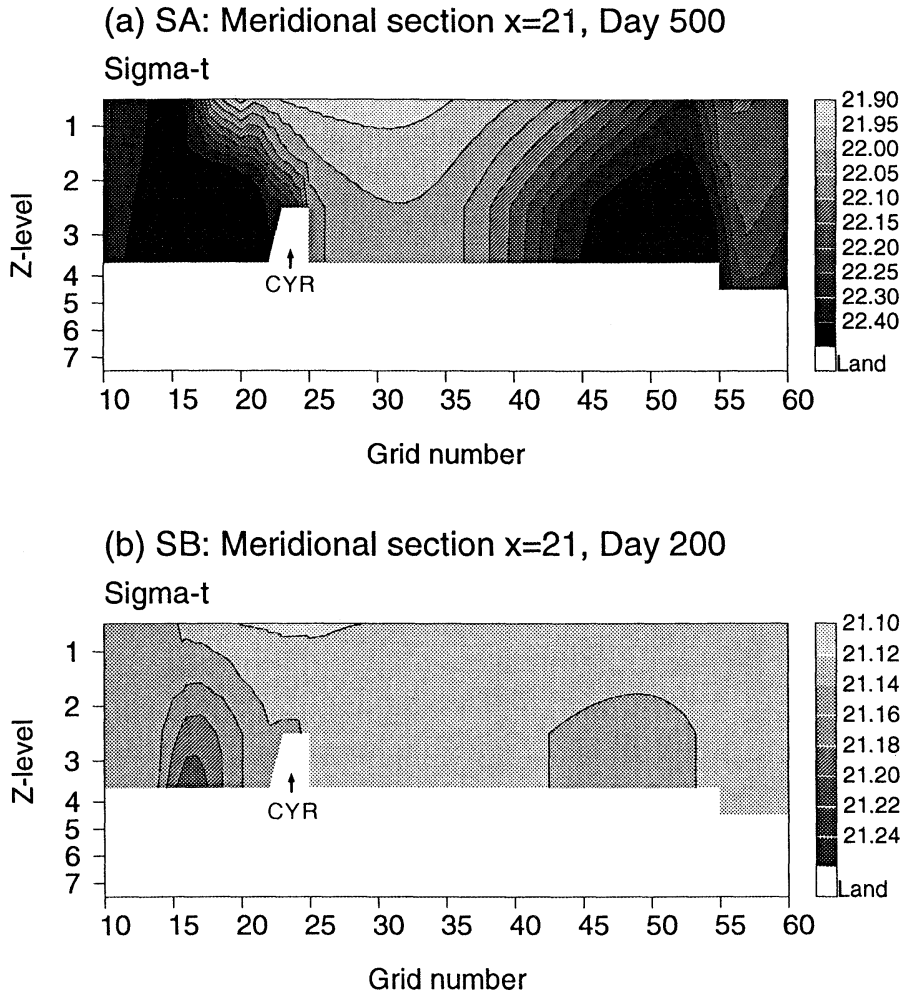

Fig. 9. Vertical density transects in cases SA and SB at the meridional section $x = 21$.

in the western portion of the Strait are pushed eastward due to the thermal wind relation and the topographic β-effect, as mentioned in a previous section. Hence, a wave-like pattern is formed in the center of the Strait. This kind of density structure has also been observed along the central line of the Strait, as shown in Fig. 10, which is the density transect at line A in Fig. 2. The resemblance of isopycnals distribution between this figure and case SA in Fig. 9 is clear. The formation of this density structure and its relation to the upstream stratified condition need further study.

Since tidal currents are strong in the Strait, the bottom Ekman layer associated with the frictional stresses may also affect the flow pattern. Different frictional coefficients have been used in our model to study this effect. With C_d increase, model results indicate that transport streamlines tend to move westward in the northern TS. However, for C_d in the range from 0.001 to 0.005, there is no appreciable difference among the modeled flow fields. Since there is insufficient information about the frictional strength in the TS, and the simulated flow patterns shown previously are in good agreement with the observed hydrography, we may say that the parameter values used in the present model are reasonable.

To summarize, this model study verifies that

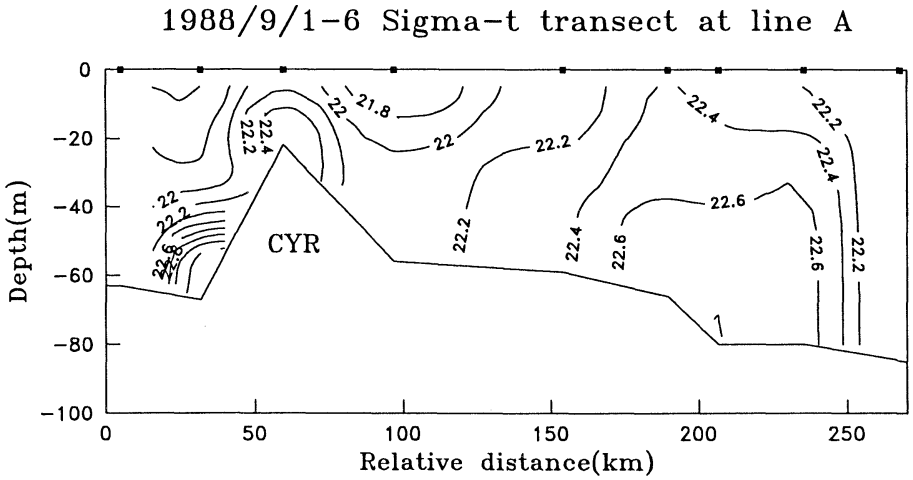

Fig. 10. Vertical density transect at line A in Fig. 2a.

the summertime flow pattern in the Strait is determined by the bottom topography, the stratification and volume transport in the southern entrance of the PHC. Due to shoaling at the northern end of the PHC, surface waters are accelerated and then flow over the ridge. Meanwhile, bottom waters are blocked south of the CYR and flow northwestward following the local isobaths. After surface and bottom waters veered in front of the ridge, original vertically stratified waters are transformed to be uniform in the eastern portion and stratified in the western portion of the northern TS. For the upstream Burger number of about 1, the above transformation related to the baroclinic effect together with the topographic β-effect can enhance downstream flows toward the Taiwan coast. In the central part of the TS, a wave-like density structure is formed north of the CYR.

References

CHERN, C.-S. and J. WANG (1990): On the Kuroshio branch current north of Taiwan. Acta Oceanogr. Taiwanica, **25**, 55–64.

CHUANG, W.-S. (1985): Dynamics of subtidal flow in the Taiwan Strait. J. Oceanogr. Soc. Japan, **41**, 65–72.

CHUANG, W.-S. (1986): A note on the driving mechanisms of current in the Taiwan Strait. J. Oceanogr. Soc. Japan, **42**, 355–361.

HUPPERT, H.E., and M.E. STERN (1974): Ageostrophic effects in rotating stratified flow. J. Fluid Mech., **62**, 369–385.

LIU, A.K. (1993): Satellite remote sensing for ocean application. Conference on Marine Meteorology Proceedings, Central Weather Bureau, Taipei, 177–188.

MERKINE, L.-O. (1975): Steady finite-amplitude baroclinic flow over long topography in a rotating stratified atmosphere. J. Atmos. Sci., **32**, 1881–1893.

MERKINE, L.-O. and K.-R. EUGENIA (1976): Rotating stratified flow over finite isolated topography. J. Atmos. Sci., **33**, 908–922.

NOF, D. (1978): On geostrophic adjustment in sea straits and wide estuaries: Theory and laboratory experiments. Part I: One-layer system. J. Phys. Oceanogr., **8**, 690–702.

SEMTNER, A.J. (1974): An oceanic general circulation model with bottom topography. Numerical simulation of weather and climate. Tech. Rep. 9, Dept. of Meteorology, UCLA, 99 pp.

SEMTNER, A.J. (1986): Finite difference formulation of a world ocean model. Proceedings of the NATO Advanced Study Institute on Advanced Physical Oceanographic Numerical Modelling, ed. J. J. O'BRIEN, D. Reidel Publishing Co., Dordrecht.

WANG, J. and C.-S. CHERN (1991): Some aspects on flow-topography interactions in the Taiwan Strait. A process study of subtidal flows on Chang-yuen ridge. International Symposium on Marine Pollution in Celebration of the 60th Anniv. of National Cheng-Kung Univ., 55–67.

WANG, J. and C.-S. CHERN (1992): On the distribution of bottom cold waters in Taiwan Strait during summertime. La mer, **30**, 213–221.

WANG, J., C.-S. CHERN, C.-H. CHEN and Y.-Y.

HUANG (1987): Oceanographic observations and a diagnostic system at the CBK area. Special Pub. No. 53, Institute of Oceanography, National Taiwan University. 192 pp. (in Chinese)

WANG, J., C.-S. CHERN, C.-H. CHEN and Y.-Y. HUANG (1988): Oceanographic observations at CBK-11 area platform and the nearby area. Special Pub. No. 57, Institute of Oceanography, National Taiwan Uuiversity, 279 pp. (in Chinese)

WYRTKI, K. (1961): Physical oceanography of the southeast Asia waters. Scientific results of marine investigations of the South China Sea and Gulf of Thailand, 1959-1961, Naga Report, **2**, 195 pp.

XIAO, H. (1988): Studies of coastal upwelling in western Taiwan Strait. J. Oceanogr. in Taiwan Strait, **7**, 135-142.

La mer 32: 235-244, 1994
Société franco-japonaise d'océanographie, Tokyo

The Kuroshio in the East China Sea and the currents east of the Ryukyu Islands during autumn 1991

Yaochu YUAN[*1], Kenzo TAKANO[*2], Ziqin PAN[*1], Jilan SU[*1], Kazuo KAWATATE[*3], Shiro IMAWAKI[*3], Honghua YU[*1], Hong CHEN[*1], Hiroshi ICHIKAWA[*4] and S. UMATANI[*3]

Abstract: A modified inverse method is used to compute the currents in the East China Sea and to the east of the Ryukyu Islands with moored current meter records and hydrographic data collected during October-November, 1991. The volume transport of the Kuroshio is 27.4, 26.3 and 26.0×10^6m^3/s across three different sections. There are countercurrents east of the Kuroshio. There is a western boundary current, called "Ryukyu Current", east of the Ryukyu Islands. It has two cores of maximum speed east of Okinawa Island. One is located over the area of maximum slope of the bottom. Its maximum velocity is about 20cm/s, (between 500 and 600m levels). The other is located above 200m level further to the east. This current occupies mostly the upper 1400m. Its volume transport is about 21.4×10^6m^3/s east of Iriomotejima and Ishigakijima Islands and 12.4×10^6m^3/s east of Okinawa Island.

1. Introdduction

There have been many studies on the current structure and volume transport of the Kuroshio in the East China Sea. The computation methods used there are dynamic computation method (e.g., GUAN, 1988), diagnostic model (YUAN and SU, 1988), inverse method (e.g., YUAN *et al.*, 1990, 1991), modified inverse method (e.g., YUAN *et al.*, 1992) and prognostic model (YUAN, 1993). The average total volume transport (VT) through section PN in the East China Sea is around 29×10^6m^3/s (YUNA *et al.*, 1993).

In contrast there have been few studies on the western boundary currennt east of the Ryukyu Islands. For simplicity we will call it "Ryukyu Current" (WANG and SUN, 1990). YUAN *et al.* (1990, 1991) pointed out that this northeastward current often has two cores of maximum speed. One is always between 300 and 800m over the area of maximum slope of the bottom, and its maximum velocity was 25cm/s at the 700m level during Sept.-Oct. 1987. The other is located above the 200m level further to the east. Underneath the Ryukyu Current there is a southwestward current. To the east of it there is also a southwestward countercurrent. Probably because hydrographic sections did not extend over the whole Ryukyu Current, the computed volume transport of it showed a large variability with a maximum value comparable to the average VT of the Kuroshio in the East China Sea (YUAN *et al.*, 1993).

In order to inverstigate further the western boundary current on the both sides of the Ryukyu Islands, the first cruise was carried out in October 11 to November 15, 1991, as a part of a cooperative study between Chinese and Japanese scientists. Hydrograhic data were obtained during this cruise. Current meters were deployed to the southeast of Okinawa Island (Fig. 1) in November 1991 and recovered in September 1992. With the 1991 hydrographic data and the current meter records the modified inverse method proposed by YUAN *et al.* (1992) is used to compute the current structures and volume transports on both sides of the Ryukyu Islands.

2. Numerical calculation

First we estimate the order of magnitude of

*1. Second Institute of Oceanography, State Oceanic Administration, P. O. Box 1207, Hangzhou 310012, China.
*2. Institute of Biological Science, University of Tsukuba, 305, Japan.
*3. Research Institute for Applied Mechanics, Kyushu University, Kasuga, 816, Japan.
*4. Faculty of Fisheries, Kagoshima University, Kgosima, 890, Japan.

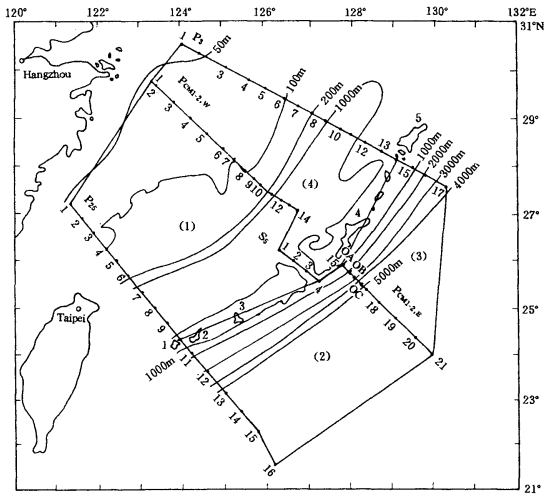

Fig. 1. Bottom topography (in meters), hydrographic sections, mooring stations OA, OB and OC and computation boxes in autumn 1991 (1: Iriomotejima I., 2: Ishigakijima I., 3: Miyakojima I., 4: Okinawa I., 5: Amamioshima I.).

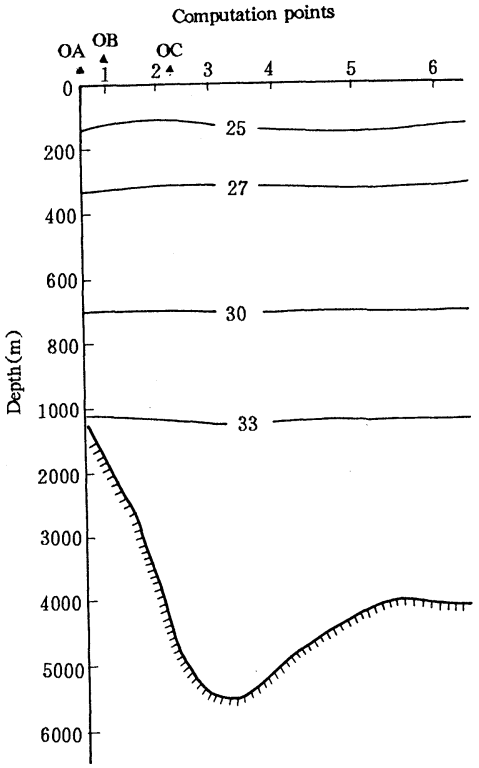

Fig. 2. Isopycnal levels along section PCM1–2E in autumn of 1991.

time change, nonlinear and horizontal eddy (HE) terms in the momentum equations. Based on velocity data obtained by moored current meters, the fluctuation of current on the slope in the East China Sea was found to have a predominant perid of 11–14 days (SUGIMOTO *et al.*, 1988). If the time and space scales T, L and the representative horizontal speed U_0 are taken to be 11 days (9.504×10^5s), 500km, and 1m/s. respectively, the Coriolis parameter f $7\times10^{-5}s^{-1}$, and the horizontal eddy coefficient A_H $10^3m^2/s$, we obtain the Rossby number $R_0=U_0/(fL)=3\times10^{-2}$, the ratio of the time change term to the Coriolis term $(Tf)^{-1}=2\times10^{-2}$, and the ratio of the HE to Coriolis terms $A_H/(fL^2)=10^{-4}$. Thus, the time change, nonlinear and HE terms are negligible in the momentum equations. In addition, previous studies (YUAN and SU, 1983; YUAN *et al.*, 1988) showed the HE term in the momentum equation is negligible, by comparing computed results between two cases, with and without the HE term. Thus, the modified inverse method described in YUAN *et al.* (1992) can be used to compute the current structures and volume transports in the survey area. Four boxes are set up: two in the East China Sea and the other two to the southeast of the Ryukyu Islands (Fig. 1). The computation points are the mid-points between neighboring hydrographic stations. For example, computation point 1 is between hydrographic points 1 and 2. Section S_5 is mostly located at a narrow gap over the Ryukyu Ridge.

All boundary sections of the computation boxes are divided into layers in the vertical according to isopycnal values of $\sigma_{t,p}=25$, 27, 30 and 33 (YUAN *et al.*, 1990). For example, at section PCM1–2E the four isopycnals lie between 130–150m, 330–345m, about 700m and 1200m, respectively (Fig. 2).

The average wind direction and speed observed on board the R/V Shijian were 42° (NE) and 8.6m/s during the autumn cruise in 1991. Because accurate wind data are not available, a steady uniform wind field with these values is assumed. The vertical eddy and diffusion coefficients are $10^{-2}m^2/s$ and $10^{-3}m^2/s$, respectively, for the momentum and density equation (YUAN *et al.*, 1992).

Table 1. Time-averages of the low-passed current velocities during November 1991.

Mooring station	Water depth (m)	Period of averaging	Instrument depth (m)	V (cm/s)	θ	V′ (cm/s)
OA	1000	Nov. 4–11, 1991	570	21.7	66.8°	19.8
		Nov. 4–15, 1991	870	5.0	50.9°	5.0
OB	2020	Nov. 4–30, 1991	1890	4.4	253.0°	−3.8
		Nov. 4–15, 1991	1890	6.0	252.0°	−5.2
OC	4630	Nov. 14–30, 1991	700	10.1	330.4°	3.0
		Nov. 13–30, 1991	2000	4.2	225.0°	−4.2
		Nov. 13–30, 1991	4500	2.6	220.0°	−2.6

V: Speed.
θ: Direction measured clockwise from due the notrh.
V′: Velocity component normal to section PCM1–2E. Positive value: northeastward.

There were three moored stations, OA, OB and OC, located on section PCM1–2E (Fig. 1). Time-averages of low-passed current velocities during November 1991 are listed in Table 1. The period of averaging begins on the starting date of valid records and ends on either the final date of valid records or 30 November 1991 whichever comes earlier. The low-passed currents are rather steady during the periods of averaging (Fig. 3). Fig. 1 shows that stations OA and OC are not located on any computation points. Only station OB is located on computation point 1 at PCM1–2E. In order to discuss the dependence of computed results upon the velocity value prescribd at 1890m depth at OB, two different velocities, −3.8 and −5.2cm/s observed there (Table 1) are used as known values for the computation in two cases, which are referred to as CA–1 and CA–2. In addition, the velocity at 2000m level of computation point 2 (see Fig. 5 (b)) is interpolated from the average velocities observed at 1890m level at OB and 2000m level at OC to get a known value for the computation. Next we set up the third case CA–3, in which the velocity at 1890m depth at OB is unknown and to be obtained from our modified inverse method.

The FIADEIRO and VERONIS's method (1982) is used to determine an optimum reference level. An optimum reference level is obtained to be 2500m in our survey area. For computation points with water depth less than 2500m, the reference levels are reset to the local water depths.

Table 2 shows the results in the three cases in terms of the VT through a western part of P_{25} (points 1 to 9), a western part of P_3 (points 1 to 14) and the other two whole sections. The VT is very little different from each other between the three cases except the VT through PCM1–2E in case CA–3.

The velocity computed in case CA–3 is −1 cm/s and southwestward at 1890m depth at OB, which agrees in direction with the observation at OB but is much smaller than the observed magnitude, −3.8 cm/s or −5.2 cm/s. Since there is almost no difference between cases CA–1 and CA–2, only the result in CA–1 will be discussed below.

3. Velocity distribution during autumn of 1991

Figs. 4 to 7 show the velocity distribution at each section. It might be remarked that both horizontal and vertical scales are different from each other in these figures and that the vertical scale below 1000m is different from that above 1000m in each.

(1) Section P_{25}

Section P_{25} is divided into two parts; northwest of Iriomotejima Island (computation points 1–9) and southeast of it (computation points 10–15).

To the northwest of Iriomotejima Island the Kuroshio core is located over the continental slope (Fig. 4). The velocities are greater than 100 cm/s in the upper 150 m of computation point 6. Its maximum velocity is about 154 cm/s at the surface. Below 500 m level the location of maximum velocity moves eastward to the computation point 7, in agreement with previous studies (YUAN and SU, 1988). The

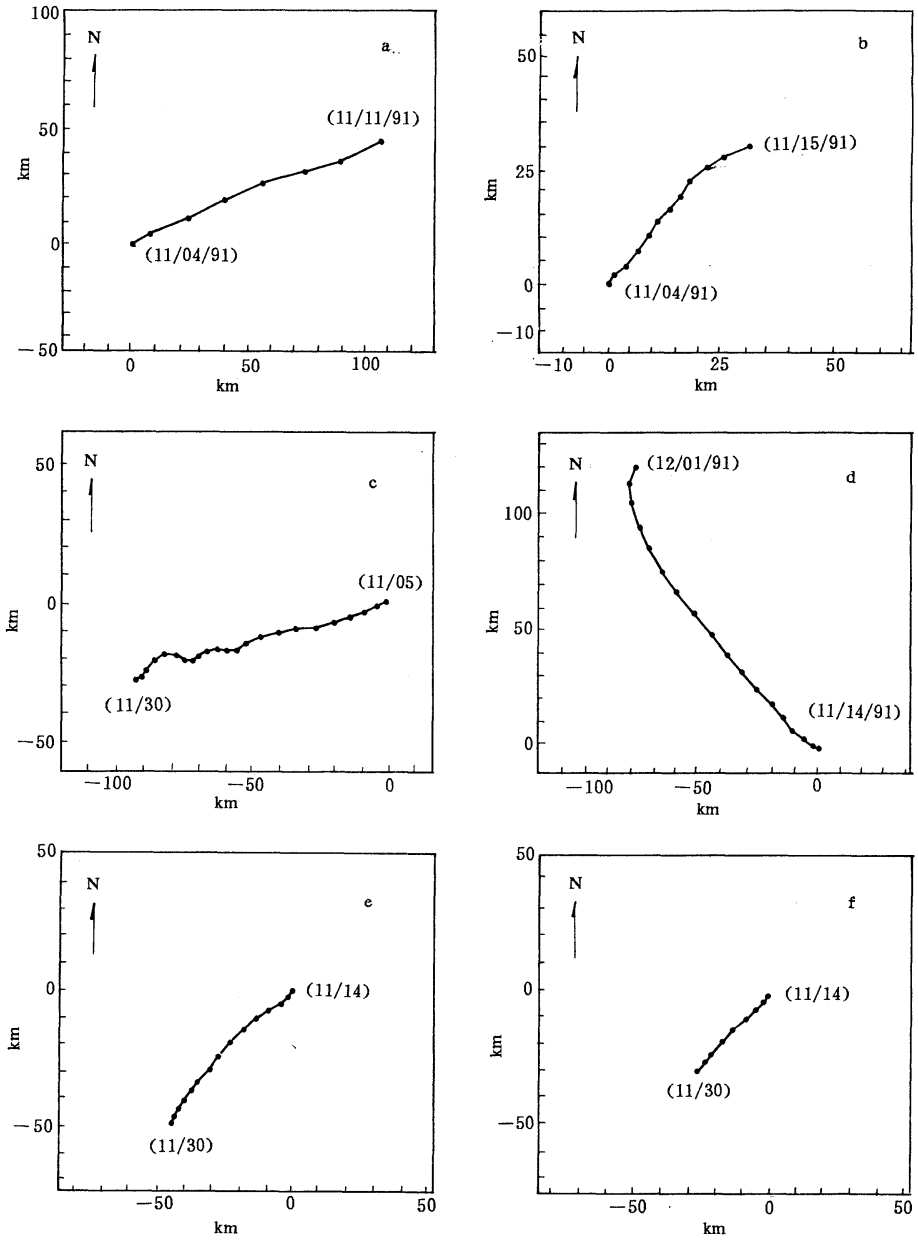

Fig. 3. Progressive vector diagrams of observed daily currents. (a), (b) 570m and 870m depths at OA; (c) 1890m depth at OB; (d), (e), (f) 700m, 2000m and 4500m depths at OC.

countercurrent is to the east of the Kuroshio. Its velocities are not small. The core of this flow lies between 700 and 1000m levels, and maximum velocity is about 21cm/s at 800m level (Fig. 4). There is a cold eddy over the shelf north of Taiwan and west of the Kuroshio, centered at about 122° 14.11′ E, 26° 8.72′ N. The temperature distribution at section P_{25} also depicts its existence, as discussed in previous studies (YUAN *et al.*, 1991). This cold eddy has been documented in many studies (e.g., UDA and KISHI, 1974; FAN, 1980; CHERN *et al.*, 1990). For

Table 2. Volume transports (VT) ($10^6 m^3/s$) through sections. NE: northeastward; SE: southeastward; SW: southwestward.

Cases	Sections					
	P_{25}	PCM1-2W	P_3		PCM1-2E	
	NE	NE	NE	SE	NE	SW
CA-1	27.5	26.1	25.8	−4.2	6.4	−5.8
CA-2	27.4	26.1	25.7	−4.3	6.1	−5.2
CA-3	27.5	26.1	25.8	−4.3	8.3	−6.1

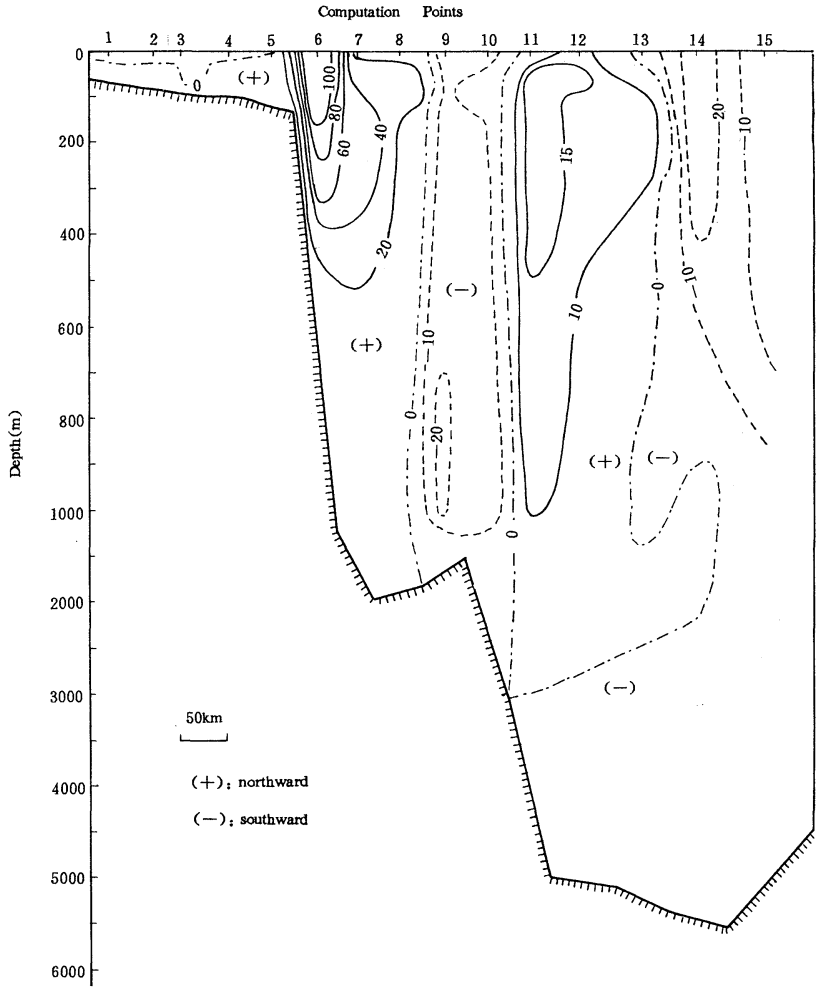

Fig. 4. Velocity distribution at section P_{25} during autumn of 1991. (positive: northeastward, units: cm/s)

example, on the basis of hydrographic data during Sept. 1987, CHERN *et al.* pointed out that next to the Kuroshio there was a distinct cold and high-salinity eddy on the shelf edge with minimum temperatures $<19°C$ and maximum salinities $>34.6‰$.

To the southeast of Iriomotejima Island, there is clearly a northeastward flow, i.e., the Ryukyu Current (Fig. 4). Its core is between 50 and 800m levels, located over the region of

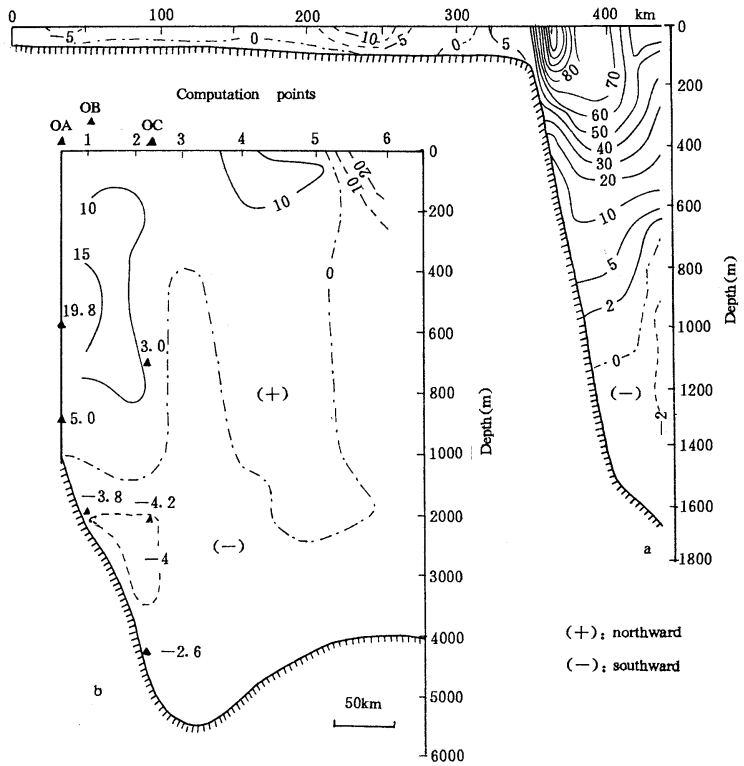

Fig. 5. Velocity distribution during autumn of 1991 at (a) section PCM1–2W, (b) section PCM–12E (positive: northeastward, units: cm/s). ▲ positions of the moorings.

maximum slope of the bottom. Inside this core the velocity varies slightly with depth, from 12 to 19 cm/s. Below this northeastward current the flow is southwestward. There is also a southwestward flow to the east of the Ryukyu Current. Its maximum velocity is close to 30 cm/s at the surface of computation point 14. At computation point 10 there is also a southwestward flow. This shows that flows on both sides of Iriomotejima Island have the same orientation (Fig. 4).

(2) Sections PCM1–2W, PCM1–2E and S_5

Fig. 5(a) shows the velocity distribution at section PCM1–2W. Similarly to section P_{25} the Kuroshio core is over the continental slope. Its maximum velocity is about 136 cm/s at 30m level. In the deeper layer there is a weak southwestward current. The countercurrent often existing east of the Kuroshio is not observed because this section does not extend across the whole Okinawa Trough.

Section PCM1–2E is located southeast of Okinawa Island. Fig.5(b) shows that the greater part of the section is occupied by a northeastward current with two cores of maximum speed. One is between 150 and 800 m levels over the area of maximum slope of the bottom, and its velocity is 16.3 and 16.1 cm/s, respectively, at 500 and 600m levels. The other is located above 200m level further to the east, and its maximum velocity is about 15.2 cm/s at 50m level. The average observed velocity component normal to section PCM1–2E at OA is 19.8 cm/s and 5 cm/s, respectively, at 570 and 870m levels (Table 1 and Fig. 5 (b)). Fig. 5(b) shows that the 570m current meter is in the core with speed greater than 15 cm/s, while the 870m current meter is between isotachs of 10 and 0 cm/s. The computed results agree fairly well with the observed values at OA. They agree with the observed values at OC, too (Fig. 5 (b)). Beneath the Ryukyu Current there is a southwestward flow. It is located below 1000 and 1400m levels

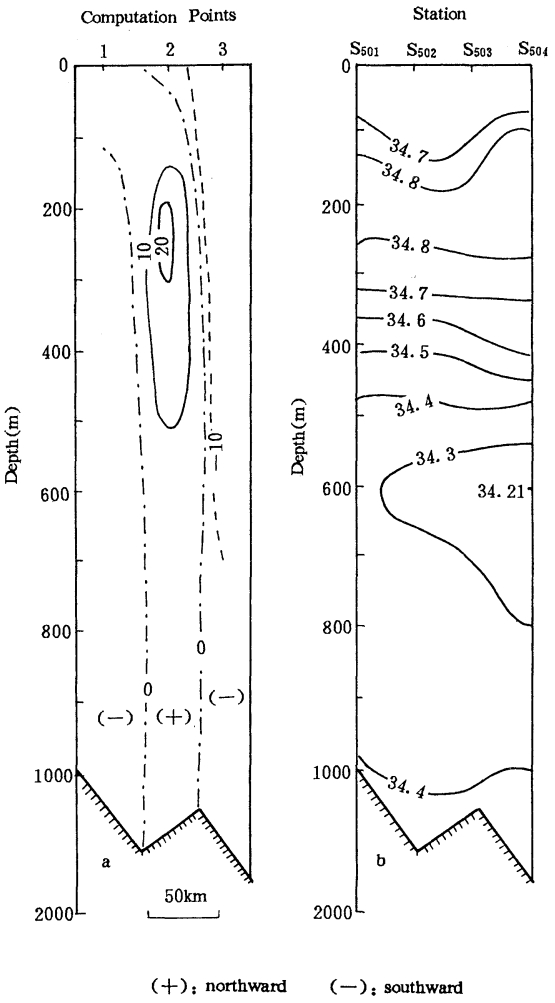

Fig. 6. Velocity (a) and salinity (b) distribution at section S_5 in autumn 1991. (positive: northeastward, units: cm/s and ‰)

at computation points 1 and 2, respectively. Its speed is about 4.2 and 4.1cm/s, respectively, at 2000 m level at computation points 1 and 2. The maximum speed is about 5.2 cm/s at 2500 m level. In the eastern part of section PCM1–2E there is also a southwestward flow, whose velocities are greater than 20 cm/s in the upper 150 m layer.

Finally, we note that the features of currents at section PCM1–2E as discussed above were also obtained at a section southeast of Okinawa Island in September–October, 1987 (YUAN *et al.*, 1990).

The velocity distribution at this section shows that there are southwestward flows at both its west and east ends and a northeastward flow at its central part (Fig.6 (a)). Fig.6 (b) shows that the low salinity water seems to intrude from the east to the west, in agreement with previous studies (Yu *et al.*, 1993).

(3) Section P_3

Section P_3 is divided into two parts (Fig. 1), i.e., the northwestern part (computation points 1–14) in the East China Sea just north of the regular survey line PN, and the southeastern part (computation points 14–17) southeast of Amamioshima Island.

The Kuroshio core at section P_3 is located over the continental slope (Fig.7). Its maximum velocity is about 92 cm/s at 100 m level of computation point 9, which is less than that at section P_{25} and PCM1–2W. Southeast of the Kuroshio there is a southwestward countercurrent. It extends all the way down to the bottom underneath the Kuroshio (Fig.7). Fig.7 also shows the appearance of a northeastward flow at computation point 13, the southeasternmost computation point inside the East China Sea, of which velocity is not large.

The southeastern part of section P_3 southeast of Amamioshima Island is of short length (Fig. 1). Fig. 7 shows a southwestward flow at computation point 15 and a northeastward flow at computation points 14 and 16. These flows all have subsurface cores and the southwestward flow is quite strong, with a maximum velocity of 72 cm/s at 250 m level.

4. Distribution of the volume transport during autumn 1991

Fig. 8 shows the distribution of the total volume transport in the computational region during autumn of 1991. In the East China Sea the net VT through the part of section P_{25} northwest of Iriomotejima Island is about $27.4\times10^6 m^3/s$. There is a core of higher temperatures (Fig. 9) and lower salinities in the deeper layer west of Iriomotejima Island, probably associated with an anticyclonic eddy with a total transport of $11\times10^6 m^3/s$ (Fig. 8). The northeastward VT is about $26.1\times10^6 m^3/s$ through section PCM1–2W, and about $25.8\times10^6 m^3/s$ through the northwestern part of section P_3. The transport of the

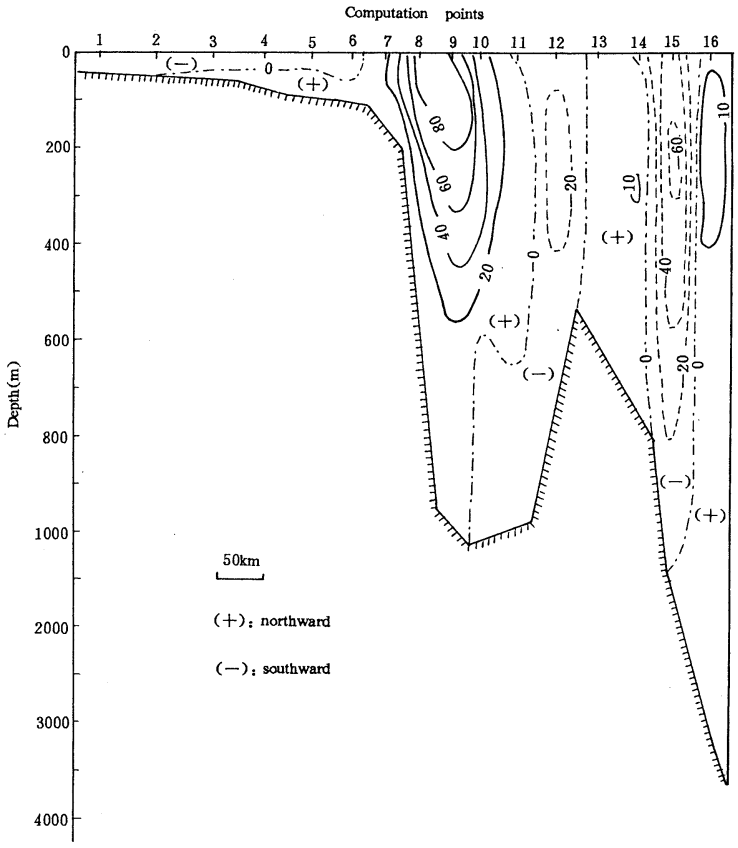

Fig. 7. Velocity distribution at section P_3 during autumn of 1991. (positive: northeastward, units: cm/s).

Kuroshio, i.e., the northeastward current next to the continental shelf of the Est China Sea, is 27.4, 26.3 and $26.0 \times 10^6 m^3/s$, respectively, across sections P_{25}, PCM1–2W and P_3. These values are very close to the transport of the Kuroshio at section PN, $26.0 \times 10^6 m^3/s$, during Oct. 1987 (YUAN *et al.*, 1990). Our computation cannot confirm the gradual decrease in VT along the downstream direction, because section PCM1−2W does not extend across the whole Okinawa Trough, as mentioned before.

In the following we shall discuss the volume transport in the area east of the Ryukyu Islands. Through the eastern part of section P_{25} the northeastward and southwestward total VT are 19.4 and $18.6 \times 10^6 m^3/s$, respectively. The southwestward total VT is divided into two parts; one with $8.9 \times 10^6 m^3/s$ is in the west and the other with $9.7 \times 10^6 m^3/s$ in the east. The VT of the Ryukyu Current, i.e; the northeastward current east of Iriomotejima Island, is $21.4 \times 10^6 m^3/s$. The northeastward and southwestward total VT through section PCM1–2E are 6.4 and $5.8 \times 10^6 m^3/s$. The VT of the Ryukyu Current through section PCM1–2E is $12.4 \times 10^6 m^3/s$ and the VT of the southwestward current beneath it is about $6.0 \times 10^6 m^3/s$.

The VT of the northeastward and southwestward current through section P_3 east of the Ryukyu Islands are 9.1 and $8.2 \times 10^6 m^3/s$, respectively.

There is a net eastward flow through the area between Okinawa and Miyakojima Islands with a VT of about $5.8 \times 10^6 m^3/s$.

5. Summary

Based on moored current meter records and hydrographic data during autumn of 1991, the modified inverse method is used to compute the Kuroshio in the East China Sea and the current

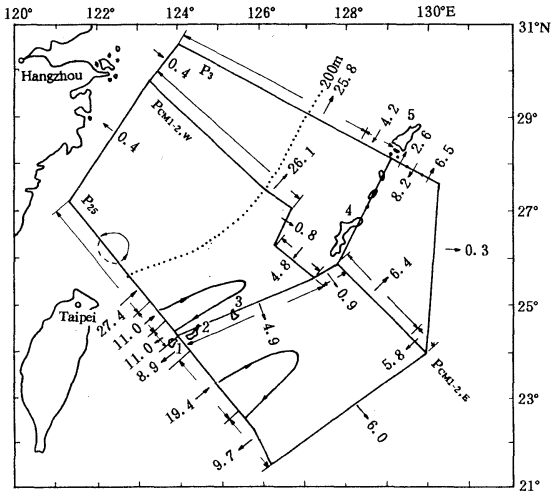

Fig. 8. Distibutions of the total VT during autumn of 1991 (units: $10^6 m^3/s$).

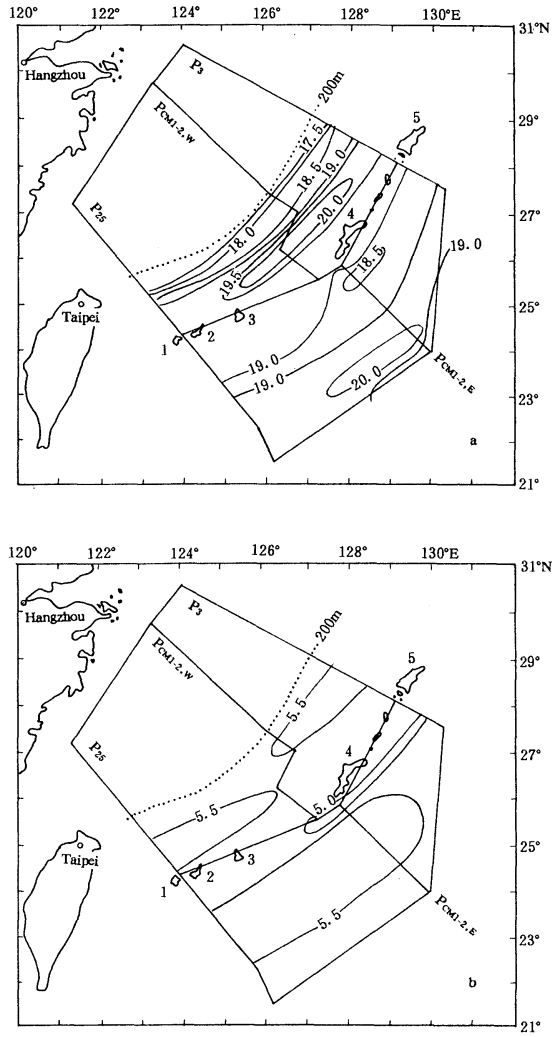

Fig. 9. Temperature distributions in autumn 1991 at (a) 200m level; (b) 800m level.

east of the Ryukyu Islands. It is found that:

1) The Kuroshio core is located over the continental slope. Its maximum velocity is 154, 136 and 92 cm/s, at sections P_{25}, PCM1-2W and P_3, respectively, during this cruise.

2) The transport of the Kuroshio is 27.4, 26.3 and $26.0 \times 10^6 m^3/s$, respectively, across sections P_{25}, PCM1-2W and P_3.

3) Beneath the Kuroshio there is a southwestward countercurrent. Southeast of the Kuroshio there is another countercurrent.

4) East of the Ryukyu Islands there is a western boundary current, called Ryukyu Current. It has two cores of maximum speed at section PCM1-2E. One is located over the area of maximun slope of the ocean bottom. Its maximum velocity is between 500 and 600m levels, and is about 20 cm/s. The other is located above 200m level further to the east.

5) Below the Ryukyu Current the flow is southwestward. Its maximum velocity at section PCM1-2E is about 5.2 cm/s at 2500 m level. There is another southwestward flow east of the Ryukyu Current.

6) The volume transport of the Ryukyu Current through sections P_{25} and PCM1-2E is 21.4 and $12.4 \times 10^6 m^3/s$, respectively.

References

CHERN, C. S., J. WANG and D. P. WANG (1990): The exchange of Kuroshio and East China Shelf Water. J. Geophys. Res., **95**, 16017-16023.

FAN, K. L. (1980): On upwelling off northeastern shore of Taiwan. Acta Oceanogr. Taiwan, **11**, 105-117.

FIADEIRO, M. E and G. VERONIS (1982): On the determination of absolute velocities in the ocean. J. Mar. Res., **40**, suppl., 159-182.

GUAN, B. (1988): Major feature and variability of the Kuroshio in the East China Sea. Chin. J. Oceanol. Limnol., **6**, 35-48.

SUGIMOTO, T., S. KIMARA and K. MIYAJI (1988): Meander of the Kuroshio Front and current variability in the East China Ses. J. Oceanogr. Soc. Japan, **44**, 125-135.

UDA, M. and A. KISHI (1974): Cyclonic cold eddies along the edge of the Kuroshio current in the relation to the genesis and passage of cyclones, I. Waters north of Taiwan. The Kuroshio, Ⅲ. Proceedings of the 3rd Symposium, Bangkok, Thailand, 1972, 199–218.

WANG, Y. and X. SUN (1990): A study on the features of the Ryukyu Current. Proc. Invest. the Kuroshio (Ⅱ), China Ocean Press, Beijing, 237–245.

YU, H., J. SU and Y. MIAO (1994): Low salinity water centre of the Kuroshio in the East China Sea and intrusion of western boundary current east of the Ryukyu Islands. Proc. China Japan Joint Symp. Cooperative Study on the Kuroshio, 27–29 October 1992, Qingdao, China. (in press)

YUAN, Y. (1993): A prognostic model of three dimensional current in the East China Sea. Proc. Invest. the Kuroshio (V). China Ocean Press, Beijing, 311–324.

YUAN, Y., M. ENDOH and H. ISHIZAKI (1990): The study of the Kuroshio in the East China Sea and currents east of the Ryukyu Islands. *In*: Proc. Japan China Joint Symp. Cooperative Study on the Kuroshio, Science and Technology Agency, Japan & SOA, China, 39–57.

YUAN, Y., Z. PAN, I. KANEKO and M. ENDOH (1993): Variability of the Kuroshio in the East China Sea and the currents east of the Ryukyu Islands. Proc. the Kuroshio (V), China Ocean Press, Beijing, 279–297.

YUNA, Y. and J. SU (1983): A two-layer circulation model of the East China Sea. Proceedings of the International Symposium on the Continental Shelf, with special reference to the East China Sea, 364–374.

YUAN, Y. and J. SU (1988): The calculation of Kuroshio Current structure in the East China Sea – early summer. Progress in Oceanogr., **21**, 343–361.

YUAN, Y., J. SU and Z. PAN (1990): Calculation of the Kuroshio Current south of Japan during Dec., 1987–Jan., 1988. Proc. Invest. the Kuroshio (Ⅱ), China Ocean Press, Beijing, 256–266.

YUAN, Y., J. SU and Z. PAN (1991): A study of the Kuroshio in the East China Sea and the currents east of the Ryukyu Islands in 1988. *In*: Oceanography of Asian Marginal Seas. K. Takano, ed., Elsevier Science Publishers, 305–319.

YUAN, Y., J. SU and Z. PAN (1992): Volume and heat transports of the Kuroshio in the East China Sea in 1989. La Mer, **30**, 151–162.

YUAN, Y., J. SU and W. ZHOU (1988): Calculation of the Kuroshio Current south of Japan in May–June 1986. Progress in Oceanogr., **21**, 503–514.

La mer 32: 245–250, 1994
Société franco-japonaise d'océanographie, Tokyo

Spectra of the deep currents southeast of Okinawa Island

Yaochu YUAN[*1], Ziqin PAN[*1], Jilan SU[*1], Shin-ichiro UMATANI[*2], Shiro IMAWAKI[*2], Kazuo KAWATATE[*2] and Kenzo TAKANO[*3]

Abstract: The kinetic energy spectra are shown with three current meter records obtained above the continental slope southeast of Okinawa Island from November 1991 to September 1992. The mean velocity is almost parallel to isobaths except just above the bottom where it is indistinguishable from zero. The eddy kinetic energy is higher than the mean kinetic energy. On most time scales it is higher in the along-isobath than cross-isobath directions. The dominant eddy kinetic energy range shifts toward shorter time scales with increasing depth.

1. Introduction

There are many studies on the low frequency fluctuations with long-term current meter records (e.g., MODE group, 1974; LUYTEN, 1977, 1982; RICHMAN *et al.*, 1977; SCHMITZ, 1978; WUNSCH, 1981; FU *et al.*, 1982; IMAWAKI and TAKANO, 1982). These studies show marked spatial inhomogeneity in properties of the eddy field depending on the depth and geographical location. In the MODE region the mesoscale (20 to 150 days) fluctuations are dominant at 4000m depth, while the secular scale (longer than 150 days) fluctuations are dominant at 500m depth, but at a site near the Gulf Stream in the POLYMODE region the mesoscale fluctuations are dominant at both 600m and 4000m depths (SCHMITZ, 1978). At a deep layer in the western North Pacific, the eddy field is characterized by three time scales; annual scale with zonal dominance of the eddy activity, temporal mesoscale with meridional dominance and monthly scale with horizontal isotropy, and about two thirds of the eddy kinetic energy is contained in the temporal mesoscale (IMAWAKI and TAKANO, 1982). Eddy resolving gyre-scale numerical models (e.g., HOLLAND and LIN, 1975a, b; SEMTNER and CHERVIN, 1992) also show marked spatial inhomogeneity in eddy properties, which seem to be controlled by the eddy-mean flow interaction and the upper, lower and lateral boundary processes.

Three current meter moorings were deployed to the southeast of Okinawa in November 1991 and recovered in September 1992 by the R/V Shijian of the State Oceanic Administration in the framework of a Sino-Japan cooperative study. It is a preliminary step toward clearer understanding of the current structure above the continental slope in the region around the Ryukyu Islands where so far there have been very few long-term current measurements. The present paper describes low frequency fluctuations which other papers (TAKANO *et al.*, 1994; YUAN *et al.*, 1994, 1995) are not concerned with.

2. Velocity data

The locations of three moorings OA, OB and OC are shown in Fig. 1 with the bottom topography. Six time series of velocities from moored current meters (Aanderaa RCM-5) with sampling intervals of one hour were obtained, but usable series longer than one month are only three; at 1890m depth at OB, 2000m and 4500m depths at OC (hereafter abbreviated to OB (1900), OC (2000) and OC (4500)). The details of the current measurements and some results are given in another paper (TAKANO *et al.*, in preparation).

Figure 2 shows stick diagrams of the daily mean deviations of the 25-hour running mean velocities from the velocities averaged over the whole measurement periods at OB(1900), OC

*1 Second Institute of Oceanography, State Oceanic Administration, Hangzhou, 310012 China
*2 Reserch Institute for Applied Mechanics, Kyushu University, Kasuga, 816 Japan
*3 Institute of Biological Sciences, University of Tsukuba, Tsukuba, 305 Japan

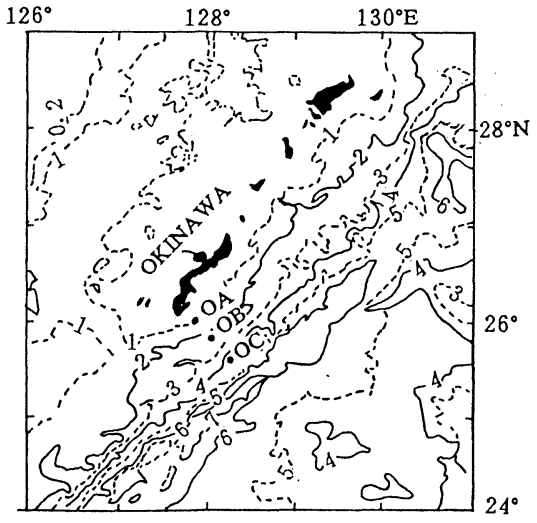

Fig. 1. Locations of moorings OA, OB and OC with bottom topography (depth in km).

(2000) and OC (4500). At OB (1900), the speed and direction of the deviations frequently change with time, except for the first two months when the southwestward deviation is prevailing. The maximum magnitude is smaller than 10 cm/s. It is still smaller at OC(4500) and the direction is more variable than at OB (1900). At OC (2000) the maximum magnitude is more than 10 cm/s. The deviations are better organized, which are directed mostly to the south to southwest in November 1991 and after May 1992, and to the north from December 1991 to April 1992. As expected, they appear to be parallel rather than perpendicular to isobaths.

3. Low frequency fluctuations

Eddy kinetic energy spectra

The Godin filter (GODIN, 1972) suitable for dealing with low frequency fluctuations (IMAWAKI, 1986) is first applied to the data to remove the tidal and inertial oscillations, and then the time series subsampled at intervals of 1 day are analyzed. Table 1 shows statistics of the data after low-pass filtering. On account of topographic directivity at the mooring sites and apparent dominance of the along-isobath component of velocity in Fig.2, the velocity is broken down into two components in the along- and cross-isobath directions (45° and 315° from the north). The eddy kinetic energy of the two components are denoted by subs A and C as K_{EA} and K_{EC}. The mean current is indistinguishable from zero at OB (1900), northeastward with a speed of 2.9 cm/s at OC(2000), and south-southwestward with a speed of 1.3 cm/s at OC (4500). The eddy kinetic energy is much higher than the mean kinetic energy at OB (1900), and about two times larger at OC (2000) and OC (4500).

The raw spectra of the first 256-day records are calculated with FFT and smoothed over four

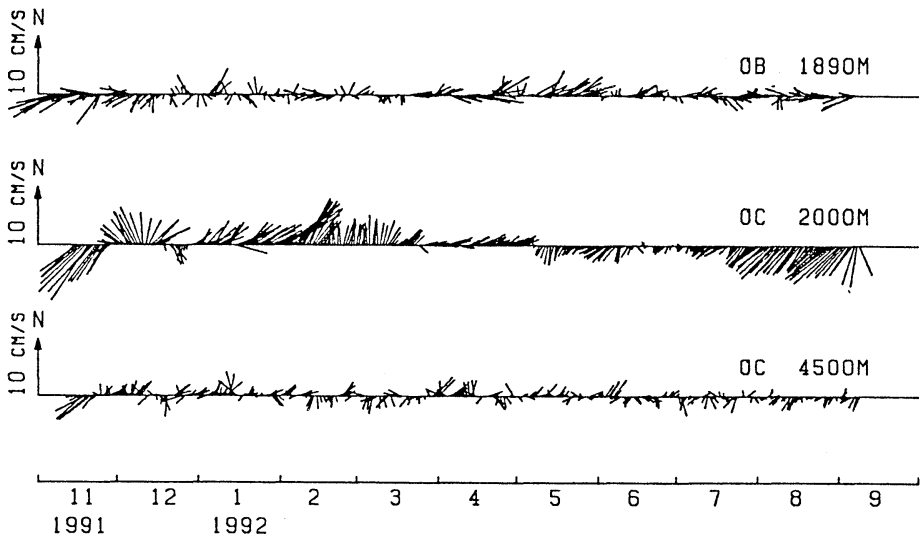

Fig. 2. Stick diagrams of the daily mean deviations at OB (1900), OC (2000) and OC (4500).

Table 1. Along- and cross-isobath components (U,V) of time-average velocity at OB and OC, variances S_U^2, S_V^2, mean and eddy kinetic energies K_M, K_E and the ratio K_E/K_M.

Location		Water depth(m)	Meter depth(m)	Length (days)	U (cm/s)	S_U^2 (cm^2/s^2)	V (cm/s)	S_V^2 (cm^2/s^2)	K_M (cm^2/s^2)	K_E (cm^2/s^2)	K_E/K_M
OB	25°48′ N 128°03′ E	2020	1890	307	−0.03	5.7	0.09	2.9	(0.005)	4.3	(800)
OC	25°34′ N 128°20′ E	4630	2000	298	2.9	18.7	0.08	2.5	4.3	10.6	2.4
			4500	298	−1.2	2.6	−0.7	1.1	0.9	1.8	1.9

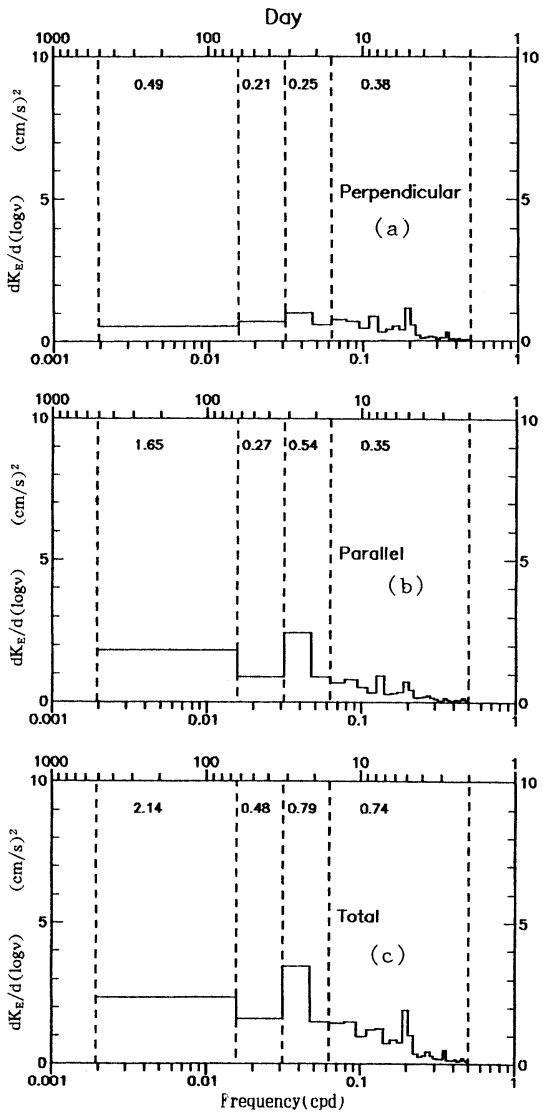

Fig.3. Frequency (ν) spectra for the low-frequency eddy kinetic energy per unit mass at OB (1900) in variance-preserving form. (a) cross-isobath spectrum; (b) along-isobath spectrum; (c) total spectrum.

period bands; 2–16 days, 16–32 days, 32–64 days and 64–512 days. The spectrum freedom is 8. The 95% confidence limits are 0.46 to 3.67 times the individual estimates. The spectra are plotted in variance-preserving form in Figs. 3 to 5, where the energy per unit mass is shown in each period band. Table 2 lists the ratio of the kinetic energy in each band to the total energy integrated over the four bands, and the ratio K_{EA}/K_{EC}.

The upper panel of Table 2 shows that at OB (1900) and OC (2000) more than half of the total eddy kinetic energy is in the band of 64–512 days. While only 3% of the total energy is in the band of 2–16 days at OC (2000), about half of the total energy is in the band of 2–16 days at OC (4500). In IMAWAKI and TAKANO (1982), however, a very small fraction of the total eddy kinetic energy is in the band of 2–16 days at 5000m depth at a site 6200m deep. At OB (1900) where the bottom is 2020m deep, 18% of the total energy is in the band of 2–16 days. The kinetic energy on scales longer than 32 days amounts to 63% of the total energy at OB (1900), 85% at OC (2000) but only 30% at OC (4500). These figures might indicate that the dominant energy range shifts toward shorter time scales with increasing depth, in particular, near the bottom. This agrees with a result by SCHMITZ (1978) in the MODE region, but does not with another result of his at a site near the Gulf Stream.

The lower panel of Table 2 shows that the eddy activity is more enhanced in the along-isobath direction than in the cross-isobath direction except at OB (1900) and OC (2000) in the band of 2–16 days where it is almost isotropic. At OC (2000) far from the sea surface and the bottom, the K_{EA} is monotonically increased with period and much larger than the K_{EC} on time scales longer than 32 days. At OB

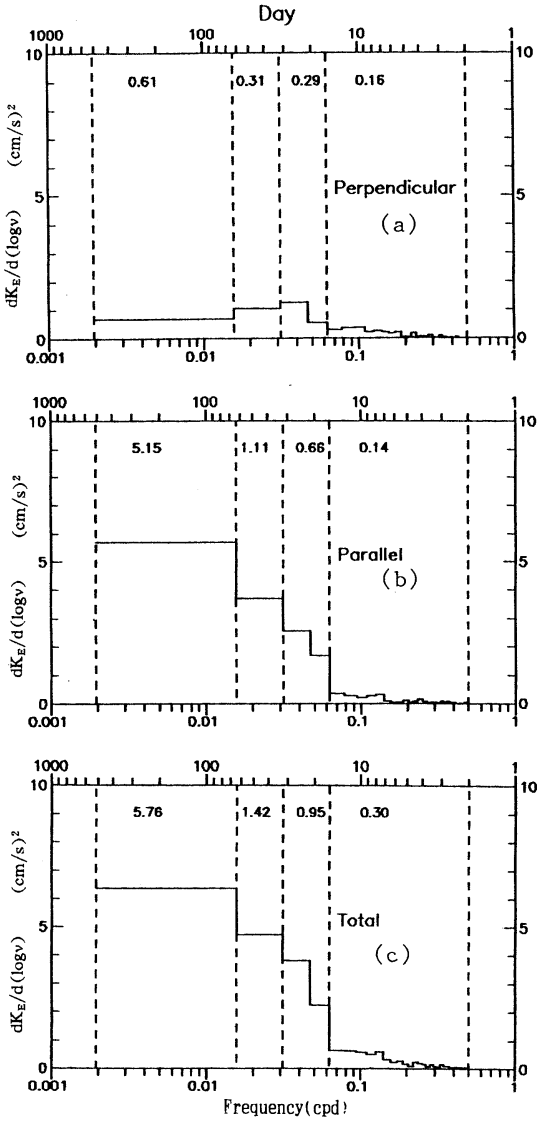

Fig.4. Same as Fig. 3 except for OC (2000).

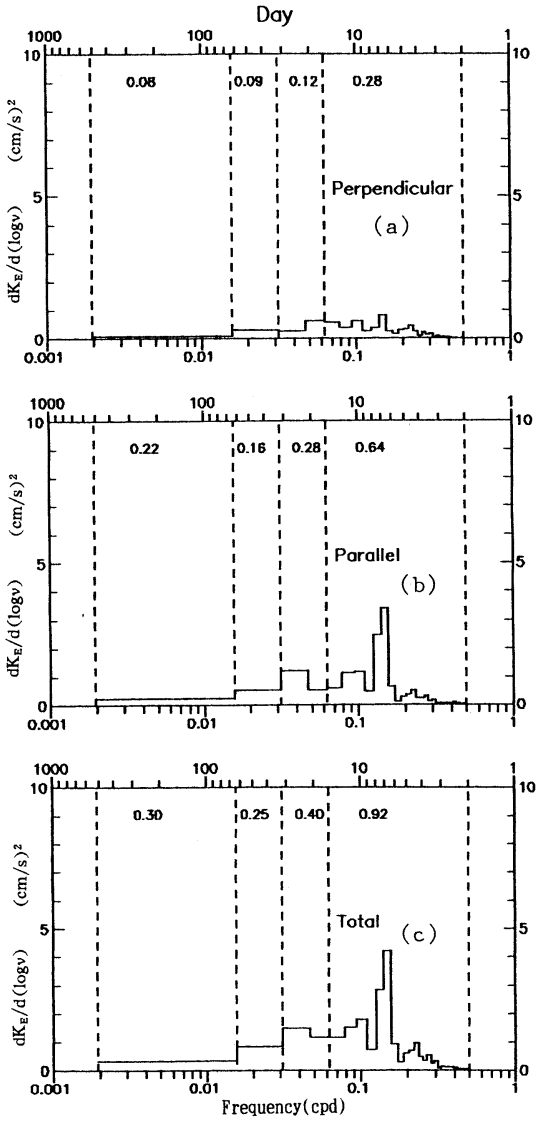

Fig.5. Same as Fig. 3 except for OC (4500).

Table 2. Ratio(%) of the kinetic energy in each period band to the total kinetic energy (upper panel) and ratio K_{EA}/K_{EC} (lower panel).

	Period (days)			
	2–16	16–32	32–64	64–512
OB(1900)	18	19	12	51
OC(2000)	3	11	17	68
OC(4500)	49	21	13	16
OB(1900)	0.92	2.2	1.3	3.4
OC(2000)	0.87	2.3	3.6	8.4
OC(4500)	1.3	2.3	1.8	2.8

(1980) near the bottom, the ratio K_{EA}/K_{EC} at each period band and its increase or decrease with period are similar to those at OC (4500). This suggests the importance of the location relative to the bottom. If both K_{EA} and K_{EC} are integrated over the four period bands, the ratio of the former to the latter is 2.1 for OB (1900), 5.2 for OC (2000) and 2.3 for OC (4500).

Maximum entropy energy spectra

The maximum entropy spectra (MCDONOUGH,

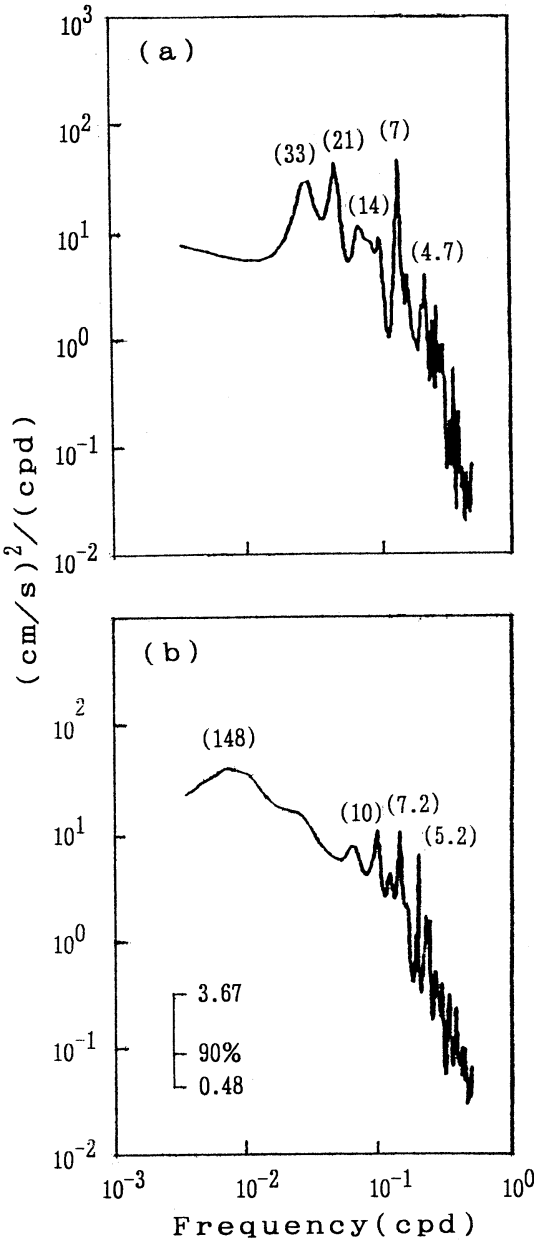

Fig. 6. Maximum entropy spectral estimates at OC (4500). (a): clockwise, (b): anticlockwise. Numerals in parentheses indicate periods (in days) at nearby peaks.

1974) with a degree of freedom of 6 show many small peaks on the time scales of 3 to 148 days, but under the 90% confidence limit only two at OC (4500) are significant (Fig.6); one at 7-day period in the anticlockwise spectrum and the other at 5-day period in clockwise spectrum. This is consistent with previous results that the kinetic energy is mostly contained in shorter time scales at deeper layers.

The squared coherence between two of the three series of velocities is estimated, which is all under the 90% confidence level. There is no significant coherence.

4. Remarks

As preliminaries, a small number of current meters were deployed at an area where the bottom topography is well oriented. The data retrieval rate was unexpectedly poor. Although solid conclusions are not drawn from such a limited amount of data, spatial inhomogeneity of the eddy activity above the continental slope southeast of Okinawa is shown with spectral analysis.

The dominant energy range appears to shift toward shorter time scales with depth, in particular, near the bottom, while the total eddy kinetic energy considerably decreases with depth.

Except at OB (1900) and OC (2000) for the band of 2–16 days, the K_{EA} is much larger than the K_{EC}. The ratio K_{EA}/K_{EC} depends on the location and the time scale. If the spatial scale of the fluctuation is much larger or much smaller than the characteristic scale of the bottom topography, the ratio K_{EA}/K_{EC} will be little affected by the bottom topography. If both are of the comparable order of magnitude, it will be seriously affected and the directivity of the eddy kinetic energy will be enhanced. Since the spatial scale is related with the time scale, there might be some relationship between the optimum time scale for a large K_{EA}/K_{EC} and the characteristic scale of the bottom topography. This scale-selective mechanism of the energy partition in the along-isobath and cross-isobath directions seems to be dependent on the height above the bottom.

More current meter data are expected to provide further information on the distribution of the eddy kinetic energy as a function of depth and time scale and its directional repartition relative to the bottom topography.

References

FU, L.-L., T. KEFFER, P.P. NIILER and C. WUNSCH

(1982): Observation of the mesoscale variability in the western North Atlantic: A comparative study. J. Mar. Res., **40**, 809–848.

GODIN, G. (1972): The analysis of tides. Liverpool Univ. Press, 264pp.

HOLLAND, W.R. and L.B.LIN (1975a, b): On the generation of mesoscale eddies and their contribution to the oceanic general circulation. I. A preliminary numerical experiment. J. Phys. Oceanogr., **5**, 642–657. II. A parameter study. *ibid.*, **5**, 658–669.

IMAWAKI, S. (1986): Numerical filters. Rept. of a preoperational survey of a proposed area for ocean disposal of radioactive wastes—low frequency water motion—. Atomic Energy Management Center, Tokyo. 175–190. (in Japanese)

IMAWAKI, S. and K.TAKANO (1982): Low-frequency eddy kinetic energy spectrum in the deep western North Pacific. Science, **216**, 1407–1408.

LUYTEN, J.R. (1977): Scales of motion in the deep Gulf Stream and cross the continental rise. J. Mar. Res., **35**, 49–74.

LUYTEN, J.R. (1982): Equatorial current measurements. I. Moored observations. J. Mar. Res., **40**, 19–41.

MCDONOUGH, R.N. (1974): Maximum entropy spatial processing of array data. Geophysics, **39**, 843–851.

MODE group (1974): The Mid-Ocean Dynamics Experiment. Deep-Sea Res., **25**, 859–910.

RICHMAN, J.G., C.WUNSCH and N.G.HOGG (1977): Space and time scales of mesoscale motions in the western North Atlantic. Rev. Geophys. Space Phys., **15**, 385–420.

SCHMITZ, W.J.Jr. (1974): Observations of low-frequency current fluctuations on the continental slope and rise near Site D. J. Mar. Res., **32**, 233–251.

SCHMITZ, W.J.Jr. (1978): Observations of the vertical distribution of low frequency kinetic energy in the western North Atlantic. J. Mar. Res., **36**, 295–310.

SEMTNER, A.J.Jr. and R.M.CHERVIN (1992): Ocean general circulation from a global eddy-resolving model. J. Geophys. Res., **97**, 5493–5550.

TAKANO, K., Y.YUAN, K.KAWATATE, S.IMAWAKI, J. SU, Z.PAN, H.ICHIKAWA and S.UMATANI (1994): Diurnal and semidiurnal current fluctuations at abyssal depths southeast of Okinawa. Proc. 7th JECSS/PAMS Workshop, La mer, **32**, 251–259.

WUNSCH, C. (1981): Low-frequency variability of the sea. *In*: Evolution in physical oceanography, ed. B.C.Warren and C.Wunsch, MIT Press, 342–374.

YUAN Y., K.TAKANO, Z.PAN, J.SU, K.KWATATE, S. IMAWAKI, H.YU, H.CHEN, H.ICHIKAWA and S. UMATANI (1994): The Kuroshio in the East China Sea and the currents east of the Ryukyu Islands during autumn 1991. Proc. 7th JECSS/PAMS Workshop, La mer, **32**, 235–244.

YUAN Y., Z.PAN, J.SU, H.CHEN, H.ICHIKAWA, S. IMAWAKI, K.KAWATATE, K.TAKANO and S.UMATANI (1995): The western boundary current east of the Ryukyu Islands. La mer, **33**, in press.

La mer 32: 251–259, 1994
Société franco-japonaise d'océanographie, Tokyo

Diurnal and semidiurnal current fluctuations at abyssal depths southeast of Okinawa

Kenzo TAKANO[*1], Yaochu YUAN[*2], Kazuo KAWATATE[*3], Shiro IMAWAKI[*3], Jilan SU[*2], Ziqin PAN[*2], Hiroshi ICHIKAWA[*4] and Shin-ichiro UMATANI[*3]

Abstract: Direct current measurements were carried out on a continental slope southeast of Okinawa from November 1991 to September 1992. Diurnal and semidiurnal current fluctuations measured by three current meters at abyssal depths and near bottom are studied. A harmonic analysis shows that the four major tidal constituents, in particular, the M_2 and K_1 are dominant during the observation period; the major axis lengths are 1.0 – 2.3 and 1.2 – 1.6 cm/s, respectively. Temporal variations of the tidal constituents suggest that there may be a topographic effect on the features of tidal current fluctuations. A rotary spectral analysis shows that the energy contained within diurnal periods of negative rotational components is much larger than that within those of positive ones. The inequality between the positive and negative components is also shown by a dynamic spectral analysis using current vector time series modified by subtracting the four major constituents of the tidal current fluctuations from the original data; it is probably due to the existence of local inertial oscillations. The suggested inertial oscillations are variable with time. The analysis also shows that the semidiurnal current fluctuations are basically composed of the semidiurnal tidal constituents.

1. Introduction

The Ryukyu Ridge is a part of the western boundary of the North Pacific subtropical gyre. Okinawa Island is located in the middle of the ridge. It has been thought that the western boundary current (WBC), the Kuroshio, of the North Pacific subtropical gyre flows in the East China Sea located northwest of the Ryukyu Ridge. However, recent studies suggest that a part of the WBC may flow east of the Ryukyu Ridge (YUAN *et al.*, 1991; SEKINE and KUTSUWADA, 1994; TAKANO *et al.*, in preparation, hereafter TP). To estimate the transport of the WBC accurately, it is necessary to observe current velocities directly. Recently CHAEN *et al.* (1993) carried out direct current measurements at abyssal depths and near the bottom southeast of the Ryukyu Ridge, and found fairly steady bottom-intensified southwestward flows. We carried out direct current measurements southeast of Okinawa at abyssal depths from November 1991 to September 1992. The results show that there are current variabilities with periods ranged from a few hours to several months at abyssal depths on the continental slope. In this paper we analyze the diurnal and semidiurnal current fluctuations basically related to tidal and inertial oscillations, and show the characteristics of the fluctuations with the tidal and near-inertial periods. This is a preliminary analysis toward future studies of tides and inertial oscillations at abyssal depths on a continental slope. Longer period variabilities with two to sixty-four days periods are studied by YUAN *et al.* (1994). TP will discuss seasonal and interseasonal variations of the abyssal flows.

*1 Institute of Biological Sciences, University of Tsukuba, Tsukuba, 305 Japan
*2 Second Institute of Oceanography, State Oceanic Administration, Hangzhou, 310012 China
*3 Research Institute for Applied Mechanics, Kyushu University, Kasuga, 816 Japan
*4 Faculty of Fisheries, Kagoshima University, Kagoshima, 890 Japan

2. Observation

The locations of mooring stations OA, OB and OC are shown in Fig.1a with bottom topography. The vertical arrangement of the current meters is shown in Fig.1b. Seven current meters were deployed in November 1991 and recovered in September 1992 on board the R/V Shijian

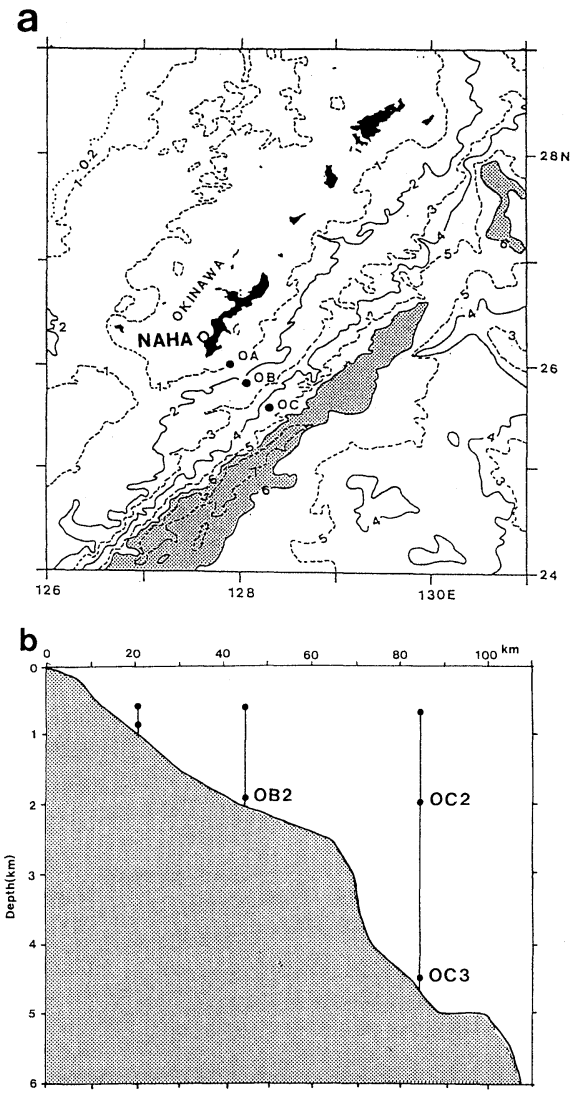

Fig.1. (a). Map showing mooring locations OA, OB and OC. Depths are shown in km; shading indicates depths greater than 6 km. (b) Vertical arrangement of current meters. Data obtained at OB2, OC2 and OC3 are analyzed.

(State Oceanic Administration, China). In this paper we analyze the year-long data obtained from three current meters at stations OB and OC; mechanical problems prevented the other current meters from giving quality records for over one month. The data sampling interval was one hour. The details of the current measurements related to this paper are shown in Table 1. Local inertial periods at stations OB and OC are 27.6 hours and 27.8 hours, respectively. Further information of the experiment is given in TP.

Hereafter OB2 refers to the current meter deployed at a depth of 1890m at station OB, and OC2 and OC3 at depths of 2000m and 4500m, respectively, at station OC.

3. Rotary spectra of current fluctuations

In order to determine the characteristics of the current fluctuation, we calculate positive (counterclockwise) and negative (clockwise) components of rotary power spectra (GONELLA, 1972) by use of the FFT (Fast Fourier Transform) method. In Fig. 2, left (right) panels indicate positive (negative) components of the rotary spectra, and upper, middle and lower panels show results for OB2, OC2 and OC3, respectively.

In each panel we find significant diurnal and semidiurnal spectral peaks. There are clear differences between the positive and negative components, in particular around the diurnal periods. The heights of the semidiurnal peaks in the positive and negative components are almost equal to each other. In contrast, those of the diurnal peaks are much higher in the negative components than in the positive ones. Further, the widths of the diurnal peaks are much wider than those in the positive ones, and hence the energy contained in the diurnal fluctuations of the negative components is much larger than that of the positive ones.

Table 1. Details of current measurements.

Station	Location	Water depth (m)	Meter depth (m)	Start date	End date	Record length (days)
OB	25° 48′ N 128° 03′ E	2020	1890	Nov. 4, 1991	Sep.9, 1992	310
OC	25° 34′ N 128° 20′ E	4630	2000	Nov.13, 1991	Sep.9, 1992	301
			4500	Nov.13, 1991	Sep.9, 1992	301

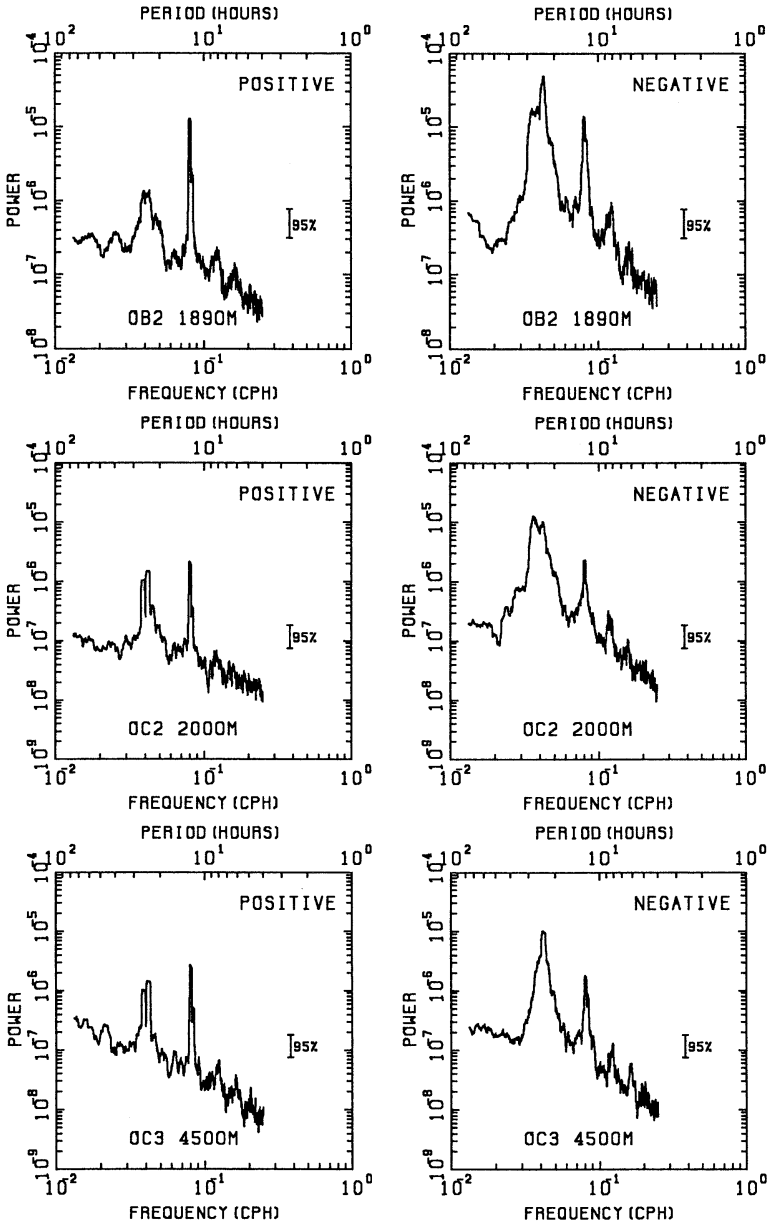

Fig. 2. Rotary power spectra in $cm^2/sec^2/cph$. Left (right) panels indicate positive (negative) components. Upper, middle and lower panels are for OB2, OC2 and OC3, respectively.

The spectral shapes of OC2 and OC3 have some similarities, in particular in the positive components. We find that two peaks around the diurnal period in the positive components are significantly separated from each other and their heights are almost equal to the heights of the semidiurnal peaks in the positive components. These features are different from those for OB2.

4. Harmonic analysis

In order to investigate the tidal fluctuations contained in the observed current vectors, we evaluate the harmonic constants of the eight

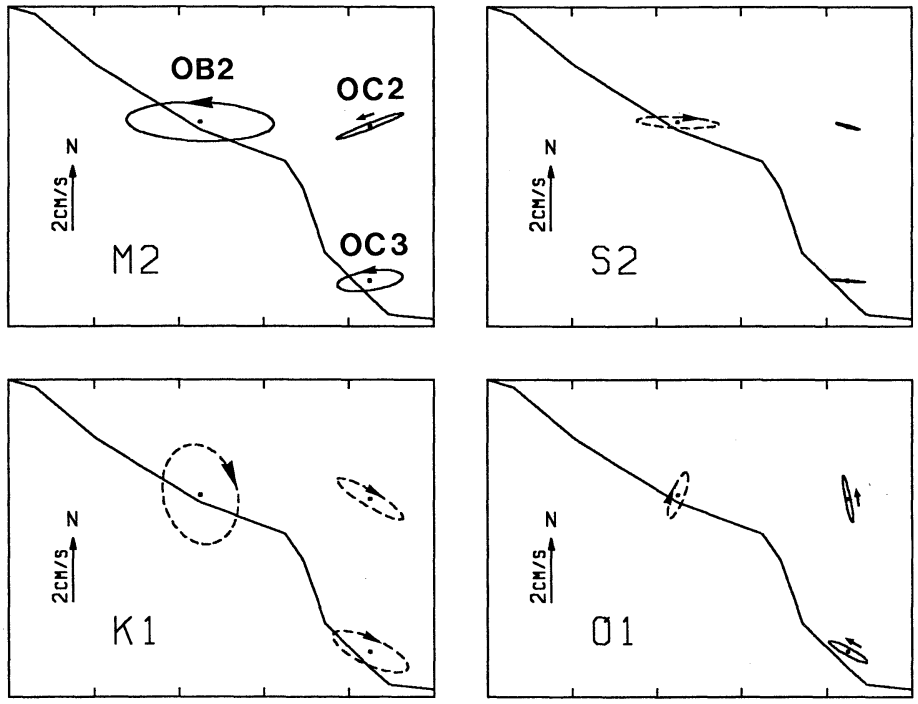

Fig. 3. Tidal ellipses of the four major constituents (M_2, S_2, K_1 and O_1) for OB2, OC2 and OC3 shown by dots (cf. Fig.1b). Upward indicates northward for the ellipses. The bottom is shown by a solid line.

major tidal constituents (M_2, S_2, K_1, O_1, N_2, K_2, P_1 and S_1) throughout the observation periods by use of the least square method. Figure 3 shows the tidal ellipses of the four major constituents (M_2, S_2, K_1 and O_1); amplitudes of the other constituents are small compared to these four major constituents. The ellipses are drawn at the corresponding individual current meter locations and depths (cf. Fig. 1b). Note that the ellipses represent horizontal current vectors with upward north. A solid (broken) ellipse means that current vectors of the tidal constituent turn counterclockwise (clockwise).

For semidiurnal tides (M_2 and S_2) and diurnal tides (K_1 and O_1), the amplitudes of the M_2 and K_1 are larger than those of the other constituents at each station. The M_2, K_1 and S_2 are stronger at OB2 than at OC. The rotational direction of the M_2 is positive and that of the K_1 is negative at each station. Between OC2 and OC3, there is no significant difference in either the ratio of the minor to major axis lengths or the length of each axis. The major axis direction of the M_2 and K_1 at OC2 and OC3 are almost the same.

Table 2. Phases (in degrees) of the four major constituents at OB2 and OC3 referred to OC2.

C.M.	M_2	S_2	K_1	O_1
OB2	−122	+30	−1	+171
OC3	+18	+27	+2	+39

The ratios of minor to major axis amplitudes are less than 0.32 except for the K_1 at OB2 (0.73). These small ratios suggest that the differences of the energy between the positive and negative components are not large. The rotary spectral analysis in the preceding section shows inequality in the energy contained within diurnal periods between the positive and negative components. The difference in the energy partition into these two components may be due to local inertial oscillations; this will be discussed later.

The phases of the four major constituents relative to OC2 are shown in Table 2. The OC3 is ahead of the four major constituents. The

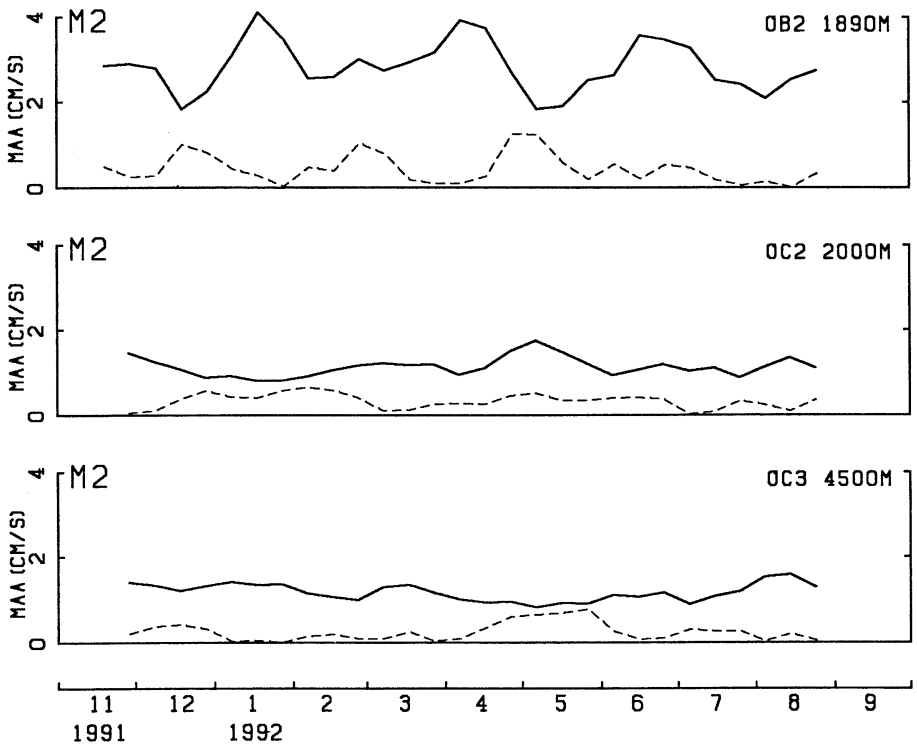

Fig. 4. Temporal variations of major (solid line) and minor (broken line) axis amplitudes for the M_2 constituent, analyzed every 10 days using 29.5 days long data. Upper, middle and lower panels are for OB2, OC2 and OC3, respectively.

phase differences might be caused by the locations of OC2 and OC3; OC2 was far above the bottom, while OC3 was close to the bottom. It might indicate the existence of internal tidal currents which are vertically out of phase (MATSUYAMA and TERAMOTO, 1985). However, we note the relatively small phase differences between OC2 and OC3 for the dominant constituents M_2 and K_1; the phases at OC3 proceed only about 40 minutes for the M_2 and about 10 minutes for the K_1. These phase differences are smaller than the temporal resolution of the present data sampling (60 minutes).

The results of barotropic tidal models suggest that the station OB is located behind the station OC for the M_2 and is almost on the same phase for the K_1, S_2 and O_1 (ODAMAKI, 1989; KO, 1993). The phase differences of the K_1 agree with the model results, but it is generally hard to explain the difference in tidal phase between the two neighboring points OB and OC with barotropic tidal models. To investigate further, we have to consider the effects of bottom topography, internal tides and others on the characteristics of the tidal currents at abyssal depths.

5. Temporal variations of tidal fluctuations

The above harmonic analysis gives us the tidal aspects of the current fluctuations throughout the observation period of about 10 months. The current meter records also indicate the existence of distinct interseasonal variations. Those interseasonal variations might affect tidal fluctuations, in particular when the tidal fluctuations include internal components induced by combined effects of the stratification and bottom topography.

Figures 4 and 5 show temporal changes of the major and minor axis amplitudes of the M_2 and K_1 constituents, respectively. They are calculated with harmonic analyses of 29.5 days long data for the four major constituents; a data length of 29.5 days is selected for avoiding the effect of the intensification of tidal currents in

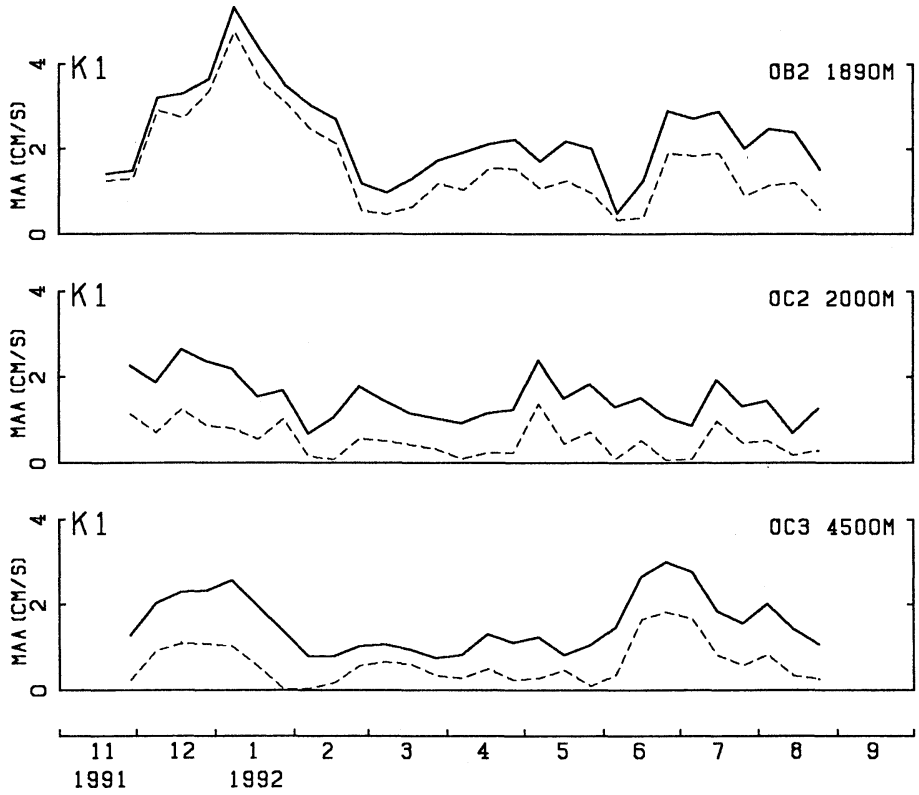

Fig. 5. Same as Fig. 4 except for the K_1 constituent.

spring tides due to some unknown reasons (TAKEOKA and MURAO, 1993). The calculations are continued with shifting the analysis period by 10 days throughout the observation period; e.g., at OB the first data set (29.5 days long) begins on Nov. 4 and the second one on Nov. 14.

The major axis amplitudes of the M_2 are much less variable at OC2 and OC3 than at OB2. This is also the case of the K_1, though its amplitudes at OC2 and OC3 are more variable than those for the M_2. At OB2 and OC3, the major and minor axis amplitudes of the K_1 become large in January and June or thereabouts, but there is no correlated increase and decrease in those of the M_2. It should be noted that both of OB2 and OC3 are located close to the bottom, which might account for some features of the observed tidal currents. It is also interesting that the minor and major axis amplitudes of the K_1 vary in almost the same manner for each current meter.

6. Discussion and summary

Diurnal and semidiurnal current fluctuations at abyssal depths southeast of Okinawa are studied. The rotary spectral analysis shows strong diurnal and semidiurnal current fluctuations (Fig. 2). The detected peaks are identified as the four major tidal constituents of which dominant are the M_2 and K_1 constituents. The tidal ellipses of the M_2 and K_1 constituents at OC2 and OC3 are similar in magnitude and major axis direction. At OB2, the magnitudes are larger than at OC2 and OC3 and the major axis directions are different from those at OC2 and OC3 (Fig. 3).

Temporal variations of the M_2 and K_1 (Figs. 4 and 5) show that throughout the observation period at OC2 and OC3, the M_2 amplitude is little variable but the K_1 amplitude is fairly variable. This suggests that the M_2 tide at OC2 and OC3 is mainly external, because each tidal current amplitude should be invariant in time if it is the barotropic tide (AOTA and MATSUYAMA, 1987).

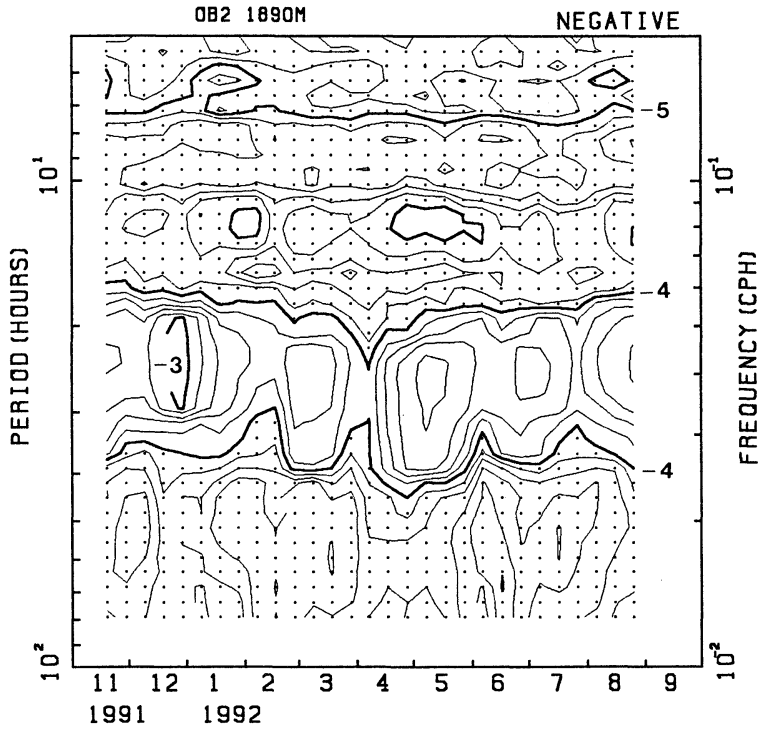

Fig. 6. Power density of the negative component of dynamic rotary spectrum at OB2 after subtracting the four major tidal constituents from the raw data. Numerals indicate logarithm of the power density ($cm^2/sec^2/cph$) to base 10. Contour inverval is 0.2. Shading indicates values less than −4.

In contrast, the major axis amplitudes at OB2 are more variable. The M_2 and K_1 constituents at OB2 might be mostly due to bottom-intensified internal tides, although it is difficult to confirm it because the vertical structure of currents is not measured.

As mentioned previously, the energy contained within diurnal periods of the negative rotary components is much larger than that of the positive components. The rotational direction of the K_1 constituent is negative, but its magnitude is not enough to account for the difference in the energy partition into the two components. This suggests that there may be non-tidal fluctuations having mainly negative components, which are probably local inertial oscillations. To investigate it in detail, we calculate dynamic spectra from current vector time series which are made by subtracting the four major tidal constituents from the original time series. Then, the harmonic constants are calculated every 10 days using 29.5 days long data.

Power density of negative components of dynamic rotary spectrum at OB2 is shown in Fig. 6 and positive components in Fig.7. A distinct high power zone is only found within near the diurnal periods (20–35 hours) in the negative components. This feature is also found at OC2 and OC3. Since the local inertial period is about 28 hours, these high energy zones are considered to be due to the inertial oscillations. Individual inertial oscillations are not persistent, and hence the estimated power is probably due to the mixture of inertial oscillations with different phases and amplitudes. The mixture does not give rise to a sharp peak at the local inertial period. This may be the reason why the peaks near the diurnal periods in Fig.6 are broad and spread over 20 to 35 hours in period. The strength of the high power zone varies in a few months. This temporal variability might be related with the variations of oceanic and/or atmospheric environments, which will be discussed in another article. Figures 6 and 7 also show that there is

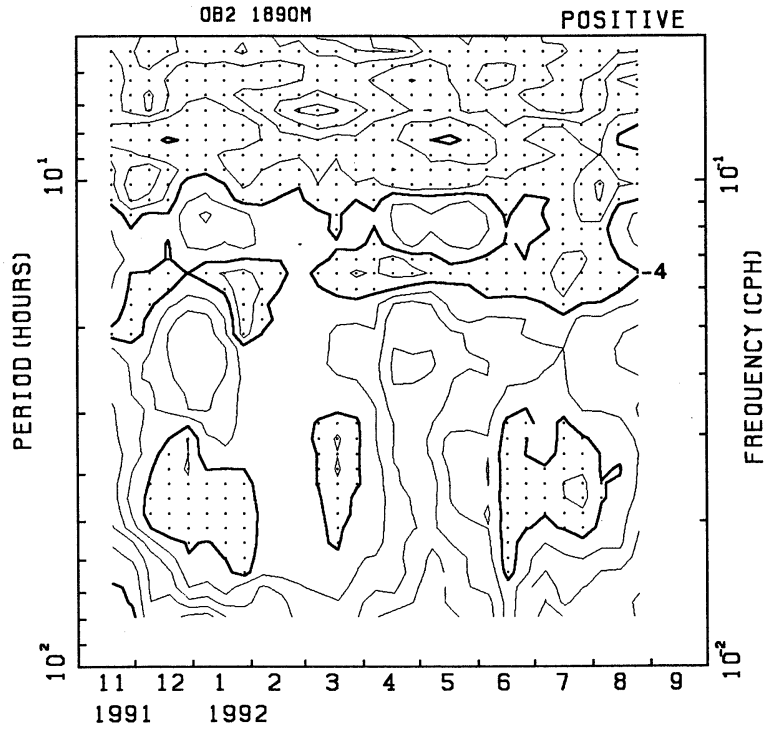

Fig. 7. Same as Fig. 6 except for the positive component.

no significant high power zone around semidiurnal periods in the two components, which indicates that the semidiurnal current fluctuations found in the original data are basically composed of tidal constituents.

Sources of the inertial oscillations cannot be identified in this study. We compare the dynamic rotary spectrum (Fig. 6) with the wind variability observed at Naha located in southwestern Okinawa. However, we cannot find any significant correlations between them. The inertial oscillations in this area might be composed of oscillations propagated from some area. FU (1981) suggested that propagating internal waves with near-inertial frequency coming to an area might induce inertial oscillations at the latitude of that area. In addition, we also have to consider the effects of the advection, bottom topography and so on. To investigate the sources of inertial oscillations, more detailed observational data covering broader area are required.

Acknowledgements

The authors would like to express their thanks to the captain and crew of the R/V Shijian for helping them in deploying and recovering the moorings. S.U. would like to thank Professor B.-H. CHOI of Sung Kyun Kwan University who kindly gave him valuable results of his tide models. This study was partly supported by the Ocean Research Project of Research Institute for Applied Mechanics, Kyushu University.

References

AOTA, M. and M. MATSUYAMA (1987): Tidal current fluctuations in the Soya Current. J. Oceanogr., **43**, 276–282.

CHAEN, M., M. FUKASAWA, A. MAEDA, M. SAKURAI and M. TAKEMATSU (1993): Abyssal boundary current along the northwestern perimeter of the Philippine Basin. pp. 51–67. *In* T. TERAMOTO (ed.): Deep ocean circulation, physical and chemical aspects. Elsevier Sci. Publ.

FU, L.-L. (1981): Observations and models of inertial waves in the deep ocean. Rev. Geophys. and Space Physics, **19**, 141–170.

GONELLA, J. (1972): A rotary-component method

for analyzing meteorological and oceanographic vector time series. Deep-Sea Res., **19**, 833–846.

KO, J.-S. (1993): Modeling of tides in the east Asian marginal seas. Master thesis, Sung Kyun Kwan Univ., Korea, 142 pp.

MATSUYAMA, M. and T. TERAMOTO (1985): Observations of internal tides in Uchiura Bay. J. Oceanogr., **41**, 39–48.

ODAMAKI, M. (1989): Co-oscillating and independent tides of the Japan Sea. J. Oceanogr., **45**, 217–132.

SEKINE, S. and K. KUTUWADA (1994): Seasonal variation in volume transport of the Kuroshio south of Japan. J. Phys. Oceangr, **24**, 261–272.

TAKEOKA, H. and H. MURAO (1993): Tidal currents influenced by topographic eddies in Uchiumi Bay. J. Oceanogr., **49**, 491–501.

YUAN, Y., M. ENDOH and H. ISHIZAKI (1991): The study of the Kuroshio in the East China Sea and the currents east of the Ryukyu Islands. Acta Oceanologica Sinica, **10**, 373–391.

YUAN, Y., Z. PAN, J. SU, S. UMATANI, S. IMAWAKI, K. KAWATATE and K. TAKANO (1994): Spectra of the deep currents southeast of Okinawa Island. La mer, **32**, 245–250.

La mer 32: 261–269, 1994
Société franco-japonaise d'océanographie, Tokyo

Inertial oscillations in the Kuroshio west of Okinawa

Hideo NAKAJIMA[*1], Shiki HASHIMOTO[*1], Arata KANEKO[*1],
Kazuo KAWATATE[*2] and Shinjiro MIZUNO[*3]

Abstract: Inertial oscillations generated in the upper layer of the Kuroshio have been investigated by using moored ADCP data together with wind data from a JMA buoy robot at an adjacent site. The ADCP data were obtained at the central region of the Kuroshio west of Okinawa during one year from 1989/12 to 1990/11. The kinetic energy of the inertial current and the Kuroshio was separated from the total current field by a simple method which uses progressive vector diagrams. During a typhoon period, a strong inertial oscillation was generated not only in the surface Ekman layer but also in the underlying region of the Kuroshio. Strong inertial oscillations were also accompanied by significant reduction of the Kuroshio energy at the surface layer throughout the year.

1. Introduction

Inertial oscillations have often been observed in the oceans (e.g., WEBSTER 1968; SAKOU and NESHYBA, 1972; KUNDU, 1976; SALAT *et al.*, 1992). Inertial oscillations in the surface layer are generated mainly by winds (POLLARD, 1970; KUNDU, 1976). The wind-generated inertial oscillations transfer kinetic energy downward and cause the deepening of the mixed layer (SHAY *et al.*, 1992; TROWBRIDGE, 1992). The sea-surface wind stresses and the heat fluxes across the surface play an essential role in the dynamics of the upper ocean (GILL, 1982; QIU and KELLY, 1993). It is known that the conditions in which inertial oscillations are effectively generated by winds are (i) the clockwise rotation of the wind direction within an inertial period in the Northern Hemisphere or the rapid weakening of a strong wind which has been blowing for a few hours up to half an inertial period (POLLARD, 1970; PRICE, 1983), and (ii) the sudden shift of the direction of a strong wind (POLLARD and MILLARD, 1970). According to POLLARD and MILLARD (1970), a strong wind blowing in a fixed direction for an inertial period rather suppresses inertial oscillations because there is a period at which the wind stress and the inertial current work in the opposite direction. Mechanisms of the generation of inertial oscillations are not so simple. The detailed processes of the vertical transfer of the energy by inertial oscillations still remain as one of the most important subjects to be elucidated because of the difficulty of current observation under severe surface conditions. The effect of typhoons on the upper ocean also attracts great concern of oceanographers (HONG and YOON, 1992; TAIRA *et al.*, 1993).

In this paper, we analyze one-year term moored ADCP (acoustic Doppler current profiler) data obtained in the Kuroshio west of Okinawa together with the wind data from a buoy robot of the JMA (Japan Meteorological Agency). Special attention is paid to the inertial oscillation generated in the Kuroshio by typhoons. In the following, the date is expressed in a format of year/month/day.

2. Observation and method

A moored ADCP observation was carried out at the station M2 indicated in Fig. 1 during a period of 1989/12 to 1990/11 (MIZUNO *et al.*, 1991). The station M2 is located at the central region of the Kuroshio flowing to the northeast between Okinawa and the continental shelf in the East China Sea. The water depth is about 1500 m. An ADCP was mounted upward on the top of the mooring line. The first mooring

*1 Faculty of Engineering, Hiroshima University, Higashi-Hiroshima 724, Japan
*2 Research Institute for Applied Mechanics, Kyushu University, Kasuga 816, Japan
*3 Hiroshima Institute of Technology, Saeki-ku, Hiroshima 731-51, Japan

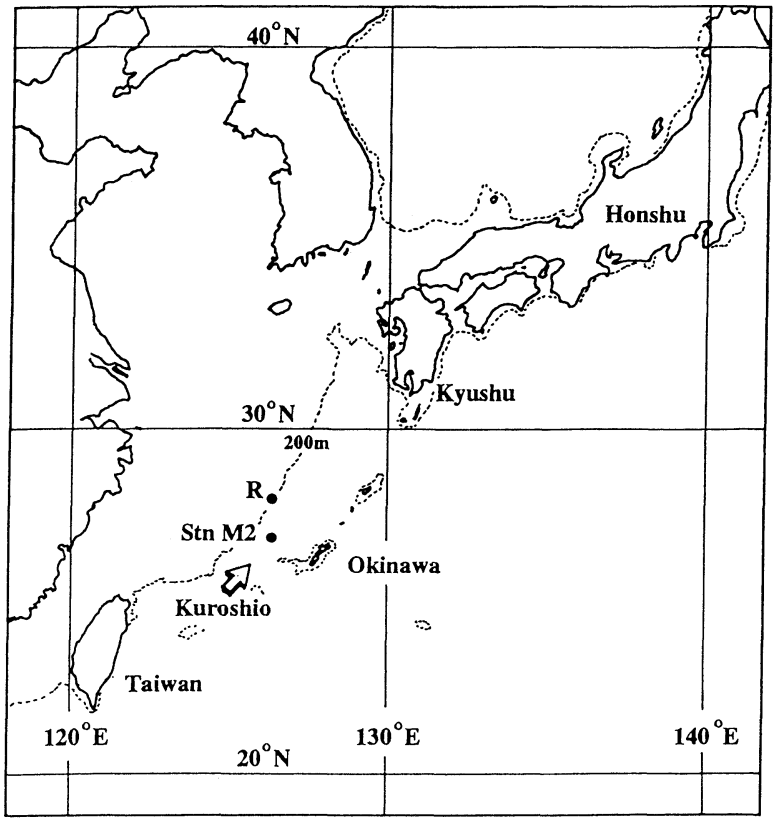

Fig. 1. Location map of the observation site. The positions of the ADCP mooring and the buoy robot of JMA are marked M2 and R, respectively.

Tabe. 1. Characteristics of the ADCP observation.

	Observation period	ADCP depth	Sampling interval	Depth resolution
First mooring	1989/12–1990/7	430 m	30 min	8 m
Second mooring	1990/7–1990/11	398 m	30 min	8 m

system was recovered immediately after resetting the second system in 1990/7 for the maintenance of the mooring system and the ADCP battery exchange. Characteristics of the first and second moorings are presented in Table 1. The location of the JMA buoy robot is also marked R in Fig. 1, where the wind at 8 m height above the sea surface was measured every 3 hours. The inertial period (frequency) at the station M2 is 26.3 h (3.81×10^{-2} ch^{-1}).

We shall make use of the progressive vector diagram to extract the inertial current from the original ADCP data. When the inertial current is superimposed on the northeastward flowing Kuroshio, we obtain a progressive vector diagram as shown typically in Fig. 2. When T_I denotes the inertial period and S the distance between two neighbobring kinks along the path on the diagram with a time interval T_I, the mean velocity of the Kuroshio during the period T_I is

$$v_K = S/T_I. \quad (1)$$

The perturbed velocity v_I is obtained by subtracting v_K from the total velocity field v,

$$v_I = v - v_K. \quad (2)$$

The v_I may be a measure of the inertial current. It can be calculated in the same way whether or not the neighboring points on the diagram with

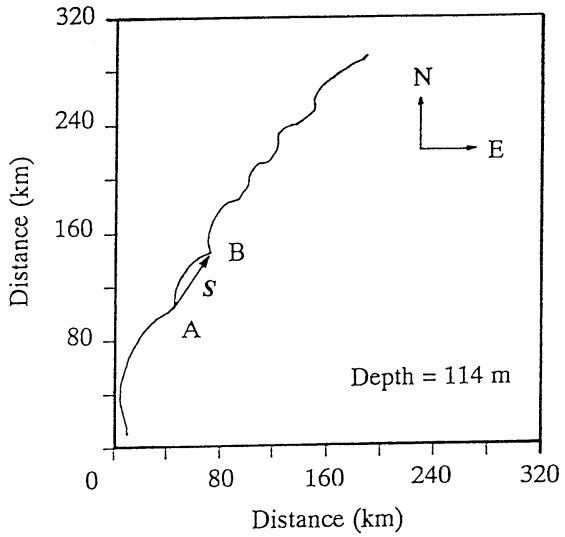

Fig. 2. Progressive vector diagram for the total velocity v obtained at 114 m depth in the observation period when the typhoon T9015 attacked the observation site.

the interval T_I are on the kinks. The four principal constituents K_1, O_1, M_2 and S_2 of tidal currents were determined through the harmonic analysis which uses the one-year data. These constituents were removed from the total velocity v prior to the calculation of v_K and v_I.

3. Results and discussion

We shall examine the monthly viariability of the inertial current. The mean direction of the Kuroshio current at station M2 is estimated as 40° clockwise from the north (NAKAJIMA *et al.*, 1992). The power spectra for the velocity component (V) in this direction including the tidal current are shown on the monthly basis for the 114 m depth data in Fig. 3. The spectral peaks corresponding to the inertial current and the semidiurnal tidal current are marked I and S, respectively. The semidiurnal current includes the M_2 and S_2 constituents. The spectral peak for the semidiurnal tidal current is clearly seen in the figure. In 1989/12, 1990/1 and 1990/5–6, inertial current with spectral level comparable to that for the semidiurnal tidal current was generated. The spectral peaks for inertial current became much higher than those for the semidiurnal tidal current in 1990/7–9. The observed periods for inertial oscillation were shorter or longer than the theoretical period. This might be caused by the Doppler effect due to the Kuroshio current or the effect of the stratification (GILL, 1982). The progressive vector diagrams at 114 m depth for the total velocity v including the tidal current are shown on the monthly basis in Fig. 4. A sequence of prominent kinks were seen on the paths for 1990/1 and 1990/8–9. These months are included in the period when the steep spectral peaks for the inertial current appear in Fig.3. The total length of the path on the diagram was remarkably decreased in 1990/8–10, showing the slack of the Kuroshio at 114 m depth.

Strongest inertial oscillation was generated when the typhoon T9015 attacked the observation site on 1990/8/29. The data for the total horizontal velocities v obtained during 8/25 to 9/9 are shown with the depth-time plot in Fig.5. The wind vectors are also shown in a series of arrows at the top of each depth profile. The wind vectors rotated clockwise during 8/29 to 9/3, evidencing that the typhoon passed the western side of the observation site. A pronounced inertial oscillation was initiated on 8/30 by this typhoon and continued until 9/5.

The method to extract the inertial current from the total current as expressed in Eqs. (1) and (2) was applied to the data during 8/28 to 9/6 when the typhoon T9015 attacked the observation site. The v_K and v_I for this period are shown with the vector plots in Figs. 6(a) and (b), respectively. For comparison, the wind vectors are also drawn at the top of the figure. A strong inertial oscillation was generated at depths of 114 to 170 m immediately after the wind with speeds greater than 15 ms^{-1} changed rapidly its direction on 8/30. This oscillation propagated downward with time. The generation process of the inertial oscillation at depths of 114 to 170 m is consistent with that proposed by POLLARD and MILLARD (1970). In the course of the generation of inertial oscillation v_K was remarkably reduced at 114 to 186 m depths.

The 3-day mean kinetic energies for the total current including the Kuroshio and the inertial oscillation are shown for various depths in Fig.7 together with those for the wind plotted against time. The E_{T3} and E_{W3} denote the 3-day mean kinetic energies for the total current and the wind,

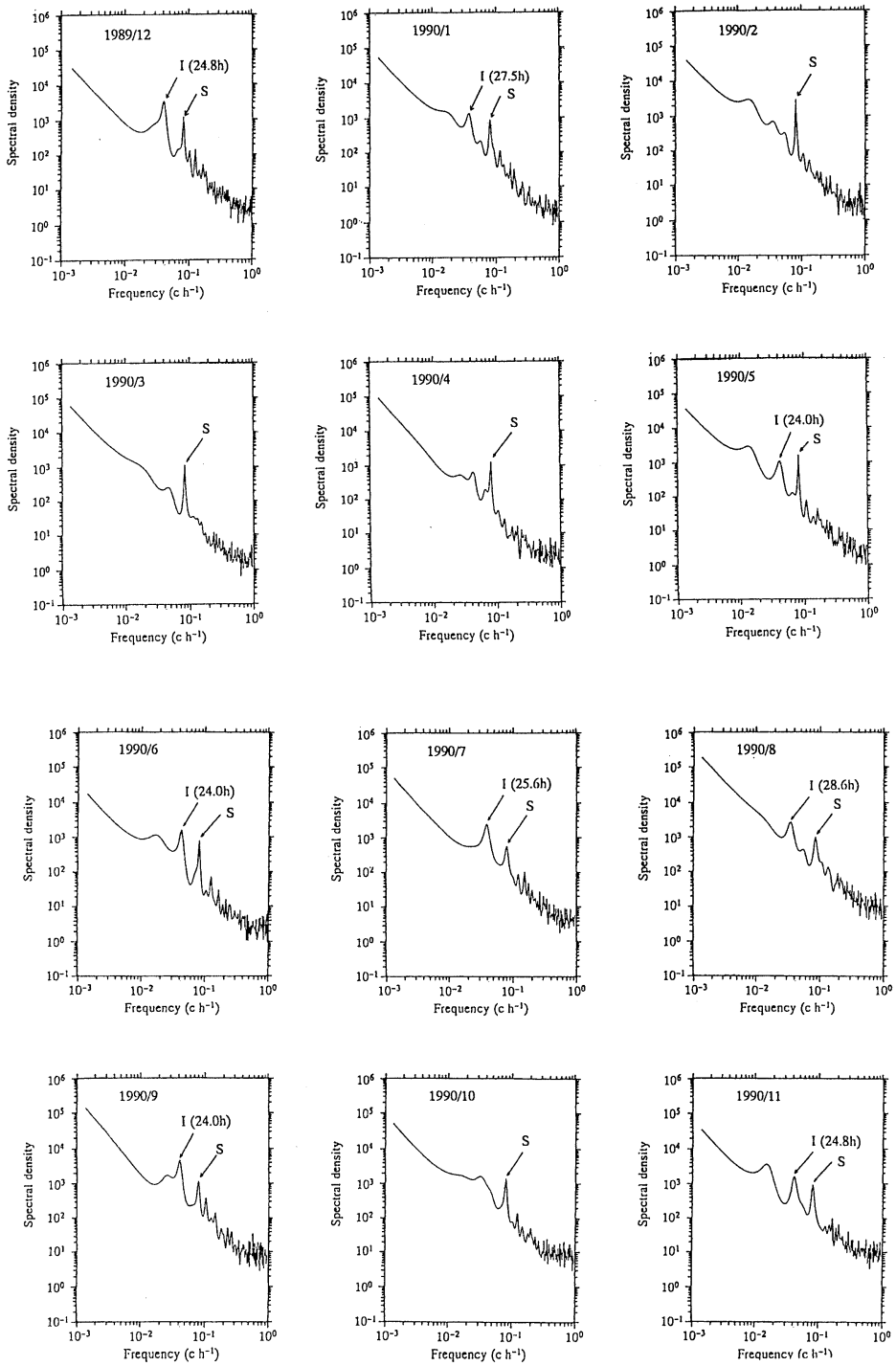

Fig. 3. Power spectra for the velocity component (V) along the mean current direction of the Kuroshio by using the data at 114 m depth. Units of spectral density: $3.6 \times 10^3 cm^2 s^{-1}$. The spectral peaks for the inertial current and the semidiurnal tidal current are marked I and S, respectively. The period of the inertial current at the peak is indicated in parentheses beside mark I.

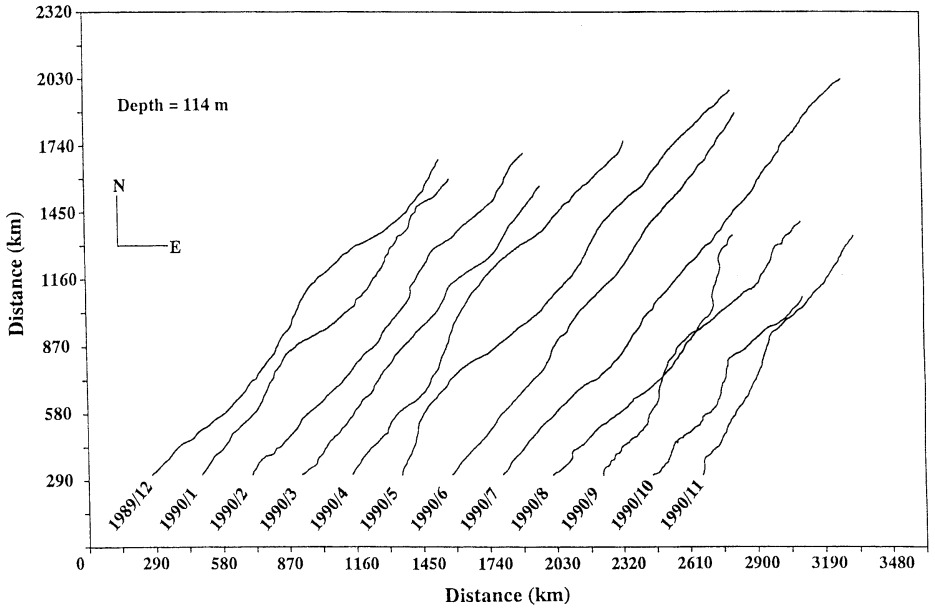

Fig. 4. Progressive vector diagrams for the total velocity v drawn on the monthly basis (114 m depth).

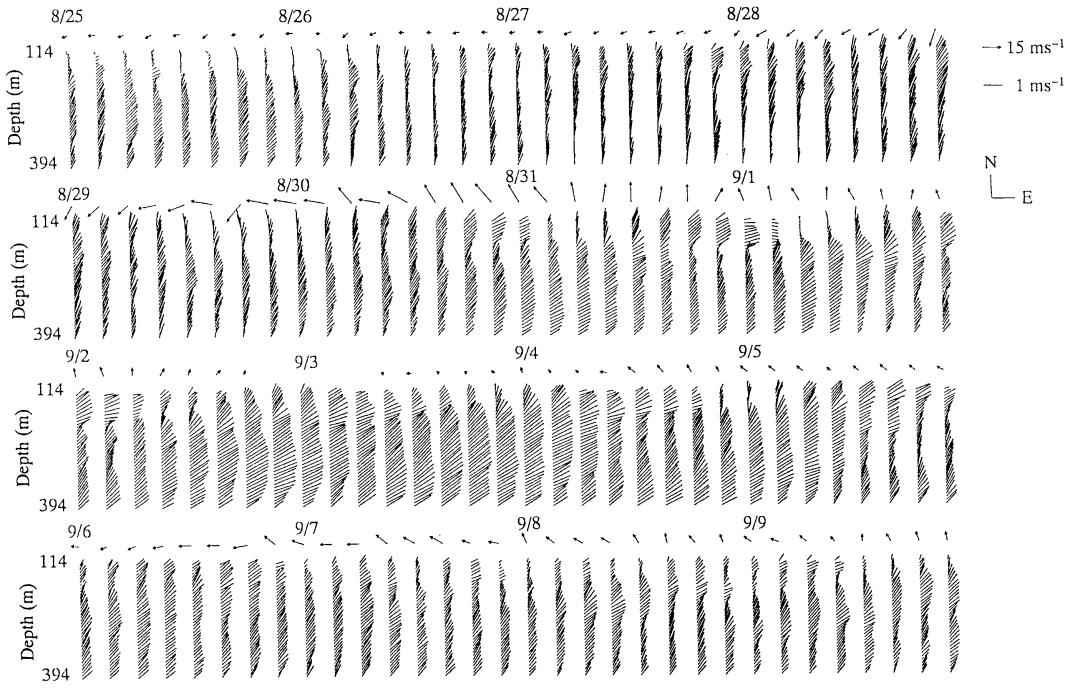

Fig. 5. Velocities at depths of 114 to 394 m when the typhoon T9015 attacked the observation site. The depth interval is 8 m. The wind vectors are also drawn above each current profile.

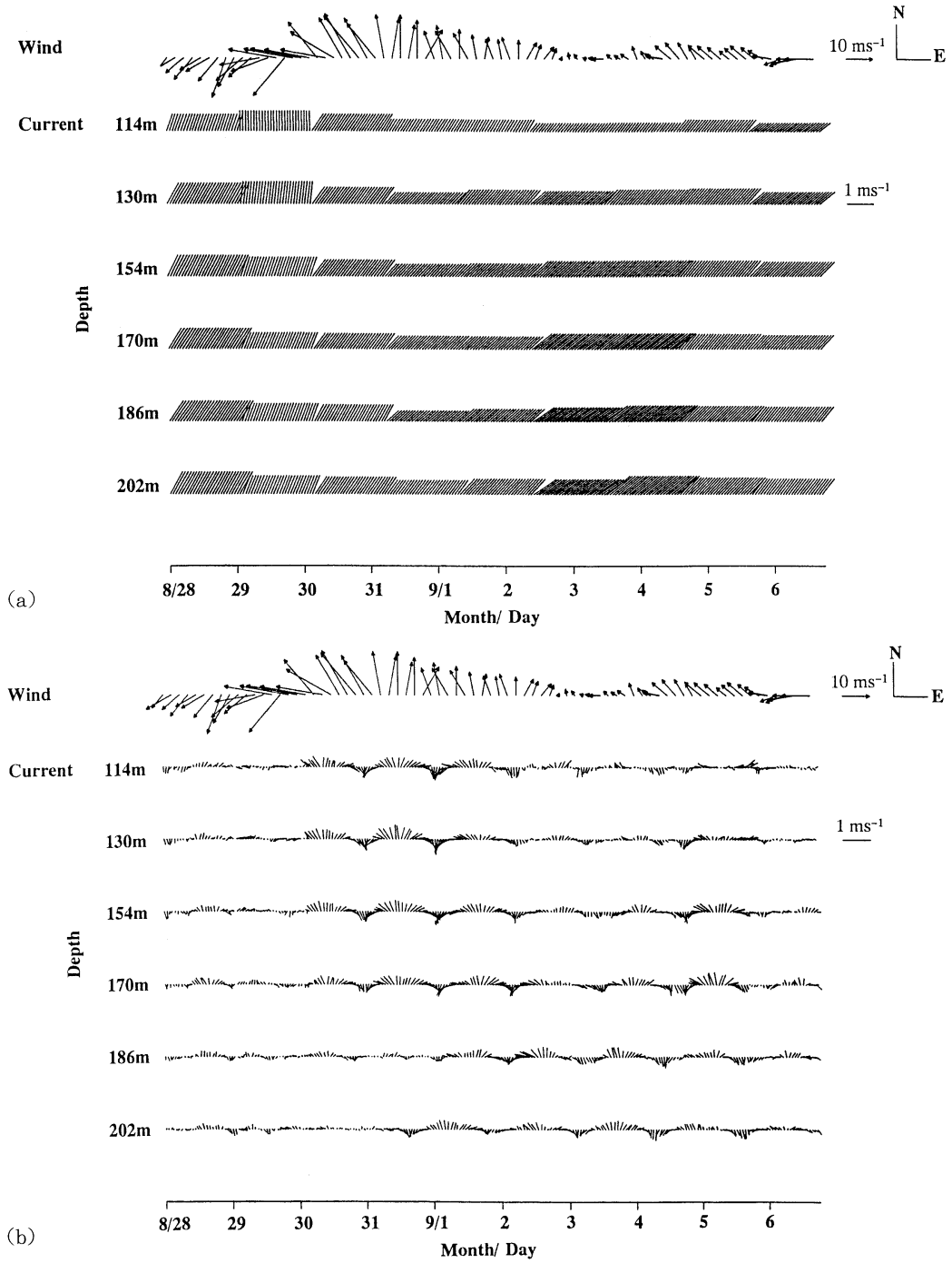

Fig. 6. The Kuroshio current (a) and the inertial current (b) during 8/28 to 9/6 when the typhoon T9015 attacked the observation site. The wind vectors are also drawn at the uppermost part of the figure. The four principal constituents K_1, O_1, M_2 and S_2 of the tidal current are removed, although the percentage of the tidal current in the total current is very small.

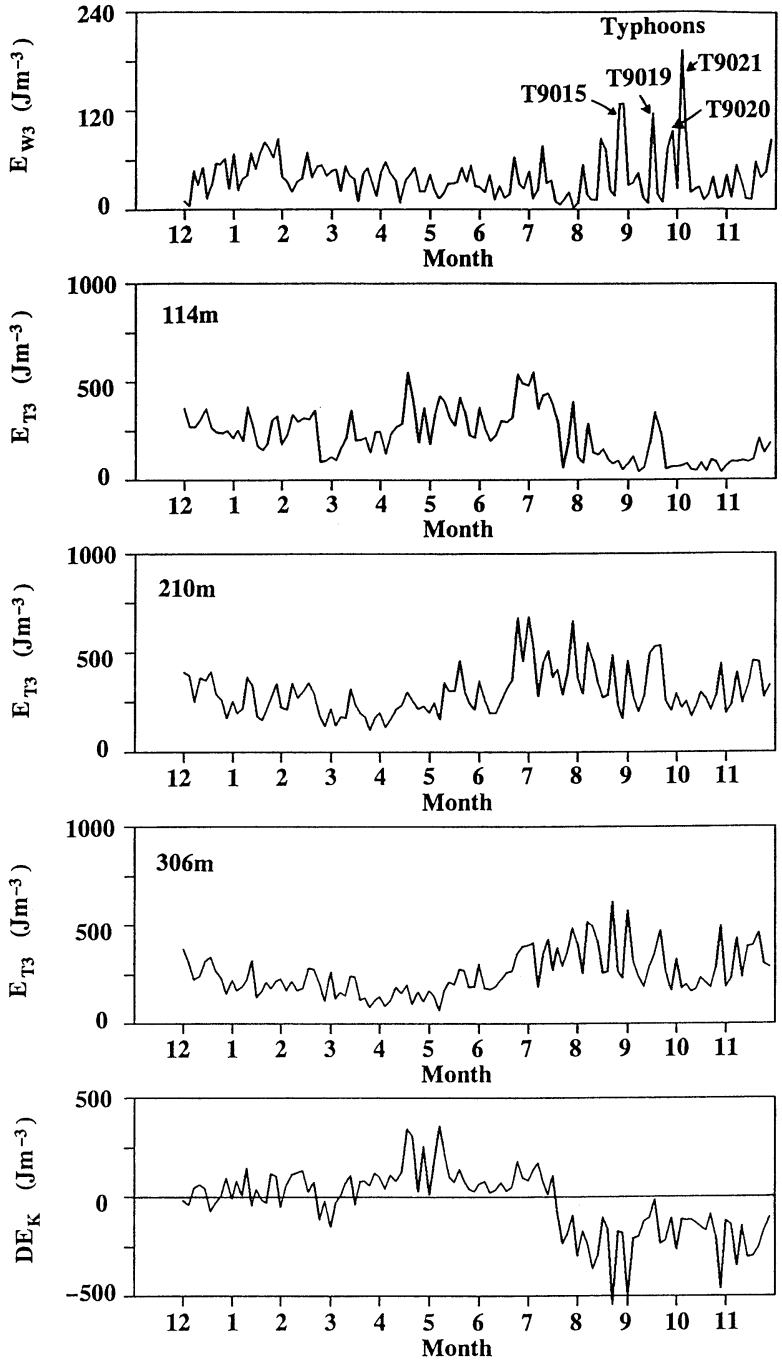

Fig. 7. Comparison of fluctuations of the 3-day mean kinetic energies of the current and wind; E_{T3} for the total current and E_{W3} for the wind.

respectively. We shall estimate the difference (DE_K) between the total kinetic energies in the surface and intermediate waters of the Kuroshio, by subtracting E_{T3} at 306 m depth from E_{T3} at 114 m depth. DE_K became negative in 1990/8–11, showing the reduction of kinetic

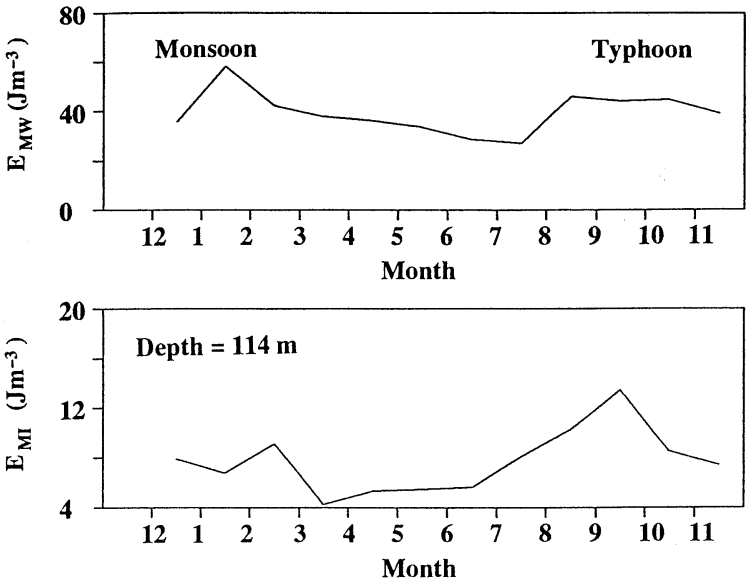

Fig. 8. Variation of the monthly mean kinetic energy of the wind and the inertial current at 114 m depth; E_{MW} for the wind and E_{MI} for the inertial current.

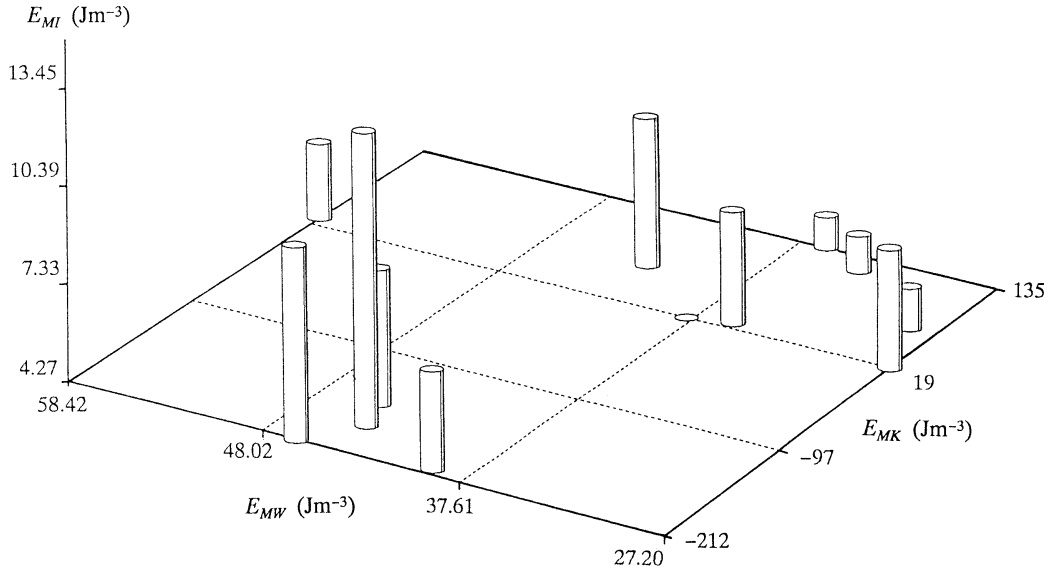

Fig. 9. Variation of the monthly mean kinetic energy for the inertial oscillation (E_{MI}) shown on the plane (E_{MW}, E_{MK}).

energy at the surface layer of the Kuroshio. This energy reduction was well correlated with the period when the severe winds caused by the typhoons T9015, T9019, T9020 and T9021 attacked successively the observation site.

The time plot of the monthly mean kinetic energies for the wind and the inertial current (E_{MW} and E_{MI}, respectively) is shown in Fig.8. E_{MI} was calculated from Eq.(2) by using the data at 114 m. E_{MW} had the largest value at the period of winter monsoon. In contrast, E_{MI} was greater in the typhoon period than in the monsoon period. It is understood that the conditions for effectively generating the strong inertial

current were satisfied more frequently in the typhoon period rather than in the monsoon period. The monthly variation of E_{MI} is shown on the (E_{MW}, E_{MK}) plane in Fig.9, where E_{MK} is the monthly mean difference between the kinetic energies of the Kuroshio at depths of 114 m and 394 m. It should be noted that strong inertial currents were accompanied by significant reduction of the Kuroshio energy at the surface layer throughout the year.

4. Conclusions

The analysis of the one-year term ADCP data obtained in the Kuroshio west of Okinawa and combined with the wind data provides us the following results on the inertial oscillation:

(1) A simple method is proposed which can extract the inertial current and the Kuroshio current from the observed data by using progressive vector diagrams.
(2) The strong inertial oscillation generated by the typhoon T9015 occurred not only in the surface layer but also in the underlying Kuroshio region.
(3) The inertial oscillations were more effectively generated in the typhoon period than in the monsoon period.
(4) Strong inertial currents were accompanied by significant reduction of the Kuroshio energy at the surface layer throughout the year.

Acknowledgements

We thank the Oceanographical Division, JMA for providing us the wind data. The data analysis was made on a HITAC M-680 computer at the Information Processing Center of Hiroshima University.

References

GILL, A. E. (1982): Atmosphere-Ocean Dynamics. Academic Press, New York, 662pp.

HONG, C.-H. and J.-H. YOON (1992): The effect of typhoon on the coastal sea level variations in the Tsushima Straits. Umi no Kenkyu, **1**, 225-249. (in Japanese)

KUNDU, P. K. (1976): An analysis of inertial oscillations observed near Oregon Coast. J. Phys. Oceanogr., **6**, 879-893.

MIZUNO, S., K. KAWATATE, A. KANEKO and T. NAGAHAMA (1991): Direct measurements of the Kuroshio in the East China Sea (III)- a study of system for measuring heat and momentum fluxes of the ocean (1st report)-. Bull. Res. Inst. Appl. Mech., **71**, 1-18. (in Japanese)

NAKAJIMA, H., A. KANEKO, N. GOHDA, K. KAWATATE and S. MIZUNO (1992): One-year mooring of an ADCP in the central region of the Kuroshio west of Okinawa. Proc. PORSEC (Pacific Ocean Remote Sensing Conference) - '92, Okinawa, **1**, 112-115.

POLLARD, R. T. (1970): On the generation by winds of internal waves in the ocean. Deep-Sea Res., **17**, 795-812.

POLLARD, R. T. and R. C. MILLARD, JR. (1970): Comparison between observed and simulated wind-generated inertial oscillations. Deep-Sea Res., **17**, 813-821.

PRICE, J. F. (1983): Internal wave wake of a moving storm. Part I: Scales, energy budget and observations. J. Phys. Oceanogr., **13**, 949-965.

QIU, B. and K. A. KELLY (1993): Upper-ocean heat balance in the Kuroshio extension region. J. Phys. Oceanogr., **23**, 2027-2041.

SAKOU, T. and S. NESHYBA (1972): The temporal structure of oceanic motion off the Oregon Coast, Northeastern Pacific, 1969. J. Mar. Res., **30**, 1-14.

SALAT, J., J. TINTORE, J. FONT, D.-P. WANG and M. VIEIRA (1992): Near-inertial motion on the shelf-slope front off Northeast Spain. J. Geophys. Res., **97**, 7277-7281.

SHAY, L. K., P. G. BLACK, A. J. MARIANO and D. HAWKINS (1992): Upper ocean response to hurricane Gilbert. J. Geophys. Res., **97**, 20227-20248.

TAIRA, K., S. KITAGAWA, H. OTOBE and T. ASAI (1993): Observation of temperature and velocity from a surface buoy moored in the Shikoku Basin (OMLET-88)- An oceanic response to a typhoon. J. Oceanogr., **49**, 397-406.

TROWBRIDGE, J. H. (1992): A simple description of the deepening and structure of a stably stratified flow driven by a surface stress. J. Geophys. Res., **97**, 15529-15543.

WEBSTER, F. (1968): Observations of inertial-period motions in the deep sea. Rev. Geophys., **6**, 473-490.

La mer 32: 271–278, 1994
Société franco-japonaise d'océanographie, Tokyo

Two modes of the salinity-minimum layer water in the Ulleung Basin

Yang-Ki CHO* and Kuh KIM*

Abstract: CTD data taken bimonthly in 1991 show two modes of the salinity-minimum layer (SML) water less saline than 34.00‰ in the Ulleung Basin; the North Korean Cold Water (NKCW) and the East Sea Intermediate Water (ESIW). The NKCW was observed only along the east coast of Korea in summer, whereas the ESIW was observed around Ulleung Island in April and spreading southward in the Ulleung Basin subsequently. The depth of the SML is 100 to 200 m for the NKCW and 200 to 400 m for the ESIW. The temperature at the core of the NKCW is about 1.5℃, but that of the ESIW is higher than 2.0℃ in general during 1991.

1. Introduction

The East Sea has been divided into the warm water region and the cold water region (KAJIURA *et al.*, 1958; MORIYASU, 1972), since UDA (1934) found a polar front in the middle of the East Sea. MORIYASU (1972) defined water masses in the East Sea following this division; surface and subsurface water in each region, and the East Sea Proper Water (henceforth, ESPW) which is made of deep and bottom waters. Another water mass is situated between the Tsushima warm water and the proper water in the warm water region. This water is characterized by salinity-minimum and dissolved oxygen-maximum layer (KAJIURA *et al.*, 1958; MORIYASU, 1972). Despite of its distinct characteristics, detailed observation of salinity-minimum layer (henceforth, SML) water was scarce to understand its distribution and movement.

The SML has been also observed in the Ulleung Basin and became a subject of intensive investigation. KIM and CHUNG (1984) found an SML and dissolved oxygen-maximum layer in the southwestern region of the basin in September 1981 and named it the East Sea Intermediate Water (henceforth, ESIW) because of its distinct characteristic similar to that observed south of the polar front in the central part of the East Sea (KAJIURA *et al.*, 1958). KIM, LIE and CHU (1991) reported the widespread presence of the SML in the western half of the basin in August 1986. Previously KIM and KIM (1983) reported that the North Korean Cold Water (henceforth, NKCW) along the Korean coast has similar properties as the ESIW. Most of historical data used to identify the SML in the Ulleung Basin were taken with bottle casts at standard depths. Therefore, it is often difficult to distinguish the SML from the ESPW, and moreover the NKCW from the ESIW.

Recently KIM *et al.* (1991) indicated a possibility of two modes of waters for the SML, analyzing CTD data taken in the Ulleung Basin; three CTD sections across the Ulleung Basin show that the salinity-minimum water found at shallow depth off the Korean coast is less saline and warmer than similar waters observed widely in the basin. Although the NKCW and the ESIW are similar in their vertical structure, it is important to know whether their properties are different enough to imply different origin and passage into the Ulleung Basin.

Understanding of the circulation in the Ulleung Basin requires an in-depth investigation of physical characteristics and their temporal and spatial variations, for which bimonthly surveys were conducted in 1991, taking 60 CTD stations each time (Fig. 1). It should be noticed that the northernmost K-line running from the Korean coast to Dok Island is specially designed to find any indication of an inflow of the cold water from north. This is the first time that CTD sections were repeated between Ulleung Island and Dok Island. At each station SBE 19 profiler of Sea-Bird Electronics Inc. was

* Department of Oceanography, Seoul National University, Seoul, 151-742, Korea

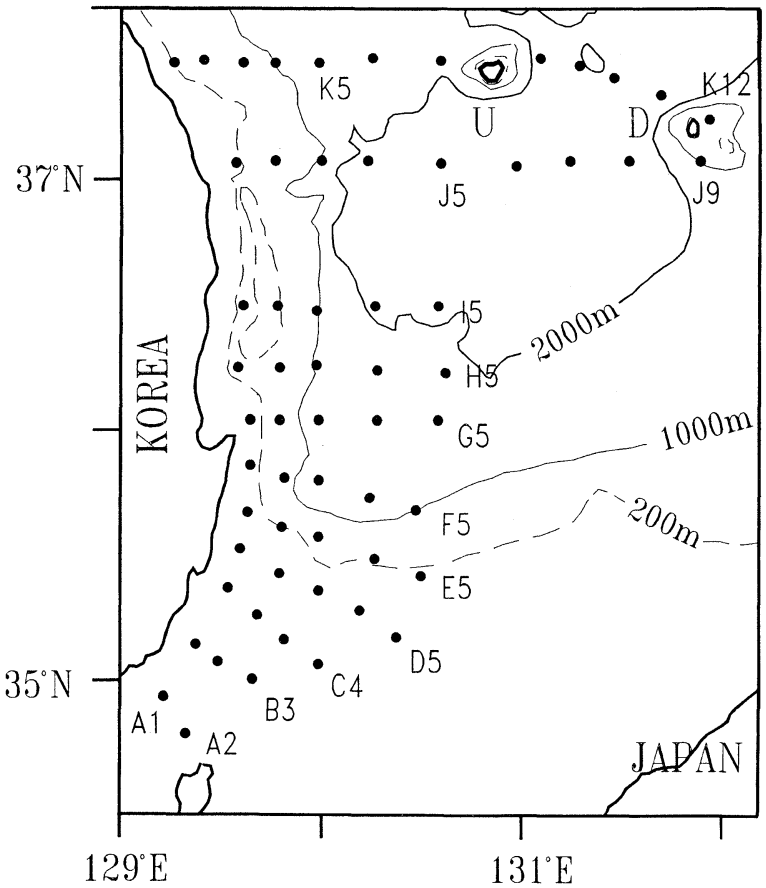

Fig. 1. CTD stations taken in April, June, August, October, 1991. Sections of K and J lines are presented in Figs. 2 and 5.

lowered to a nominal depth of 500 m at a speed of 60 m/min approximately, taking two samples of temperature, conductivity and pressure in one second, which give a vertical resolution of about 50 cm. Final data for analysis were obtained by averaging temperature and salinity data over two decibars.

The purpose of this paper is to report spatio-temporal variation of the characteristics of the salinity-minimum waters in detail, which renders clear distinction between the NKCW and the ESIW.

2. Vertical sections

Salinity sections shown in Fig. 2 illustrate a large change of salinity across the K-line from April through October 1991. In April salinity varies little between 34.1‰ and 34.0‰ in the upper 200 m except for the high salinity core near surface at stations K3 and K12. Below this the SML is observed across the section. In Fig. 2 the isohaline of 34.05‰ is chosen to indicate the minimum layer. Previously KIM and CHUNG (1984) used 34.05‰ as a criterion to define the layer in the southwestern region of the East Sea. It will be shown in the T–S diagram that this criterion is also useful in the present case. The SML in the K section is shaped like a bowl, deep and thick at the center near Ulleung Island and relatively shallow and thin away from the center. The diameter of the bowl is about 200 km. At stations K7 and K10 salinity in the minimum layer is even lower than 34.00‰. It is interesting to compare this section with another one taken at the same location in October, 1990 which is shown in Fig. 3. The SML defined by

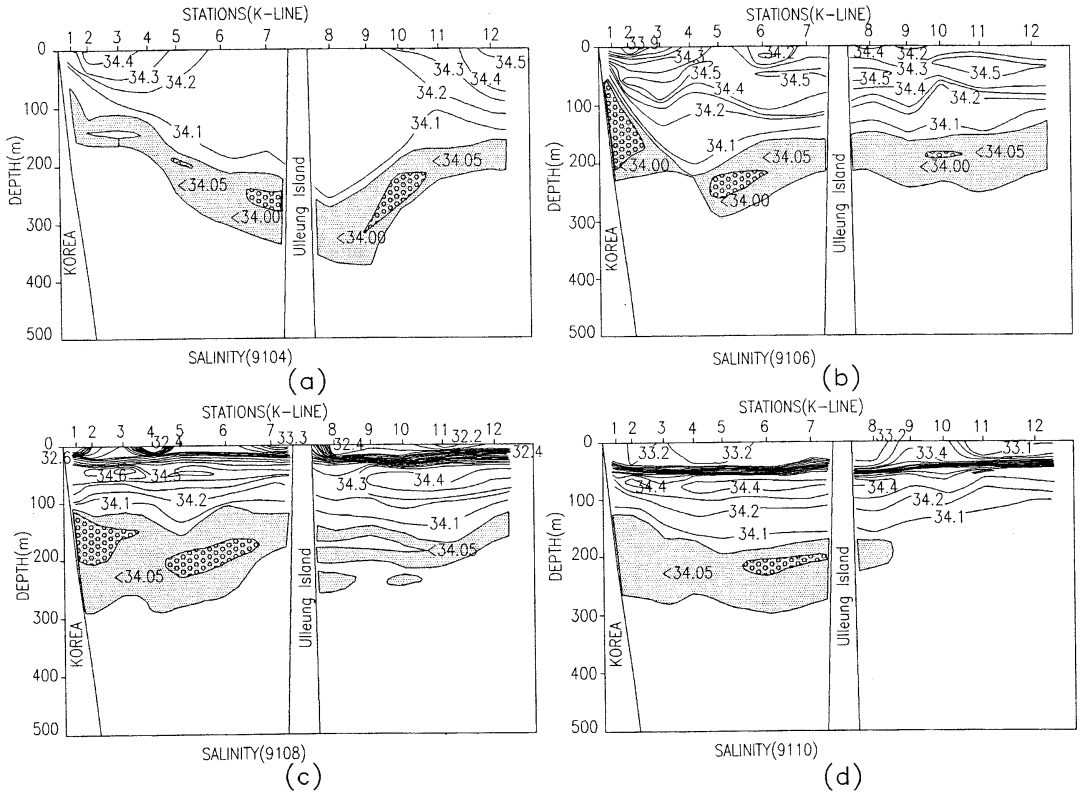

Fig. 2. K sections of salinity in April (a), June (b), August (c) and October (d), 1991. The waters with salinity less than 34.05‰ are shaded and salinity less than 34.00‰ is indicated with small circles.

34.05‰ was also observed six months before, but salinity is nowhere lower than 34.00‰. A period of six months is too long to speculate any specific process for the change from Fig.3 to Fig. 2. However, there is no doubt that the low salinity cores less than 34.00‰ in Fig. 2 represent a newly arrived water mass.

In June 1991 the salinity in the upper 100 m becomes higher than that observed in April. Despite this change, the SML remains, but relatively flat at about 200 m, losing its bowl-like structure. It is important to note that a new core of low salinity less than 34.00‰ appears at stations K1 and K2 near the Korean coast, leaning against the continental slope. Its shallow depth and triangular shape is separated from the rest of the SML. In August the SML becomes thicker between the Korean coast and Ulleung Island. However, two cores of low salinity are not connected closely. In October the

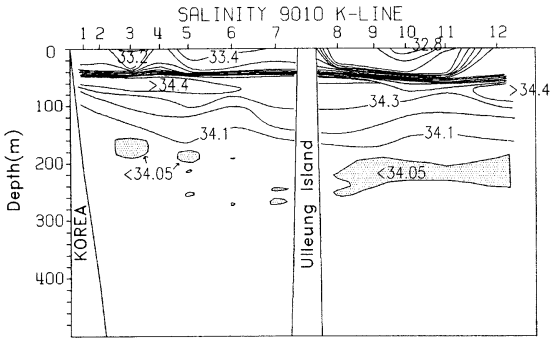

Fig. 3. Same as in Fig. 2 except for October, 1990.

core near the Korean side disappears as the thickness of the SML is reduced and its presence east of Ulleung Island is limited only at K8.

We select stations K2 and K10, where cores of low salinity appear in August and April, to examine the variation of the T–S relation in time.

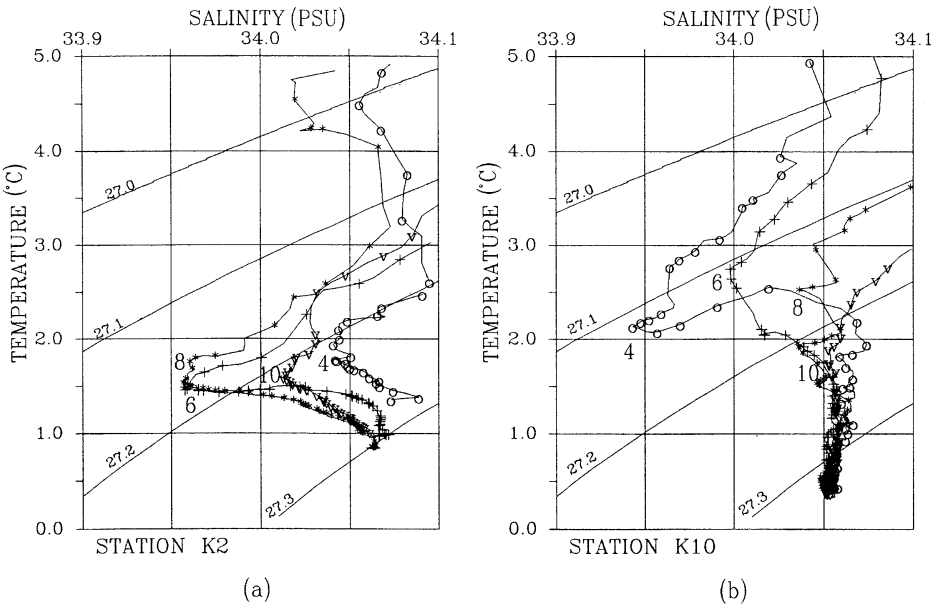

Fig. 4. Temperature-salinity diagrams for waters colder than 5℃ at stations K2 and K10. Numbers 4,6,8 and 10 represent months of observation.

Since the low salinity at intermediate depths is of our interest, Fig. 4 shows T–S diagram for temperature range of 0–5℃ only. The lowest salinity observed at K2 is about 33.96‰, nearly the same for June and August. This diagram indicates that below this layer salinity increases rapidly as temperature changes little, particularly so in June and August. Although the lowest salinities in April and October are higher than 34.00‰, all T–S curves clearly indicate the presence of the salinity-minimum.

At station K10 the lowest salinity is observed in April, which is less than that observed in June and August at K2 by 0.013‰. The minimum at K10 in June is substantially larger than that in April, but still very well-defined. In August multiple values of the minima appear as their salinities increase further, which is true at stations K8 and K9 as shown in Fig. 2. The minimum at K10 is not apparent in October. From T–S curves at K2 and K10 it is possible to distinguish the SML by S = 34.05‰, because of its relatively stable salinity for cold waters with T $<$ 1℃ and the rapid increase of the salinity upward. Therefore salinity-minimum layers are indicated according to this criterion. It is also noticed in the T–S diagram that temperature of salinity-minima at K2 in June, August and October is about 1.5℃, but that at K10 is higher than 2.0℃ in general.

Salinity section along J-line taken in April also shows a bowl-shape structure of the SML in Fig. 5 which is similar to the SML along K-line. The depth of the bowl is between 300 m and 400 m, which is deeper than that shown for K-line (Fig. 2). It is interesting that the bowl-shaped minimum layer is imbedded at the base of permanent thermocline in the temperature range of 2–4℃ as can be seen in Fig. 5. Geostrophic current relative to 500 db is of the order of 5–10 cm/s into the section between J3 and J6 and out of it between J6 and J8. Together with a meridional section passing through J5 it is possible to show that these currents make a clockwise circulation around the bowl-like structure. In October the SML of J-line is in general flat at about 200 m without the core (S $<$ 34.00‰). The temporal change of the salinity section from April to October is consistent with that of the temperature section.

3. Lateral spreading

Fig. 6 shows the horizontal distribution of the lowest salinity at stations with the SML. In April SML is observed extensively along K- and J-line in the northern part of the survey area.

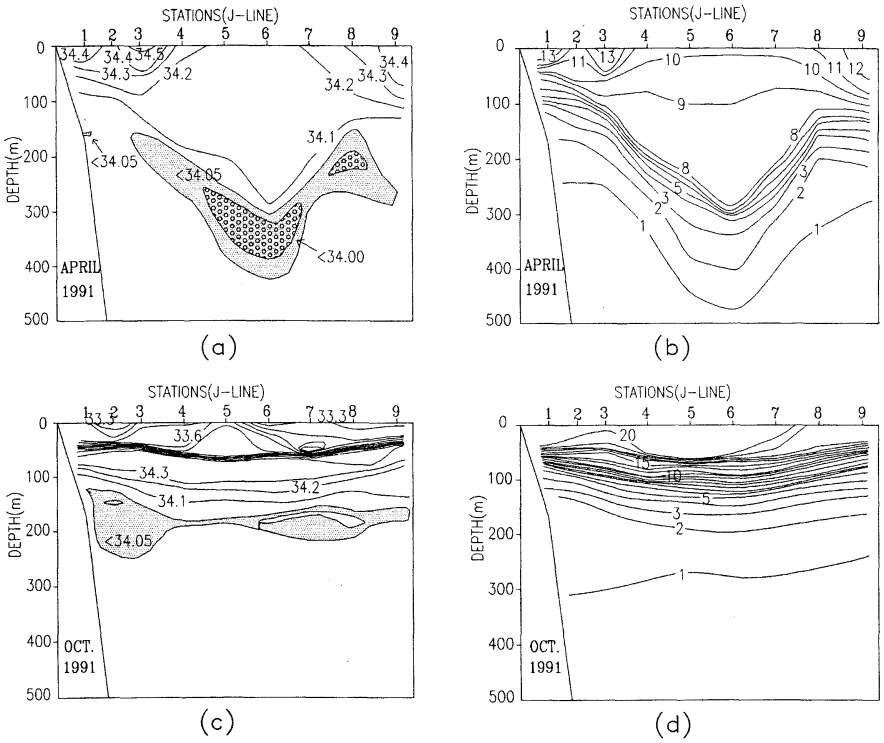

Fig. 5. J sections of salinity (a, c) and temperature (b, d) in April (a, b) and October (c, d), 1991.

Particularly it is noticed that the low salinity less than 34.00‰ is distributed around Ulleung Island. Except for two stations K11 and J9 temperature at the SML is higher than 2℃. It is important that temperature for salinity less than 34.00 ‰ is higher than 2℃ without any exception.

From April to June we notice several changes in the horizontal extent of SML. First, a new low salinity core less than 34.00‰ appears at K1 and K2 (see Fig. 1 for location) near the Korean coast, which is more than 100 m thick as shown in Fig. 2. Its temperature is lower than 2℃ unlike the core observed around Ulleung Island in April. Second, the SML is newly observed at H5 and I5 which are located almost due south of Ulleung Island. The high temperature core ($T > 3$℃) associated with the SML moves southward at the same time. It is important to note that this movement is not limited at depth of the SML, as can be seen in Fig. 7. Horizontal temperature at 200 m clearly indicates the presence of the warm bowl around Ulleung Island in April, although we cannot close isotherm due to insufficient data. In June the warm bowl is located south of Ulleung Island. As it is shown already in Fig. 5 that the SML is part of the bowl-like structure circulating clockwise with warm water inside, the SML spreads as the warm bowl moves southward.

In August the SML is observed at most stations. Particularly the core of the low salinity less than 34.00‰ is found along the Korean coast, contrasting its prevalence around Ulleung Island in April. The core which is observed only at K1 and K2 in June appears along the Korean coast as far south as G1. It should be noticed that the temperature of this core is close to 1.5 ℃ except for a couple of isolated stations. East and south of Ulleung Island temperature of SML is higher than 2.0℃ in August like in April, although it is not as high as 4℃ as observed at some stations in April and June. Since the warm bowl remains in this area through August (Fig. 7), it is quite likely that the SML southeast of Ulleung Island is of the same water as observed in April and June. In October the core along the Korean coast disappears, although the

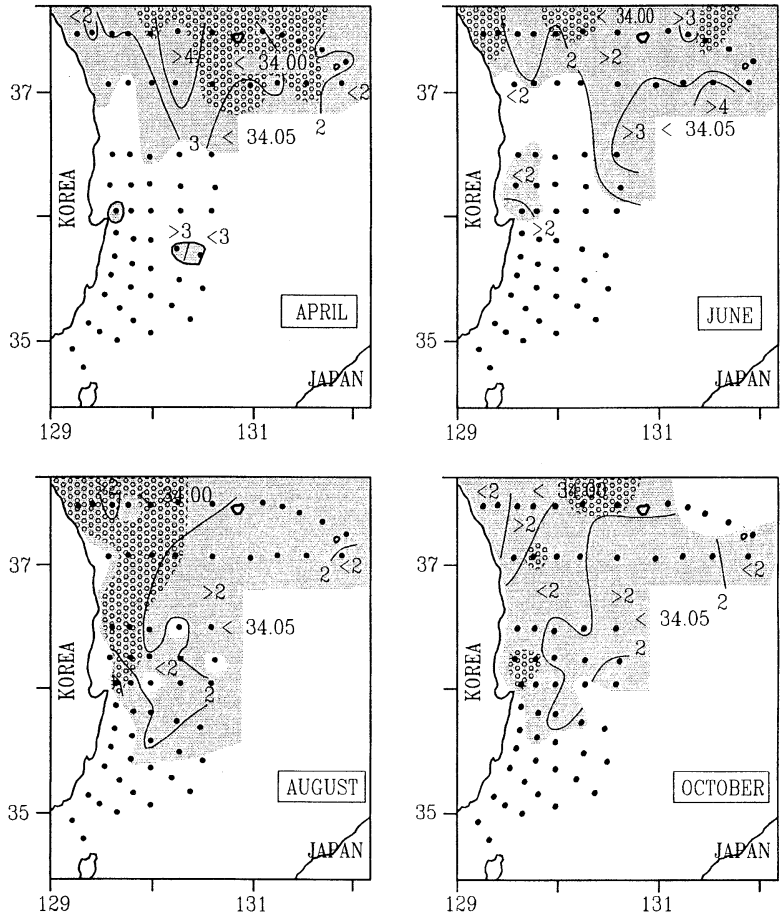

Fig. 6. Horizontal distribution of the lowest salinity in the salinity-minimum layer. The solid lines are the temperatures of the lowest salinity water in April, June, August and October, 1991. The waters with salinity less than 34.05‰ are shaded and salinity less than 34.00‰ is indicated with small circles as in salinity sections shown in Figs. 2 and 5.

SML is still observable widely in the Ulleung Basin.

4. Discussion and conclusion

In summary, the SML was observed in April, 1991 in the northern area of the Ulleung Basin with a low salinity core less than 34.00‰ around Ulleung Island. In August another core appeared along the coast of Korea. Salinities of SML cores are similarly as low as 33.95‰ as shown in Fig. 4, but they differ not only in the timing and location of observation in the basin, but their temperature and depth of observation. The former is warmer than 2℃ and observed deeper than 200 m and the latter is about 1.5℃ and shallower than 200 m. Since the latter was observed at K1 and K2 in June before its extensive presence along the east coast of Korea in August, it is reasonable to consider a current flowing southward along Korea, carrying this particular water. This water has been known as the NKCW (KIM and KIM, 1983), although there is no direct observation of this current yet.

It is very important to note that the former was observed extensively around Ulleung Island in April before the observation of the NKCW along the Korea coast. This indicates that there is another way for the SML to be introduced into the Ulleung Basin, as suggested previously by KIM and CHUNG(1984). As the SML is imbedded at the base of the warm bowl structure, it spreads into the basin as the bowl moves

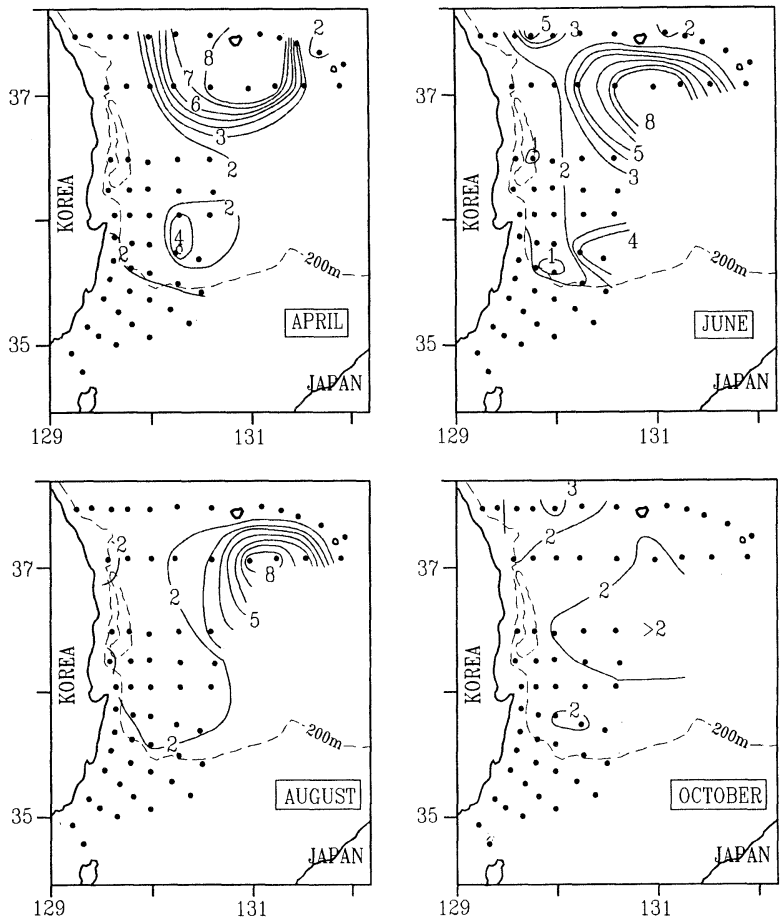

Fig. 7. Horizontal distributions of the temperature at 200 m in April, June, August and October, 1991.

southward in time. It seems that the presence of an anticyclonic (clockwise) circulation associated with the warm bowl is essential for the spreading of the SML.

The salinity of the SML water increases in time due to vertical mixing with neighbouring saline waters. However temperature changes little during this mixing process, because it has colder and warmer water above and below it. We can easily find an example of this process in Fig. 4. Temperature remains less than 2℃ at K2 and above 2℃ at K10 respectively over a period of six months, whereas the salinity increases in time.

The two cores of low salinity less than 34.00 ‰ with different temperatures suggest two different processes of their formation. First, it is possible that they represent different waters. There is no doubt that both of them are formed during winter due to cooling, most likely in the northwestern region of the East Sea. As temperature is in general low along the east coast of North Korea late winter, compared with offshore temperature, the two cores may originate from different locations; the NKCW along the Korean coast and the core around Ulleung Island from somewhere offshore. In this regard it is worthwhile to know that core temperature and salinity of the SML found at 37° 58′ N and 131° 00′ E, 60 km north of Ulleung Island on May 22, 1991 are 4.19℃ and 33.973‰ (Maizuru Marine Observatory, 1991). Similarly high temperatures of the SML were observed at a few stations nearby. These observations are consistent with the formation of the SML with temperature higher than 2℃.

Another possibility is that the two cores are formed in the same region, but at different time. As cooling continues throughout winter, part of water may leave the surface before the end of the cooling period, sinking and spreading at mid depth. On the other hand, the lower temperature of the NKCW implies that it is likely the final products of the cooling period along the coast of North Korea. At this point it is difficult to delineate the formation process any further without data taken in formation region during winter.

It is clear now that the NKCW is distinguished from the rest of the SML water in the Ulleung Basin, because of the separation in the temperature of the SML and its horizontal distribution in time. We postulate that the core of the SML around Ulleung Island found in April is different from the NKCW and term it the East Sea Intermediate Water (ESIW). When KIM and CHUNG (1984) introduced the ESIW based upon the data taken in 1981, its temperature range was 1–3℃ in the depth range of 100–300 m and no distinction was made for the NKCW. However, now it is certain that there are two modes of SML in the Ulleung Basin as observed in 1991, which spread in the basin following two different routes.

Recently there have been a couple of noteworthy investigations concerning this suggestion. KIM, LIE and CHU (1991) showed that in August, 1986 some of the SML water in the central part of the basin is lower than that along the Korean coast. KIM *et al.* (1991) showed two cores of the SML along the K-line in May, 1988; one near the Korean coast and the other near Dok Island which is the same location as station K11. These imply that the ESIW in the central part of the basin is not the extension of the NKCW, but has an independent route of southward flow in the basin.

It may be better at this point not to limit the temperature and salinity range of the ESIW. KIM, LIE and CHU (1991) showed a very significant interannual variation of T–S properties for the SML along a section which is identical to the K-line. The ranges of temperature and salinity which they showed are 1–4℃ and 33.80–34.05‰ respectively. Careful analysis of historical data is required in order to find any stable separation between the NKCW and the ESIW in their T–S properties such as found in 1991.

Acknowledgements

This work is a product of cooperative research between Seoul National University and Korea Hydrographic Office. Graduate students in Ocean Circulation Laboratory, Department of Oceanography, SNU helped to collect data. Captain, officers and crew of the R/V BUSAN-802 extended their professional skills to take high quality data. Thanks are expressed to Dr. Y. ISODA for his comments to improve this paper. This research was supported in part by the Basic Science Research Institute Program, Korea Ministry of Education, 1991. The Korean Science and Engineering Foundation also supported this research for 1991–1993.

References

KAJIURA, K., M. TSUCHIYA and K. HIDAKA (1958): The analysis of oceanographical condition in the Japan Sea. Rep. Develop. Fisher. Resour. *In*: The Tsushima Warm Current, **1**, 158–170.

KIM, C.H. and K. KIM (1983): Characteristics and origin of the cold water mass along the east coast of Korea. J. Oceanol. Soc. Korea, **18**(1), 71–83.

KIM, C.H., H.-J. LIE and K.-S. CHU (1991): On the intermediate water in the southwestern East Sea (Sea of Japan). *In*: Oceanography of Asian Marginal Seas (ed., K. TAKANO), Elsevier Oceanography Series, **54**, 129–141.

KIM, K. and J.Y. CHUNG (1984): On the salinity-minimum layer and dissolved oxygen-maximum layer in the East Sea (Japan Sea). *In*: Ocean Hydrodynamics of the Japan and East China Sea (ed., T. ICHIYE), Elsevier Oceanography Series, **39**, 55–65.

KIM, K., K.-R. KIM, J.-Y. CHUNG and H.-S. YOU (1991): Characteristics of physical properties in the Ulleung Basin. J. Oceanol. Soc. Korea, **26**(1), 83–100.

Maizuru Marine Observatory (1991): Oceanographic Prompt Reports. No. 375: The Prompt Report of the Oceanographic Observations in Japan Sea in May and June, 1991, 29 pp.

MORIYASU, S. (1972): The Tsushima Current. *In*: Kuroshio, its physical aspect (eds., H. STOMMEL and K. YOSHIDA), Univ. of Tokyo Press, 353–369.

UDA, M. (1934): The results of simultaneous oceanographical investigations in the Japan Sea and its adjacent waters in May and June, 1932. J. Imp. Fish. Exp. Station, **5**, 57–190. (in Japanese)

La mer 32: 279–284, 1994
Société franco-japonaise d'océanographie, Tokyo

Oxygen isotope characteristics of seawaters in the Yellow Sea

Dong-Jin KANG*, Chang Soo CHUNG*, Suk Hyun KIM*,
Gi Hoon HONG* and Kyung-Ryul KIM**

Abstract : Due to extremely large variation of temperature and salinity, typically as much as 20℃ in temperature seasonally, it is a difficult task to characterize and classify water masses in the Yellow Sea. We studied $^{18}O/^{16}O$, oxygen isotope characteristics, of seawaters in the area in order to provide additional constraints on the water mass analysis.

Even with large variations in salinity and temperature, isotopic composition of seawaters in summer and winter does not indicate any signficant seasonal difference, showing a simple mixing trend. The contrasting difference observed in T–S and $\delta^{18}O$–S characteristics of surface waters in summer, therefore, reflects the non-conservative nature of temperature in the area, resulted from solar heating at the sea-air interface.

The present study implies that seawaters in the area are, in essence, a mixture of two end-members; isotopically light, fresh waters from precipitation and river discharges (S = 0 ‰, $\delta^{18}O = -7 \sim -9$ ‰) and isotopically heavy, saline waters originated from the East China Sea as a Kuroshio branch (S = 34.40 ‰, $\delta^{18}O$ = 0.2 ‰).

1. Introduction

The Yellow Sea is a typical epicontinental sea, surrounded by the contiguous land masses of Korea and China. With a mean depth of 44m and maximum depth of 105m, it is open to the East China Sea to the south and the Bohai Sea to the north, whose significant portion freezes during winter (GONG, 1989).

The salinity and temperature in the Yellow Sea show enormously large variations as much as 20℃ in temperature between summer and winter time and from 29 ‰ to 35 ‰ in salinity. While several water masses such as Yellow Sea (Bottom) Cold Water (YSCW), Yellow Sea Warm Current Water (YSWCW) and East China Sea Water (ECSW) have been identified as distinct water masses with persistent T–S characteristics, individual investigator often disagrees on the property limits of these waters (LIE, 1984, 1986; PARK, 1985, 1986; KIM *et al.*, 1991). Furthermore, waters along Chinese and Korean coasts were defined rather loosely, reflecting difficulties involved in classification and characterization of water masses in the area.

Oxygen isotope composition, $^{18}O/^{16}O$, of seawater is a classic example of conservative tracers applied to water mass analysis along with temperature and salinity in the ocean (CRAIG and GORDON, 1965). It is also interesting to note that the stable isotope composition is the characteristics of water molecule itself, experiencing little alteration with thermal conditions such as heating or cooling. This property, therefore, can be very powerful in water mass analysis for coastal or shelf waters, where temperature can no longer be a conservative property due to relatively small size of thermal mass (TORGENSEN, 1979).

Oxygen isotope studies have been carried out for the coastal, estuarine waters in the area (ZHANG *et al.*, 1990; WU, 1991). In this paper, we explored the possibility of utilizing this unique tracer for water mass analysis of Yellow Sea waters.

2. Materials and methods

During five oceanographic cruises carried out in the Yellow Sea from 1991 through 1993, 59 stations were occupied as shown in Fig. 1. Water temperature and salinity were measured using a

* Chemical Oceanography Division, Korea Ocean Research & Development Institute, Ansan, P. O. Box 29, Seoul 425-600, Korea
** Department of Oceanography, Seoul National University, Seoul 151-742, Korea

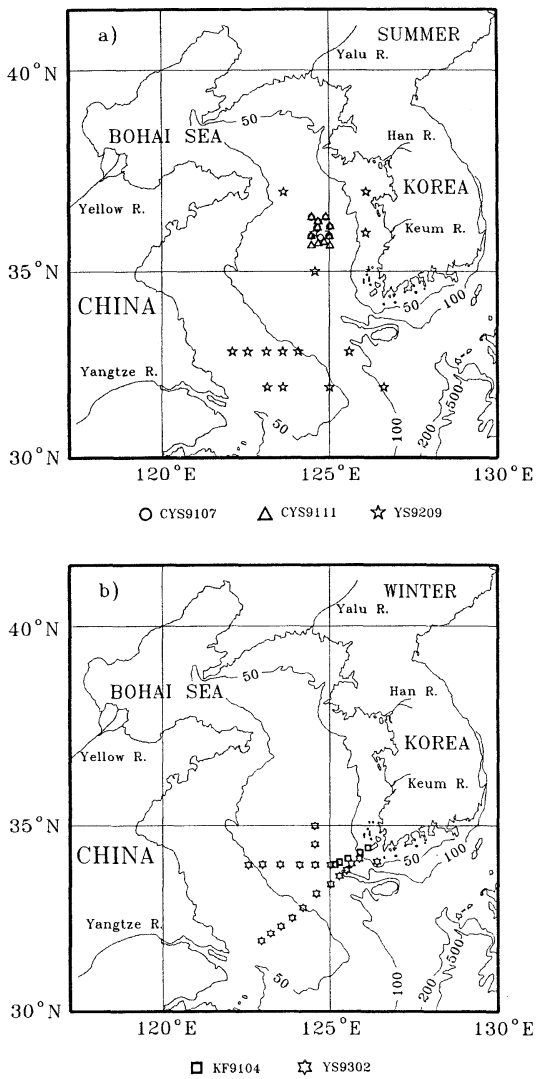

Fig. 1. Maps showing sampling stations in the Yellow Sea. Stations with strong thermocline in summer are grouped in (a), and those with winter characteristics (thoroughly mixed vertically in water column) are grouped in (b). Isobaths in meters.

Seabird SBE-25 CTD system. Water samples were collected with 5 *l* Niskin bottles mounted on a Rosette sampler at standard depths; surface, 10, 20, 30, 50, 75m and near bottom.

The $^{18}O/^{16}O$ ratio of seawater was determined using Isotope Ratio Mass Spectrometer (VG ISOTECH SIRA II) equipped with an automatic H_2O/CO_2 equilibrator (Isoprep 18). The seawater was equilibrated with CO_2 gas inside the equilibrator for 6 hours at 25℃ with mild shaking and isotope ratio of the sample was determined from the observed value for CO_2 gas (EPSTEIN and MAYEDA, 1953).

The oxygen isotopic composition of seawater is compared with SMOW (Standard Mean Ocean Water), and is expressed as $\delta^{18}O$ defined as follows (CRAIG, 1961):

$$\delta^{18}O_{sample} = \left[\frac{(^{18}O/^{16}O)_{sample}}{(^{18}O/^{16}O)_{SMOW}} - 1\right] \times 1000 \ (‰).$$

Twenty samples were analyzed for each run as a batch and 2 to 4 seawater samples used for working standard were included in each batch to control the quality of the measurement. The mean $\delta^{18}O$ of the working standard used in our experiment is -0.12 ‰ $\pm$ 0.08 ‰. The precision of the measurements is $\pm$ 0.13 ‰.

3. Results and discussions

In the Yellow Sea proper with depths less than 100 m, waters are thoroughly mixed vertically in the water column in winter, while strong thermoclines with their depths up to 40 m occur in summer with mixed layers both above and below these thermoclines. Typical examples of CTD profiles representing summer and winter characteristics are shown in Fig.2. Three cruises occupied in July and November, 1991 (CYS9107 and CYS9111) and September, 1992 (YS9209) showed summer characteristics and the rest two carried out in April, 1991 (KF9104) and February, 1993 (YS9302) showed winter characteristics.

The isotopic composition of seawater samples is also shown in the figure, reflecting homogeneous nature in property distribution for each mixed layer, surface mixed layer and deep mixed layer in summer and whole water column in winter. For following discussions, data from samples at 0 and 50 m depths were chosen as representatives for each layer. Henceforth, the surface and deep waters refer to the waters at these selected depths.

Fig. 3 shows the T–S characteristics and $\delta^{18}O$–S characteristics of surface waters and deep waters in summer and winter. Though sampling areas for the present study were not extensive over the Yellow Sea, the T–S distribution reveals

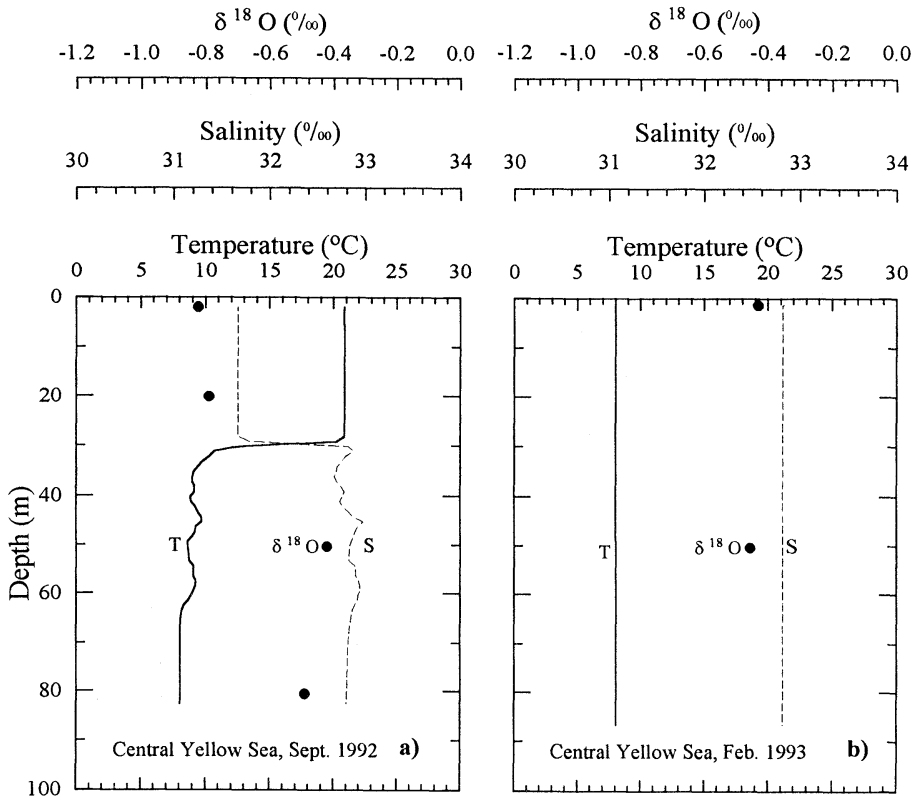

Fig. 2. Typical examples of CTD profiles representing summer characteristics (a) and winter characteristics (b) in the Central Yellow Sea. The $\delta^{18}O$ values of seawater samples are also shown in the figure reflecting homogeneous nature in each mixed layer.

major features such as YSCW, YSWCW and ECSW observed by previous investigations (NAKAO, 1977; KONDO, 1985; KIM *et al.*, 1991).

In summer as stratification occurs, a separation in T–S characteristics between surface waters and deep waters is clear. However, $\delta^{18}O$–S characteristics do not show any significant difference between surface waters and deep waters in summer and also between waters in summer and in winter. This observation, thus, strongly implies that water masses in the Yellow Sea, in essence, do not change seasonally, and that the apparent separation in T–S characteristics between surface and deep waters in summer is primarily due to solar heating at the sea-air interface resulting in very little alteration in isotopic composition.

Furthermore, as shown in Fig. 4, isotopic composition of all these waters, in general, falls on a single mixing trend between less saline and isotopically lighter waters and more saline and isotopically heavier waters, when plotted against salinity. In the figure, the isotopic compositions of Yellow River (Huanghe) estuarine waters (ZHANG *et al.*, 1990), weight-averaged precipitation collected in Korea, China and Japan (KIM and NAKAI, 1988; ROZANSKI *et al.*, 1993), and Kuroshio waters collected in the East China Sea (ONR9202) are also shown.

Major sources for fresh waters in the Yellow Sea are precipitation and discharges from major rivers in the area; the Yellow, Yalu, Han and Keum Rivers. Fresh waters discharged from the Yangtze River (Changjiang) mostly flow southward entering into the East China Sea and its direct influence on the Yellow Sea is minimal (BEARDSLEY *et al.*, 1985). The precipitation over the Yellow Sea is estimated as 4.6×10^{11} m^3/yr (LEE and KIM, 1989), about four times as large as river discharges, $\sim 1.2 \times 10^{11}$ m^3/yr

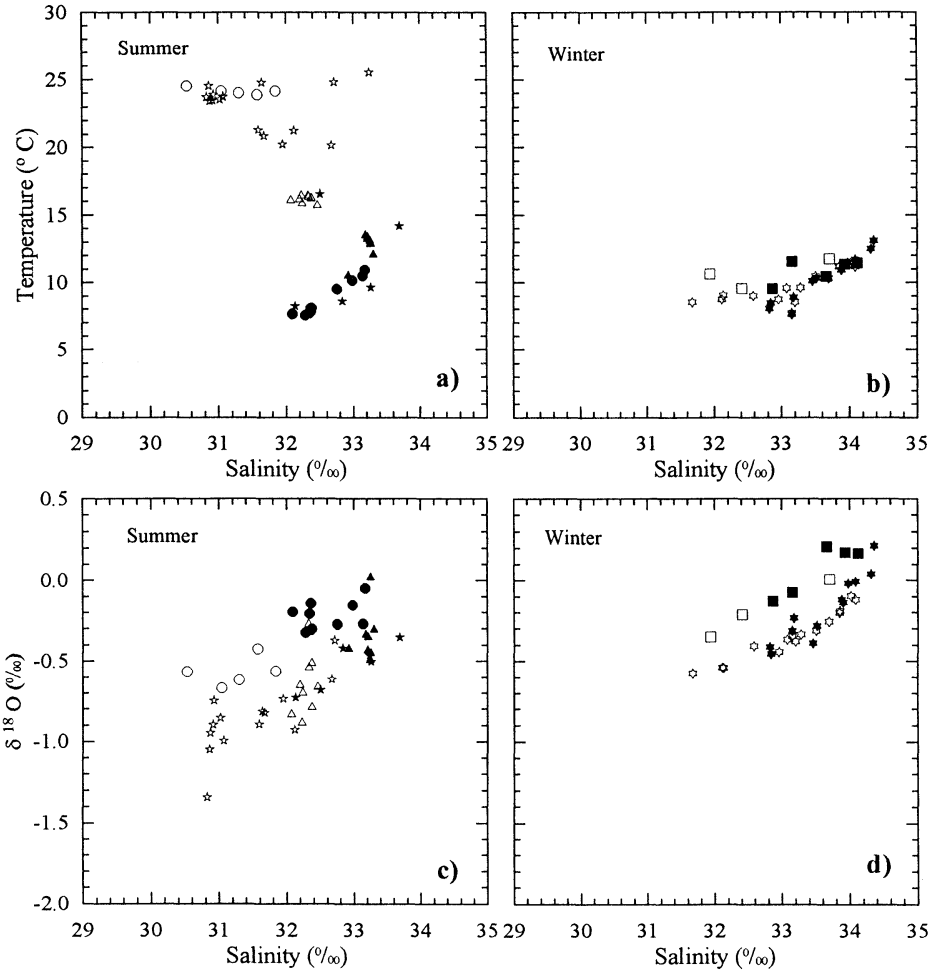

Fig. 3. T–S and $\delta^{18}O$–S diagrams of surface waters and deep waters in summer and winter. Samples at 0 m (open symbols) and 50 m (closed symbols) depths were chosen as representatives for the surface mixed layer and the deep mixed layer, respectively. Symbols represent cruises listed in Figure 1.

(CHOUGH and KIM, 1982; MILLIMAN and MEADE, 1983; WANG and AUBERY, 1987).

The isotopic composition of precipitation in the area ranges from −6.7 to −8.8 ‰ for their weight-averaged values (KIM and NAKAI, 1988; ROZANSKI *et al.*, 1993), even with some seasonal variations, and are very comparable to riverine compositions −7.9 ~ −8.8 ‰ (ZHANG *et al.*, 1990) observed in the Yellow River. As already shown in Fig. 4, these values fit well on the extension of mixing line for the Yellow Sea waters, implying their role as one end-member for the observed mixing trend.

The most saline waters in the Yellow Sea mainly come from the East China Sea as a branch of the Kuroshio current (KONDO, 1985; PARK, 1986; KIM, 1988). The isotopic composition of Kuroshio waters collected in the East China Sea (ONR9202), shown in Fig. 4, clusters well on heavy waters with high salinity and is very comparable to values of Kuroshio waters at the northeast of Taiwan (25°10'N, 121°58.6'E), 0.2 ‰ in $\delta^{18}O$ and 34.40 ‰ in salinity. This observation reflects the role of Kuroshio waters as the other saline and isotopically heavy end-member waters in the Yellow Sea mixing trend.

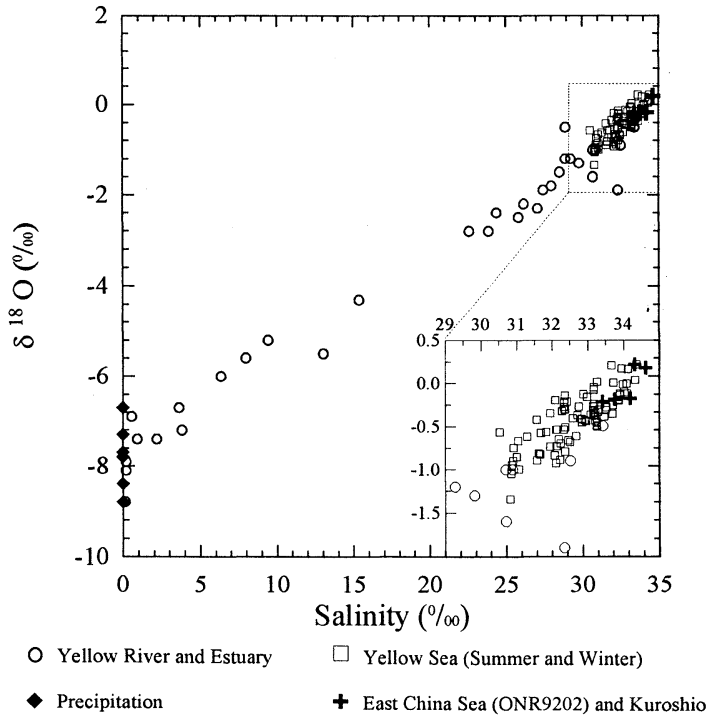

Fig. 4. A δ^{18}O–S diagram of waters in the Yellow River and estuary, Yellow Sea, East China Sea (ONR9202), and precipitation in Korea, China and Japan. The data of the Yellow River estuary taken in May and August, 1985 are from ZHANG *et al.* (1990), and those of the Yellow Sea and East China Sea are obtained in this study. The precipitation data are weight-averaged from KIM and NAKAI (1988) and ROZANSKI *et al.* (1993). The diagrams of the Yellow Sea and East China Sea are redrawn also in an expanded scale.

4. Conclusion

The initial study of oxygen isotopic composition of seawaters in the Yellow Sea revealed that seawaters in the area are, in essence, a mixture of two end-members; isotopically light, fresh waters from precipitation and river discharges (S = 0 ‰, $\delta^{18}O = -7 \sim -9$ ‰) and isotopically heavy, saline waters originated from the East China Sea as a Kuroshio branch (S = 34.40 ‰, $\delta^{18}O$ = 0.2 ‰). The future studies, therefore, need to be focused on quantification of processes determining the mixing ratios in the area.

Furthermore, the contrasting difference observed in T–S and δ^{18}O–S characteristics of surface waters in summer is a mere reflection of non-conservative nature of temperature in the area, resulted from solar heating at the sea-air interface; strongly implying that water mass analysis in the Yellow Sea with T–S characteristics must be exercised with caution due to their non-conservativeness. The effect of solar heating can also be confirmed and normalized by pCO_2 measurement in surface waters especially in summer and winter (WEISS *et al.*, 1982; FUSHIMI, 1987); this type of research in the area is one of the important topics to be explored in the future.

The isotopic composition of precipitation and river waters is rather loosely known at the present time, which may also be a reason for scattering of data. Further refinement is needed to apply this tracer in a more quantitative way.

Acknowledgments

This work was supported by Ministry of Science and Technology (BSPN00203), and also in part by Basic Sciences Research Institute Program, Ministry of Education, Korea, 1991 for K. -R. KIM. We thank Dr. C. -H. WANG and

Dr. K. K. LIU at Academia Sinica, Taiwan for providing the Kuroshio water samples. We express our appreciation to Prof. Y. HORIBE and Prof. D. S. LEE at Yonsei University for reviewing and improving our manuscript. Prof. HORIBE, especially, helped us to pay our attention to the importance of pCO_2 study in the future. Prof. K. KIM at Seoul National University provided encouragement and invaluable criticism during paper preparation.

References

BEARDSLEY, R. C., H. Y. LIMEBURNER and G. A. CANNON (1985): Discharge of the Changjiang (Yangtze River) into the East China Sea. Cont. Shelf Res., **4**, 57–76.

CHOUGH, S. K. and D. C. KIM (1981): Dispersal of fine-grained sediments in the southeastern Yellow Sea: A steady state model. J. Sed. Pet., **51**, 721–728.

CRAIG, H. (1961): Standard for reporting concentrations of deuterium and oxygen-18 in natural water. Science, **133**, 1833–1834.

CRAIG, H. and L. I. GORDON (1965): Deuterium and oxygen-18 variations in the ocean and the marine atmosphere. *In*: Stable isotopes in oceanographic studies and paleotemperatures (ed. E. TONGGIORGI), Spoleto Conf. Proc. 9–130.

EPSTEIN, S. and T. MAYEDA (1953): Variation of O^{18} content of waters from natural sources. Geochim. Cosmochim. Acta, **4**, 213–224.

FUSHIMI, K. (1987): Variation of carbon dioxide partial pressure in the western North Pacific surface water during the 1982/83 El Niño event. Tellus, **39B**, 214–227.

GONG, J. (1989): Satellite remote sensing of sea-ice and its operational monitoring method along the coast of China. Acta Oceanol. Sinica, **8**, 379–390.

KIM, K. (1988): Hydrography and currents in the Yellow Sea and the northern East China Sea. *In*: Proc. symp. on development of marine resources and international cooperation in the Yellow Sea and the East China Sea (ed. Y.-B. GO), Cheju National Univ., 19–30.

KIM, K., K.-R. KIM, T. S. RHEE, H. K. RHO, R. LIMEBURNER and R. C. BEARDSLEY (1991): Identification of water masses in the Yellow Sea and the East China Sea by cluster analysis. *In*: Oceanography of Asian Marginal Seas (ed. K. TAKANO), Elsevier, 253–267.

KIM, K. H. and N. NAKAI (1988): Isotopic compositions of precipitations and groundwaters in South Korea. J. Geol. Soc. Kor., **24**, 37–46. (in Korean)

KONDO, M. (1985): Oceanic investigation of fishing grounds in the East China Sea and Yellow Sea I. Bull. Seikai Reg. Fish. Res. Lab., No. 62.

LEE, G. T. and K. KIM (1989): A study on the eddy diffusion of salinity in the lower layer of the Yellow Sea. Yellow Sea Res., **2**, 21–29. (in Korean)

LIE, H. -J. (1984): A note on water masses and general circulation in the Yellow Sea (Hwanghae). J. Oceanol. Soc. Kor., **19**, 187–194.

LIE, H. -J. (1986): Summertime hydrographic features in the southeastern Hwanghae. Prog. Oceanogr., **17**, 229–242.

MILLIMAN, J. D. and R. H. MEADE (1983): Worldwide delivery of river sediment to the ocean. J. Geol., **91**, 1–21.

NAKAO, T. (1977): Oceanic variability in relation to fisheries in the East China Sea and the Yellow Sea. J. Fac. Mar. Sci. Tech., Sp. No., 199–367.

PARK, Y. H. (1985): Some important summer oceanographic phenomena in the East China Sea. J. Oceanol. Soc. Kor., **20**, 12–21.

PARK, Y. H. (1986): Water characteristics and movements of the Yellow Sea Warm Current in summer. Prog. Oceanogr., **17**, 243–254.

ROZANSKI, K., L. ARAGUAS-ARAGUAS and R. GONFIANTINI (1993): Isotopic patterns in modern global precipitation. *In*: Climate change in continental isotopic records (eds. P.K. SWART, K. C. LOHMANN, J. MCKENZIE and S. SAVIN), Geophysical Monograph, **78**, AGU, 1–36.

TORGENSEN, T. (1979): Isotopic composition of river runoff on the U. S. east coast: evaluation of stable isotope versus salinity plots for coastal water mass identification. J. Geophys. Res., **84**, 3773–3775.

WANG, Y. and D. G. AUBERY (1987): The characteristics of the China coastline. Cont. Shelf Res., **7**, 329–349.

WEISS, R. F., R. A. JAHNKE and C. D. KEELING (1982): Seasonal effects of temperature and salinity on the partial pressure of CO_2 in sea water. Nature, **300**, 511–513.

WU, S. -Y. (1991): Oxygen isotope compositions of seawaters in the Huanghai (Yellow) Sea and the Bohai Sea. Sci. in China (Ser. B), **34**, 327–337.

ZHANG, J., R. LETOLLE, J. M. MARTIN, C. JUSSERAND and J. M. MOUCHEL (1990): Stable oxygen isotope distribution in the Huanghe (Yellow River) and the Changjiang (Yangtze River) estuarine system. Cont. Shelf Res., **10**, 369–384.

La mer 32: 285–293, 1994
Société franco-japonaise d'océanographie, Tokyo

Interannual SST variations to the north and south of the polar front in the Japan Sea

Yutaka ISODA*

Abstract: Interannual variations of the sea surface temperature (SST) in the Japan Sea and its relationship with the inflow variations of the Tsushima Current were investigated by using 20 years (1971–1990) long, 1°grid SST data along the 134°E meridian and sea level difference data across the Tsushima/Korea and Tsugaru Straits. The SST is closely related to the formation of a thin surface layer in summer, and of a thick mixed layer in winter. Therefore, the winter SST is suitable for research of the long-term variability of subsurface waters to the north and south of the polar front in the Japan Sea. Interannual SST variations in winter have two dominant periods: decadal and 2–4 years period.

The SST variation with decadal period is predominant in the area north of the polar front and seems to be correlated to the inflow variation of the Tsushima Current. The SST variation with 2–4 years period tends to appear almost simultaneously throughout the polar front and to its north and south, and has no significant correlation to the inflow variations of the Tsushima Current. It may be influenced by the outbreaks of the Asian winter monsoon.

1. Introduction

The Tsushima Current carries heat and water mass northward through the Tsushima/Korea Strait and creates the warm subsurface layer throughout the basin south of the oceanic thermal front, i.e. the polar front in the Japan Sea (Fig.1(a)). This warm current is known to exhibit large variability not only with seasonal period but also with various interannual periods. TOBA *et al.*(1982) showed that the Tsushima Current is caused by the sea level difference between the East China Sea and the sea east of the Tsugaru Strait and exhibits large interannual variations as well as apparent seasonal ones. By using coastal SST data, WATANABE *et al.* (1986) found that two kinds of SST variations with 10 and 6 years period are dominant along the Japanese coast. Based on hydrographic surveys from 1953 to 1982, NAGANUMA(1985) suggested that variations with a 6-year periodicity are found to be related to the flow patterns of the Tsushima Current. MIITA and TAWARA(1984) showed that a 6- to 7-year periodicity of water temperature is also predominant at the Tsushima/Korea Strait.

Thus, the previous studies were based on water temperature data in the Tsushima Current region, i.e., the region south of the polar front. Water temperature variations north of the polar front are not well understood yet. Our poor knowledge of the northern area oceanography is a serious problem, because the Tsushima Current system associated with the density structure is related to the contrast between the cold northern and the warm southern waters across the polar front. It is important to clarify the relation between both waters for understanding not only the horizontal circulations in the Japan Sea, but also the polar front genesis.

Unfortunately, long-term continuous hydrographic data of the Russian sea area are not available. A useful approach to studying the thermal structure of the northern Japan Sea is to focus on the SST variations, which reflect the ocean conditions due to the development of the surface mixed layer in winter. The Japan Meteorological Agency (JMA) has collected SST data with ship and satellite observations and averaged them over a 1°grid. If no data are available in a 1° box, the JMA calculates the weighted mean of the 5 data at the nearest

* Department of Civil and Ocean Engineering, Ehime University, Matsuyama 790, Japan
Present affiliation: Faculty of Fisheries, Hokkaido University, 3-1-1, Minato-cho, Hakodate 041, Japan

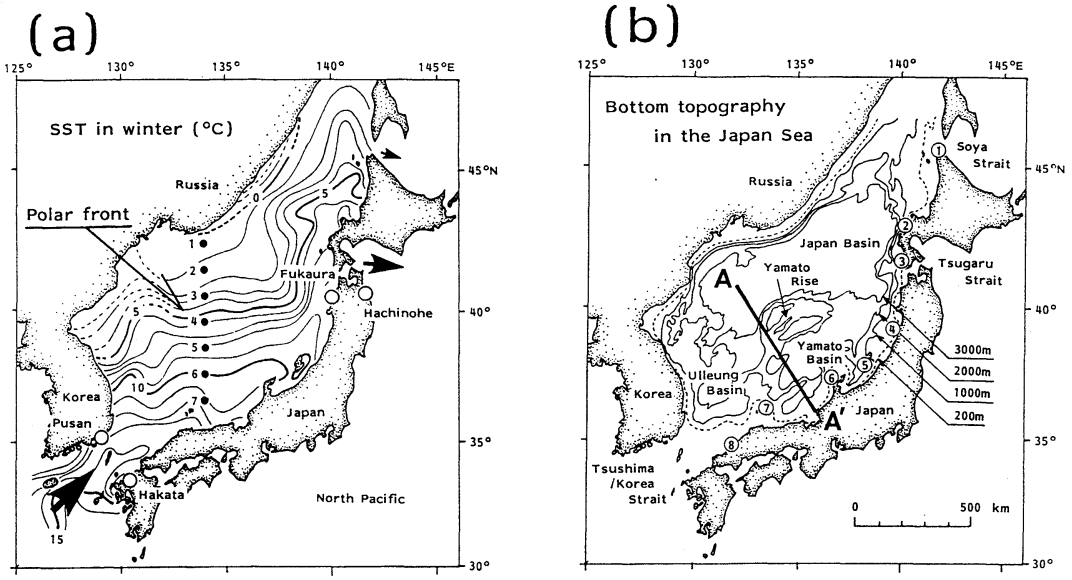

Fig. 1 (a) Seasonal mean thermal map in winter at the surface layer (JODC, 1978) and the grid points of SST (●) and sea level (○). (b) Bathymetric chart of the Japan Sea. A–A' line shows CTD observation line of the Maizuru Marine Observatory. Numerals in open circles show the station numbers of the coastal SST observation (WATANABE *et al.*, 1986).

sites with a weight w defined by $w=exp(-(d/200km)^2)$ (d: distance) and uses it as the monthly mean in that box. This procedure is applied to not a few boxes in the northern Japan Sea, particularly in winter months. However, poor spatial and temporal density of available data do not make nonsense of the study on the northern Japan Sea, if confined into comparison of the regional characteristics on both sides of the polar front rather than concerned with general description of hydrography in the individual region. The purpose of the present study is to describe interannual SST variations, and to find the relation between the north-south water mass variations and the inflow variations of the Tsushima Current.

2. Data

SST data

Figures 1(a) and (b) show the mean SST distribution in winter (JODC, 1978) and the bottom topography, respectively. Surface isotherms in the central Japan Sea tend to be directed zonally and the polar front is formed along about 40° N latitude. ISODA *et al.*(1991) revealed that a part of the front corresponds with the location of a warm eddy above the Yamato Rise. ISODA and NISHIHARA(1992) showed that this warm eddy seems to be affected by the bottom topography and stably exists above the Yamato Rise throughout the year. Therefore, the SST variation in the meridional direction passing through the Yamato Rise is useful for describing the north-south thermal structures on both sides of the polar front. In this context, we use monthly mean SST data along 134° E meridian (JMA, 1971–1990) for recent 20 years. Grid points 1 to 7 are defined for the analysis as shown in Fig. 1(a).

Sea level data

Yearly mean sea level data at Hakata, Fukaura and Hachinohe by the Geographical Survey Institute, Ministry of Construction, Japan (1991) and at Pusan by the Hydrographic Office of the Republic of Korea (1970–1991) are collected. Locations of these tidal stations are indicated by the open circles in Fig.1(a). Variations of the inflow volume transport or surface current velocity through the Tsushima/Korea Strait and the outflow through the Tsugaru Strait are investigated by examining the sea level difference between Hakata and Pusan and

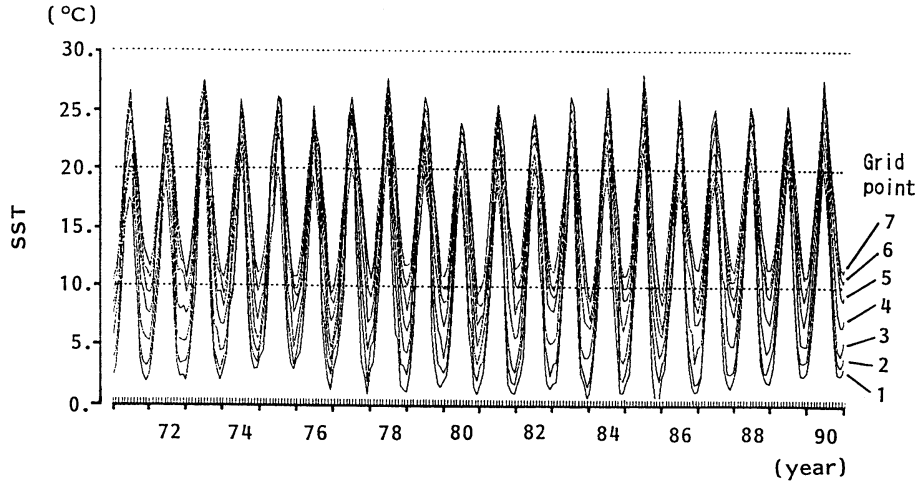

Fig.2. The time series of the monthly mean SST from grid points 1 to 7 for 20 years (1971–1990).

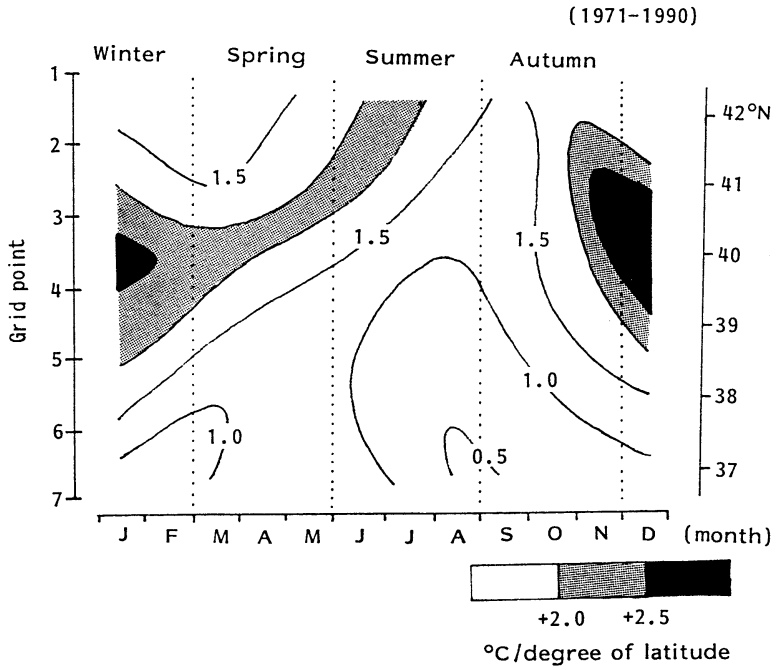

Fig. 3. The 20 years averaged time (seasonal)-latitude diagram of the southward gradient of the monthly mean SST along 134°E meridian.

between Fukaura and Hachinohe, respectively.

3. Characteristics of the seasonal SST variation

Figure 2 shows the time series of monthly mean SST during 20 years at grid points 1 to 7. One remarkable feature is a significant seasonal signal, e.g., maximum in summer and minimum in winter. The other is that the envelopes of the maximum and minimum SST indicate interannual features. The summer SST is significantly higher in 1973, 1978, 1985 and 1990 than in the other years, while the winter SST is higher from 1971 to 1976 and 1986 to 1990 than from 1977 to 1985.

A time-latitude diagram of SST front averaged over 20 years is drawn in Fig.3 for studying

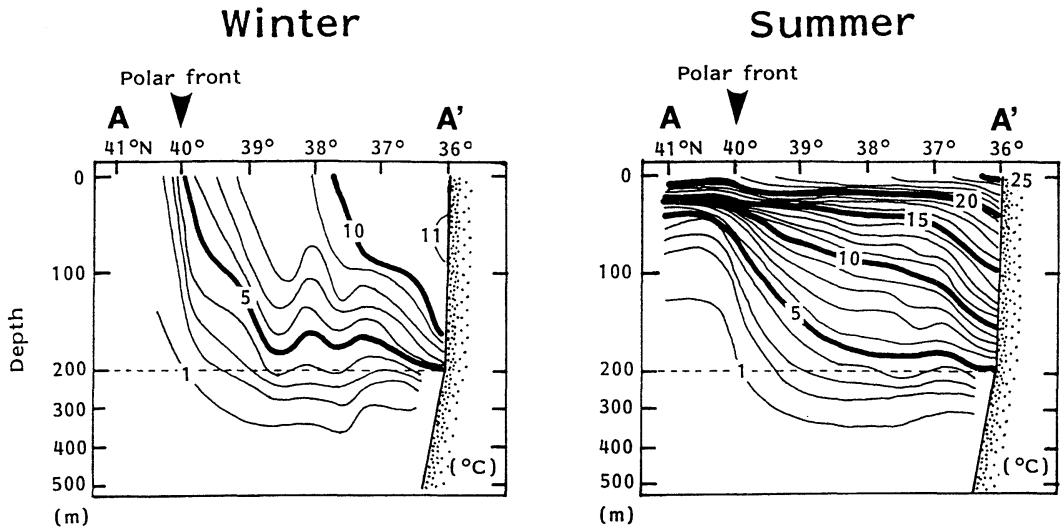

Fig. 4. Seasonal mean vertical sections of water temperature in winter and summer along A–A' line in Fig.1 (b) (MINAMI *et al.*, 1987).

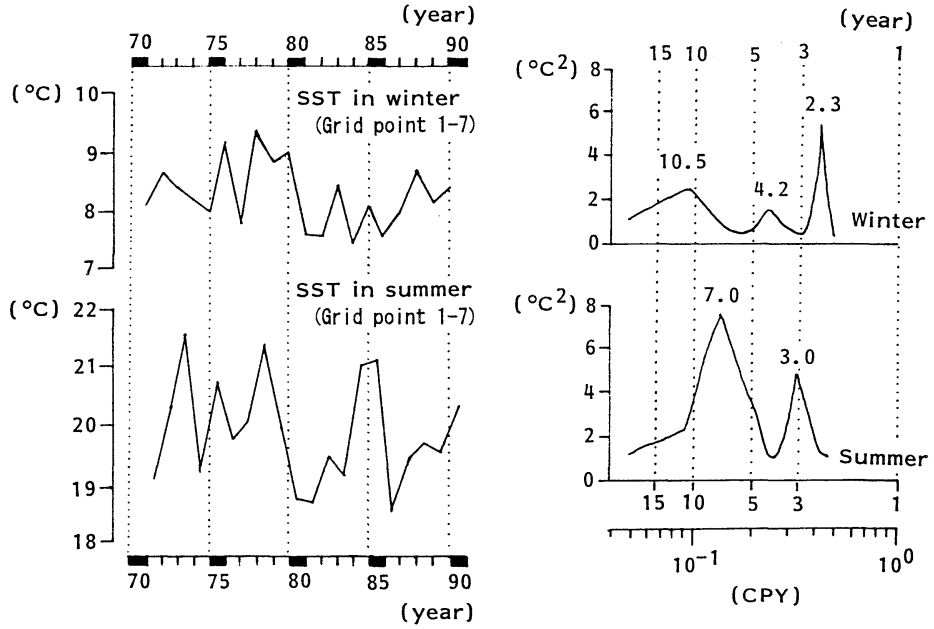

Fig. 5. The time series of SST in winter and summer averaged over grid points 1 to 7 and the SST spectra for both seasons.

the seasonality of the SST. The SST front is defined as the band where the SST gradient is sharper than 2.0℃/degree of latitude on the monthly mean. In the heating season from March onwards, the thermal frontal zone gradually migrates northward as a result of warming of surface water and disappears in August. In the cooling season from October onwards, the zone width abruptly increases at latitudes from 39 to 42° N. From December to February, the thermal frontal zone stagnates around 40° N. Figure 4 is redrawn from seasonal mean maps obtained from hydrographic measurements in 1964–1983 by the Maizuru Marine Observatory

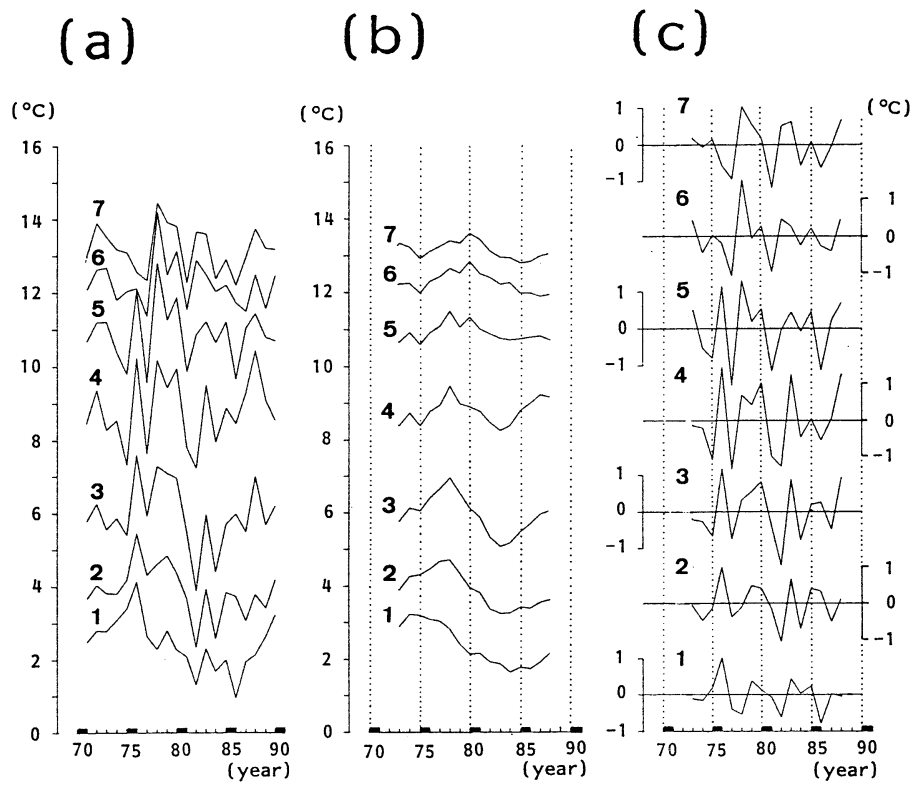

Fig. 6. Time series of SST raw data in winter (a) and those of low-passed (b) and high-passed (c) SST data with the 7-year running mean filter.

(MINAMI *et al.*, 1987). It shows the vertical sections of water temperature in winter and summer along A–A' line in Fig. 1(b). The summer SST is closely related to the formation of a thin surface layer, whereas the winter SST is strongly affected by subsurface waters due to the deepening of the surface mixed layer. It is also found that the polar front stably exists around 40° N in both seasons. From these figures, we can regard the stagnated thermal SST front at 40° N in Fig. 3 as the wintertime outcrop area of the polar front. Therefore, the SST distribution in winter will give us information on characteristics of the subsurface waters. In the present study, we analyze the wintertime SST data averaged over December to February to describe the interannual variations of the north-south thermal structure in the Japan Sea.

Before the analysis of the winter SST data, we describe the characteristics of temporal winter and summer SST fluctuations. Figure 5 shows the time series of SST in winter (December to February) and summer (June to August) averaged over grid points 1 to 7 and their SST spectra. The Maximum Entropy Method (MEM) was used because of advantage of treating the present short-length time series. It is clear that SST variations with 2–4 years and 10 years period (hereafter referred to as the decadal variation) are prevailing in winter, whereas those with 3 years and 7 years period are dominant in summer. It can be said that the decadal periodicity is a cooling-season mode and the 7-year periodicity is a heating-season mode which is restricted in a thin surface layer.

4. Interannual variations of the SST in winter

In the SST spectrum in winter, we detect two remarkable spectral peaks around 2–4 years and about 10 years. In the following analysis, we divide the data into two categories with these two periods by using the 7-year running mean filter. Figure 6 shows the time series of the raw SST data in winter (a), their low-passed SST data

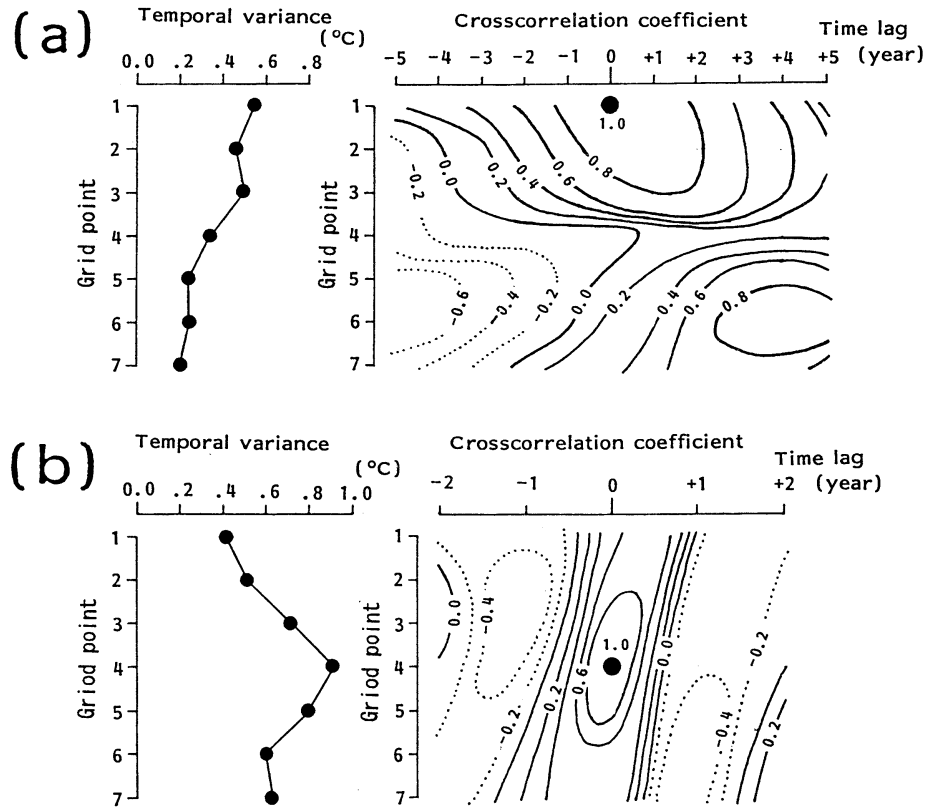

Fig. 7. Temporal SST variance at each grid point (left panels) and cross-correlation coefficients between a grid point with the maximum variance and the other grid points for 1972–1988 (right panels); (a) decadal variation and (b) 2–4 years variation.

(b) and the high-passed SST data (c) at each grid point. It is evident that the decadal SST variation is larger at the northern grid points (Fig.6(b)) and the SST variation with 2–4 years period exhibits a wavy pattern common to all grid points (Fig. 6(c)). We apply the cross-correlation analysis to each SST variation in order to extract the dominant spatial/time variation patterns.

Figure 7 shows the cross-correlation coefficients among the time series at all grid points for the two periods. The amplitude of temporal SST variance at each grid point indicates the spatial predominance. The distribution of cross-correlation coefficients represents time lags between a grid point with the maximum variance and the other grid points. The significant signal with decadal period is found in the area north of the polar front (grid points 1 to 3) with a distinct time lag of 3–4 years to the south (Fig. 7(a)). However, we cannot verify this time lag because the data is not long enough to discuss the decadal variation in detail. The SST signal with 2–4 years period is relatively strong around the polar front (grid points 3 to 5) with a small time lag less than 1 year to the north (Fig. 7 (b)).

5. Relationship between the north-south SST variations and the inflow variations of the Tsushima Current

Figure 8 shows the time series of SST variation with decadal period and yearly mean sea level differences at the entrance (Hakata–Pusan) and exit (Fukaura–Hachinohe) straits. Surprisingly, the decadal signal of the sea level difference is dominant rather than the signal with several years period. Furthermore, the dominant SST variation at grid points 1 to 4 appears to be negatively correlated with the sea

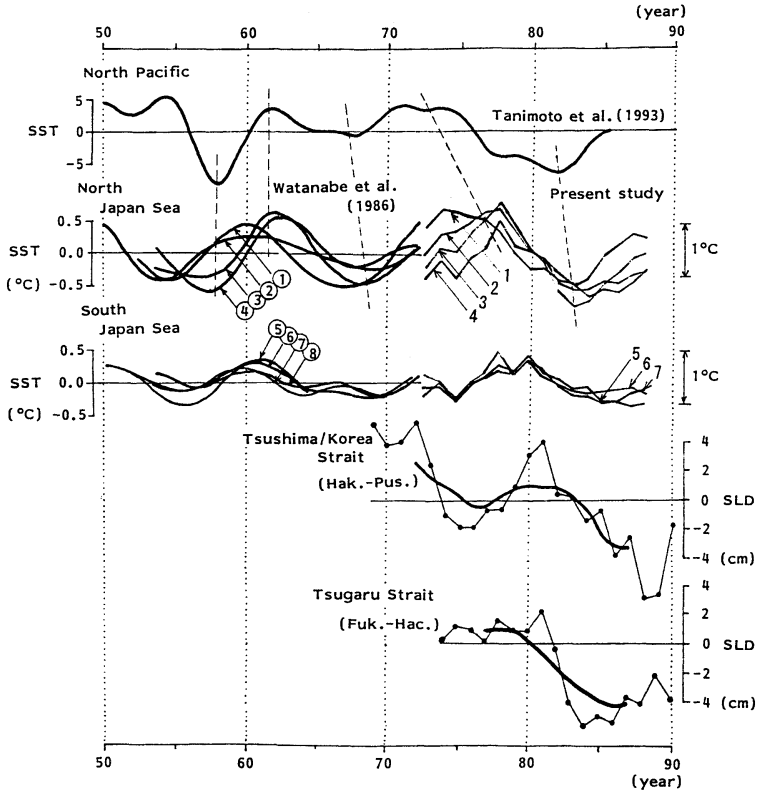

Fig. 8. Time series of decadal SST variations over the North Pacific (after TANIMOTO *et al.*, 1993) along the Japanese coast (after WATANABE *et al.*, 1986) and along 134° E meridian (present study). Lower two figures show the interannual variations of yearly mean sea level differences at the Tsushima/Korea and Tsugaru Straits. Heavy lines show the 7-year running means of the sea level difference.

level differences, especially across the Tsushima/Korea Strait. It seems that the year of increasing (decreasing) inflow volume transport or surface current velocity through the Tsushima/Korea Strait corresponds to that of decreasing (increasing) SST in the northern Japan Sea.

WATANABE *et al.*(1986) obtained SST signals with a similar time scale by use of SST data from 1950 to 1972 at coastal stations shown in Fig.1(a), and showed the SST variation pattern at northern grid points is different from that at southern grid points, as redrawn in the middle panels in Fig.8. TANIMOTO *et al.*(1993) indicated that the dominant decadal SST variability over the North Pacific is associated with the Pacific/North American (PNA) anomaly pattern in the troposheric circulation. The time coefficients of their decadal mode (the 1st mode of Empirical Orthogonal Function (EOF)) are also redrawn at the top panel in Fig.8. The variation pattern of their time coefficients is similar to that of the SST in the northern Japan Sea with a time lag of several years. It is worthwhile to note that the SST variation in the Japan Sea with decadal time scale may be influenced, either directly or indirectly, by the ocean-atmosphere interactions over the North Pacific.

Figure 9 shows a time series of the Asian winter monsoon index (MOI) redrawn from BINGHAM *et al.*(1992), the SST variation with 2–4 years period averaged over grid points 4 to 7 and the sea level differences at the entrance and exit straits, respectively. The SST variation coincides well with the MOI. This result shows that stronger outbreaks of cold air in winter are responsible for the lower SST period. However, there is no significant relationship between this SST variation and the inflow variation of the

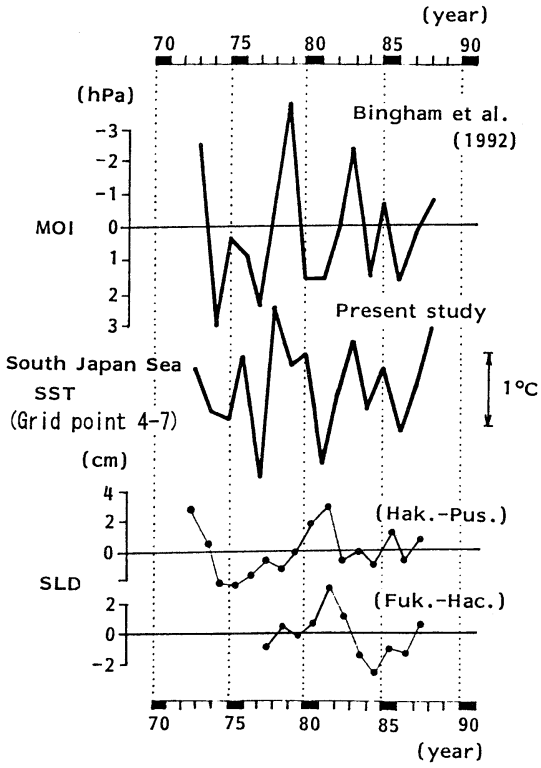

Fig. 9. Time series of MOI in winter (after BINGHAM *et al.*, 1992), and of variation with 2–4 years period averaged over grid points 4 to 7. Lower two figures show the interannual variations of yearly mean sea level difference at the Tsushima/Korea and Tsugaru Straits, which are high-passed with the 7-year running mean filter.

Tsushima Current with the same time scale.

6. Conclusions and discussion

In the present study, we have investigated the interannual SST variations in the Japan Sea and their relationship with the inflow variations of the Tsushima Current. The analysis of the seasonal SST variation confirms that the SST in winter is strongly affected by prominent thick mixed waters and, therefore, is useful to studying the interannual variations of subsurface waters in the Japan Sea. Interannual SST variations in winter have decadal and 2–4 years periods.

The SST variation with decadal period is especially dominant in the northern area of the polar front in the Japan Sea and seems to be correlated to the inflow variation of the Tsushima Current. This variation is, in turn, related to the large-scale SST variation over the North Pacific, though the linkage mechanism is still unclear (and out of the scope of the present study). The SST variation with 2–4 years period tends to appear almost simultaneously throughout the polar front and to its north and south, and has no significant correlation to the inflow variation of the Tsushima Current. The strengthening of the Asian winter monsoon is responsible for the remarkable SST decrease.

These facts suggest that the interannual variations of the eastward mean flow of the Tsushima Current is closely related with those of the SST difference between both sides of the polar front. In the decadal variation, the large north-south difference of the SST increases the eastward density flow in the polar frontal region, both of which correspond to increasing inflow from the Tsushima/Korea Strait. On the other hand, the inflow variation with 2–4 years period disappears because of the small north-south SST difference. Thus, the different ocean response depending on interannual periodicity will be an important physical aspect of the Tsushima Current system associated with the north-south density structure.

The variations with 6–7 years period were generally found in the previous studies mentioned in the introduction, but in the present study were not detected as sharp SST signal in winter. This may be primarily due to the difference of the analyzed data: namely the previous studies used the summer hydrographic data (NAGANUMA, 1985) or monthly mean anomaly SST data (WATANABE *et al.*, 1986), and were concerned with the east-west patterns of the Tsushima Current along the Japanese coast. Since the variation with 6–7 years period is seen in a thin summer surface layer, the primary energy source of it may be the heat stored in the surface layer in summer. To clarify this variation and its mechanism, further studies on the water mass formation along the Tsushima Current will be needed in relation to the atmospheric heating.

Acknowledgements

The author would like to thank Prof. T. YANAGI for helpful comments and discussion, Dr. N. SHISHIDO, Mr. K. OKAMURA of the Matsuyama Meteorological Observatory, Dr. T. MURAYAMA of the Shimane Prefectural Experimental Fishery Station and Dr. A. ISOBE of Shimonoseki University of Fishery for providing him the SST data collected by the JMA. He appreciates the editor and reviewers for their critical comments and suggestions. Thanks are also extended to Dr.H.C.HOON of Toug-Yeoung National Fisheries Junior College, who kindly provided him monthly mean sea level data at Pusan. The data analysis was carried out on a FACOM-770 of the Computer Center of Ehime University.

References

BINGHAM, F. M., T. SUGA and K. HANAWA (1992): Comparison of upper ocean thermal conditions in the western North Pacific between two pentads: 1938-42 and 1978-82. J. Oceanogr., **48**, 405-425.

Geographical Survey Institute, Ministry of Construction, Japan (1991): Tables and graphs of annual mean sea level along the Japanese coast 1894-1990. 83pp.

Hydrographic Office of the Republic of Korea (1970-1991): Technical reports. Results of tidal observation (1969-1990).

ISODA, Y. and M. NISHIHARA (1992): Behavior of warm eddies in the Japan Sea. Umi to Sora, **67**, 53-65. (in Japanese)

ISODA, Y., S. SAITOH and M. MIHARA (1991): SST structure of the polar front in the Japan Sea. *In*: Oceanography of Asian Marginal Seas, Elsevier Oceanogr. Ser., 54, (ed. K.Takano), Elsevier, Amsterdam, 103-112.

Japan Meteorological Agency (1971-1990): The ten-day marine report.

Japan Oceanographic Data Center [JODC] (1978): Marine Environment Atlas, Northwestern Pacific Ocean II (seasonal and monthly). Japan Hydrogr. Association, Tokyo, 147pp.

MIITA, T. and S. TAWARA (1984): Seasonal and secular variations of water temperature in the East Tsushima Strait. J. Oceanogr. Soc. Japan, **40**, 91-97.

MINAMI, H., Y. HASHIMOTO, Y. KONISHI and H. DAIMON (1987): Statistical features of the oceanographic conditions in the Japan Sea. Umi to Sora, **62**, 163-175.

NAGANUMA, K. (1985): Fishing and oceanographic conditions in the Japan Sea. Umi to Sora, **60**, 89-103. (in Japanese)

TANIMOTO, Y., N. IWASAKA, K. HANAWA and Y. TOBA (1993): Characteristic variations of sea surface temperature with multiple time scale in the North Pacific. J. Clim., **6**, 1153-1160.

TOBA, Y., K. TOMIZAWA, Y. KURASAWA and K. HANAWA (1982): Seasonal and year-to-year variability of the Tsushima-Tsugaru Warm Current System with its possible cause. La mer, **20**, 41-51.

WATANABE, T., K. HANAWA and Y. TOBA (1986): Analysis of year-to-year variation of water temperature along the coast of the Japan Sea. Prog. Oceanogr., **17**, 337-357.

La mer 32: 295–306, 1994
Société franco-japonaise d'océanographie, Tokyo

A numerical simulation of oil spill in the Seto-Inland Sea

Shin-ichi SUGIOKA*, Takashi KOJIMA*,
Kisaburo NAKATA** and Fumio HORIGUCHI**

Abstract: A 3-D oil spill model is used for simulating the fate of oil spilled from an accident which happened at Mizushima on the Seto-Inland Sea in December 1974. The model calculates time evolution of the partition of spilled oil to surface oil slick, entrainment into the underlying water column and sedimentation on the bottom, with empirical formulae derived from laboratory experiments. The simulated distribution of oil spreading agrees fairly well with visual observations from aircrafts.

1. Introduction

The spilled oil in the sea changes its physico-chemical properties with time (MACKAY and MCAULIFFE, 1988). Main processes affecting spilled oil are schematically shown in Fig.1. The oil is weathered with time due to various processes such as evaporation, entrainment, emulsification and biodegradation.

Advection is caused by both wind and water currents. It is calculated as the vector sum of a wind-induced drift and water current-induced drift.

For many years, Fay's three-regime spreading theory (FAY, 1971) has been commonly used for spreading which determines the aerial extent of spilled oil.

Evaporation transfers 20–40% of spilled oil from the sea surface to the atmosphere within several days, depending on the type of oil (REED, 1992). Although highly refined oil loses 75% or more of its volume through evaporation within a matter of days (SHEN *et al.*, 1991), C heavy oil dealt with in the present paper contains it very little, so that no evaporation of it is considered. Subsequent evaporation is treated together with biodegradation. Loss rate due to evaporation and biodegradation is specified as a constant of 10% per day.

Subject to wind and waves, oil on the sea surface is entrained into the underlying water column. Entrainment, strongly dependent on the turbulence and sea state, is described by an equation derived from a mixing length theory and a finite amplitude wave theory. The parameters in that equation are specified with an empirical formula (HORIGUCHI *et al.*, 1991).

The formation of water-in-oil emulsions (or mousse) depends on the oil composition and sea state. Emulsified oil in the form of micrometer-sized dispersed droplets can contain water as much as 80% of its mass. The entrainment rate of water into oil slick is specified with a formula by MACKAY *et al.* (1979). Increase of oil viscosity with time governing the entrainment rate is specified with a relationship between the viscosity and water content by MACKAY *et al.* (1981). The rate of water content increase with time is given by a JOIA report (1988). The oil-in-water emulsification process is ignored because it is not significant for C heavy oil.

These various processes interact with each other in a complex way. The model used here (called SPILOR) is composed of several submodels as shown in Fig. 2. In this model, behavior of oil spill is described by an advection-diffusion equation with processes of floating, sinking, entrainment, emulsification, evaporation and biodegradation. Bond's formula is used for floating process, and Stokes's formula for sinking process (JOIA, 1988). The equations are solved by using finite difference method. Details of the model structure are described in another paper (HORIGUCHI *et al.*, 1991)

* Fuyo Ocean Development & Engineering Co., Ltd., 1-8-2, Torigoe, Taitou-ku, Tokyo, 111 Japan
**National Institute for Resources and Environment, Onogawa, Tsukuba, 305 Japan

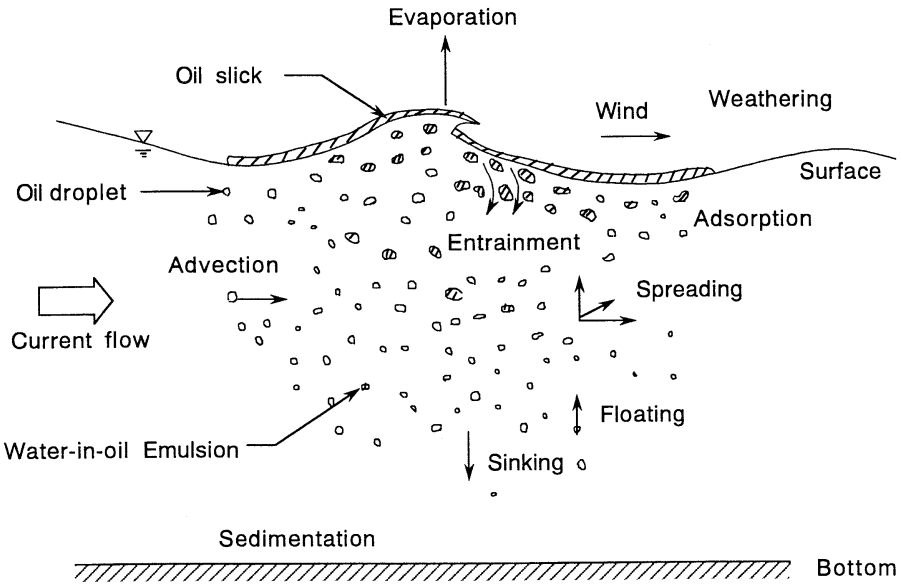

Fig. 1. Oil spill processes.

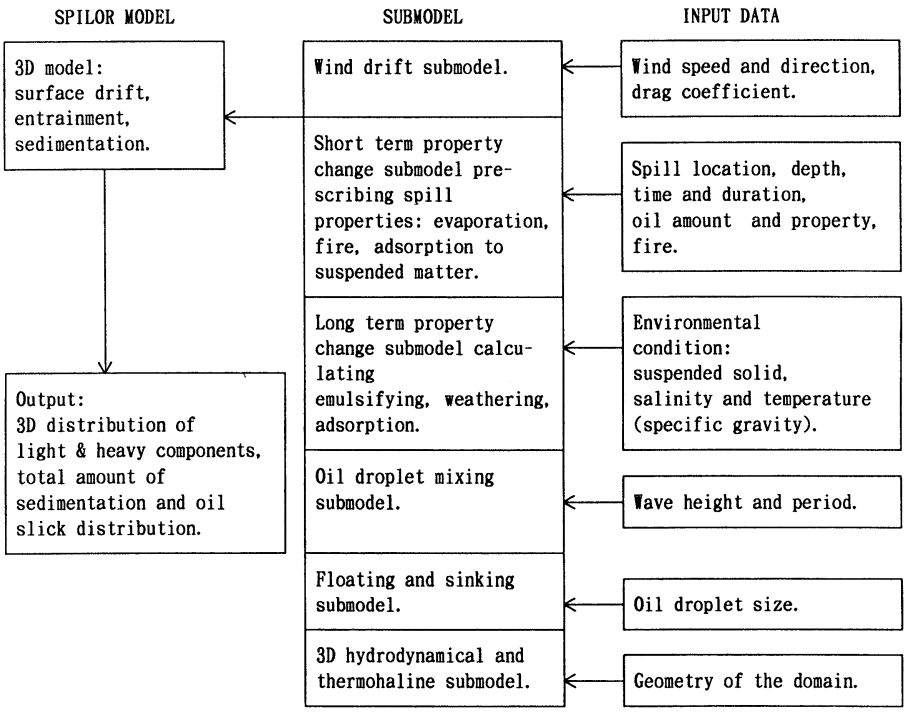

Fig. 2. Structure of the model (SPILOR).

2. Application of the SPILOR to the Seto-Inland Sea

The model is applied to an oil spill accident in the Seto-Inland Sea which occurred at Mizushima oil plant of Mitsubishi Petroleum Corporation at 21:00 on Dec. 18, 1974. The En-

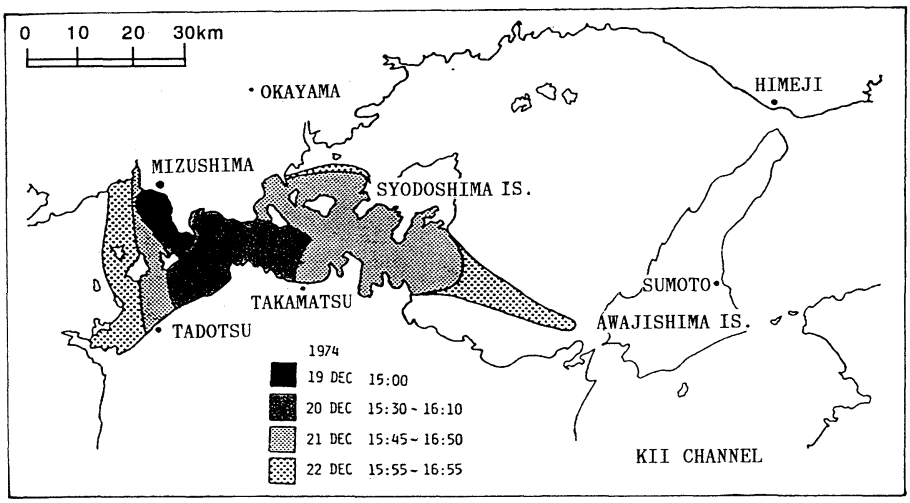

Fig. 3. Transition of oil spreading area visually observed from aircrafts of the 5th and 6th Regional Maritime Safety Headquarters. (YANAGI and OKAMOTO, 1984)

vironment Agency estimates an amount of 7500~9500kl C heavy oil was spilled (Environment Agency, 1975). The spread of oil from 19 to 22 Dec. 1974 is shown in Fig. 3 (YANAGI and OKAMOTO, 1984), where spreading area is determined with visual data from aircrafts. The oil concentration is not reported, however.

2.1 Circulation calculation

To begin with, the circulation is calculated with a 3-D hydrodynamical and thermohaline submodel (Fig.2). The calculation domain is enclosed by three open boundaries A-A′, B-B′ and C-C′ as shown in Fig. 4. The grid size is variable; the finest one is 1.5 km in the north-south direction at Mizushima area (source area) and the coarsest one is 3.0 km in both east-west and north-south direction at the remote area. Basically five layers are set up in the vertical; 0-2m, 2-5m, 5-10m, 10-20m and 20-201m. The thickness of the lowermost layer varies according to the bottom depth.

Since the M_2 tide is dominant in the Seto-Inland Sea (Oceanogr. Soc., 1985), only the M_2 tide is considered for tidal forcing, and to be a representative of the semidiurnal tides, so that its period is taken to be 12 hours instead of 12.42 hours. The tidal amplitudes and phases are specified by a tidal harmonic constants table (Hydrographic Department, 1989) at A, A′, B, B′, C and C′. Amplitudes and phases along the lines A-A′, B-B′ and C-C′ are determined by interpolation.

The temperature and salinity at the open boundaries are specified with climatological data by past observations in winter (Oceanogr. Soc., 1985). The initial conditions of temperature and salinity for the interior of the domain are specified also with climatological data (Oceanogr. Soc., 1985). The surface salinity flux is neglected. The fresh water supply from rivers is given by monthly data in Dec. 1988 (Ministry of Construction, 1988a). For the surface heat flux, only the solar radiation and cloud cover are considered; latent and sensible heat fluxes, upward and downward long wave radiation are ignored. The temperature of the fluvial fresh water is specified with monthly data (Ministry of Construction, 1988b). The surface wind stress is neglected, so that the wind driven current is neglected.

The coefficient of horizontal eddy diffusion for momentum, heat and salinity is taken to be $50\,m^2/s$ based on field data of drifting card (NAKATA and HIRANO, 1978). The coefficient of vertical eddy diffusion for momentum, heat and salinity is constant horizontally but variable vertically with the Richardson number which is variable with vertical stability. Although the vertical stability is slightly time-dependent in the course of time integration, it is taken to be a constant in time; $0.3\times10^{-4}m^2/s$ at the surface

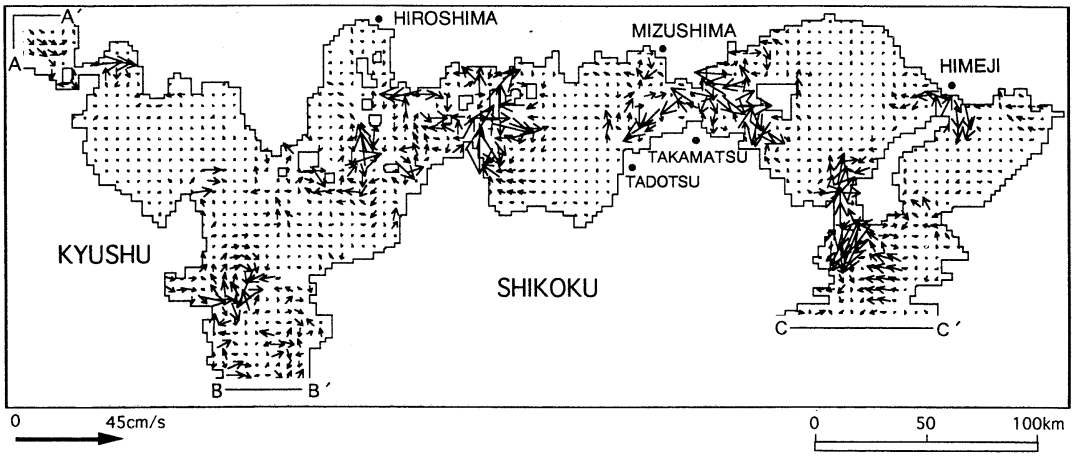

Fig. 4. Distribution of the simulated flow at the first layer. The arrow length is proportional to the speed.

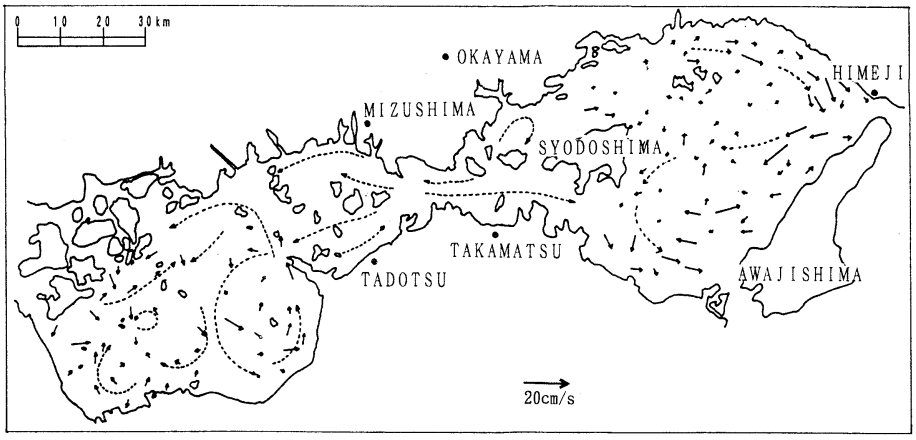

Fig. 5. Distribution of the observed flow at 10m depth. The arrow length is proportional to the speed. Dotted lines show the flow pattern schematically. (Oceanogr. Soc., 1985)

layer and $0.5\times10^{-4}m^2/s$ at the deeper layers. The equations for momentum, heat and salinity are integrated for 48 hours with a time step of 30 seconds. The boundary conditions mentioned above are kept constant in time, except for sea levels at the open boundaries.

The distribution of the calculated flow averaged over the last 12 hours is shown in Fig. 4, although a period of 48 hours is obviously too short for the thermohaline flow to reach a statistically almost steady state. Figure 5 schematically shows the flow pattern based on observed data (Oceanogr. Soc., 1985). Figures 4 and 5 are qualitatively similar to each other, though neither longer period tidal currents nor wind-driven currents are taken into account in the calculation. Off Mizushima, the calculated flow is eastward with 3cm/s, while no observed data are available. To the east of Shoudoshima Island the calculated velocity at the 1st layer is generally 1–10cm/s smaller than the observed one. The calculated velocity at the 2nd layer is almost the same as that at the 1st layer.

2.2 Estimation of dispersion

The grid structure is the same as that for the circulation calculation except for adding a very thin sheet over the sea surface. Oil in the surface sheet moves with the water in the first layer without slipping. The surface oil thickness

is not explicitly calculated, but only the oil amount in the surface sheet is a prognostic variable. The oil is assumed to be initially spilled into the surface sheet 2.25km×1.5km large on one grid box surface off Mizushima. The oil entrained from the surface into the underlying water column is dispersed by horizontal and vertical subsurface flows, diffusion, sinking and floating due to its density relative to surrounding water density.

The dispersion is calculated for 20 days starting on Dec. 18 for two cases; one is the case of no oil entrainment and the other with oil entrainment. In the former case, there is no adsorption, no sedimentation, either; there is no downward pathway from the surface.

A continuous source, constant in time for 6 hours, is set up off Mizushima. The total amount is 10000 t. The specific gravity of oil is 985kg/m^3, a typical value of C heavy oil. The coefficient of horizontal diffusion is taken to be 20 m^2/s, which is consistent with the field data cited above. The coefficient of vertical diffusion is taken to be 0.5×10^{-4}m^2/s in the surface sheet and 1×10^{-4}m^2/s at the 1st to lowermost layers. The time step is 600 seconds.

Daily mean wind velocity is calculated from data supplied every 3 hours from 18 weather stations around the Seto-Inland Sea (Fig.6a). These data are interpolated by using spline method in space at each grid point. Linear interpolation in time applies at each time step. So far the difference of the wind between at sea and on the land has been discussed (e.g., U.S. Army Coast. Eng. Res. Center, 1966). The offshore wind can reach up to 1.5 times as fast as the wind on land, but offshore increase of wind speed is ignored here. The wind is assumed to bring about an oil advection at a rate of 3% of its speed. Vector diagrams of the wind velocity are shown from Dec. 18, 1974 to Jan. 6, 1975 in Figs. 6b, c. At stations near Mizushima (e.g., Okayama, Takamatsu, and Tadotsu) the wind is dominantly eastward with a speed of about 3 m/s for these days, so that its effect on oil advection is greater than that of water flow with a speed of 3cm/s.

In the case of no oil entrainment, Fig. 7 shows the distribution of oil concentration (oil amount divided by a grid box area) in the surface sheet at 1 day, 6 days and 20 days after. Concentration of 100mg/m^2 is colored purple. Very thick oil reaches Awaji Island (90km apart from the source) 20 days after spill, showing an average eastward speed of 5cm/s. This speed is compatible with wind and current speed. The wind speed is much more important than the current speed in the surface dispersion. Figure 3 gives an eastward speed of about 23cm/s averaged over the first 4 days. The simulation gives 12cm/s averaged over the first 6 days (Fig. 7b), which is smaller than the observed speed by a factor of about 2.

Figure 8 shows the distribution in the surface sheet in the case of oil entrainment at 1 day, 6 days and 20 days after. There is no significant difference between Figs. 7a, b and 8a, b, which indicates the oil entrainment is negligibly small

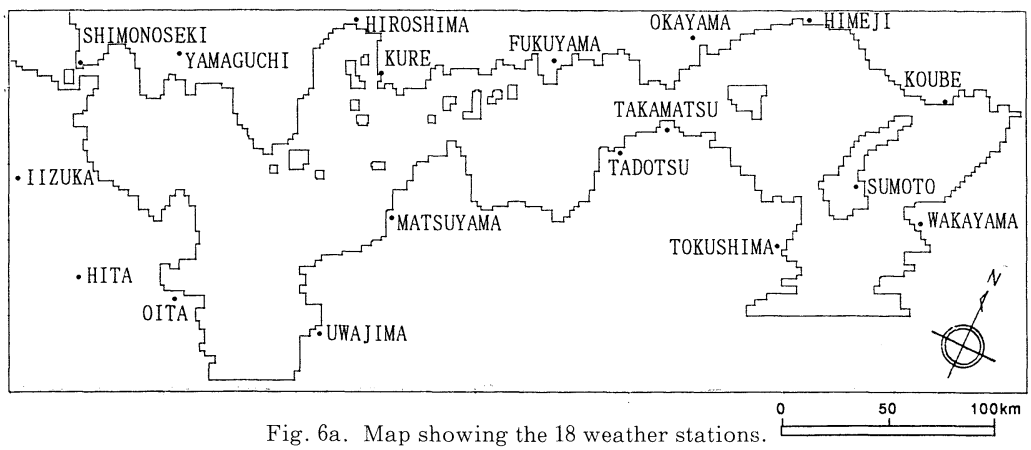

Fig. 6a. Map showing the 18 weather stations.

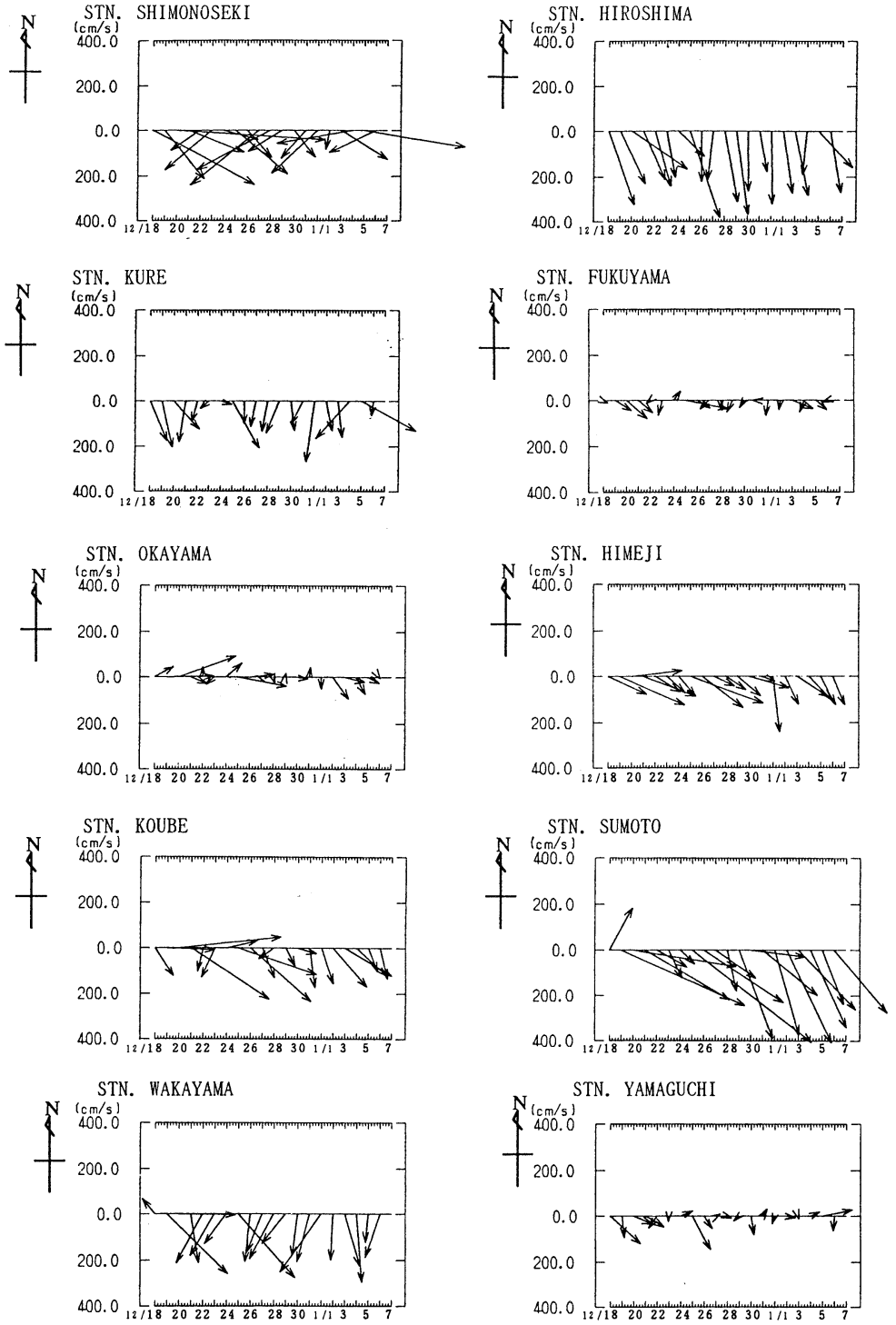

Fig. 6b. Vector diagrams of the wind velocity for Dec. 18, 1974 to Jan. 6, 1975 at 10 weather stations shown in Fig. 6a.

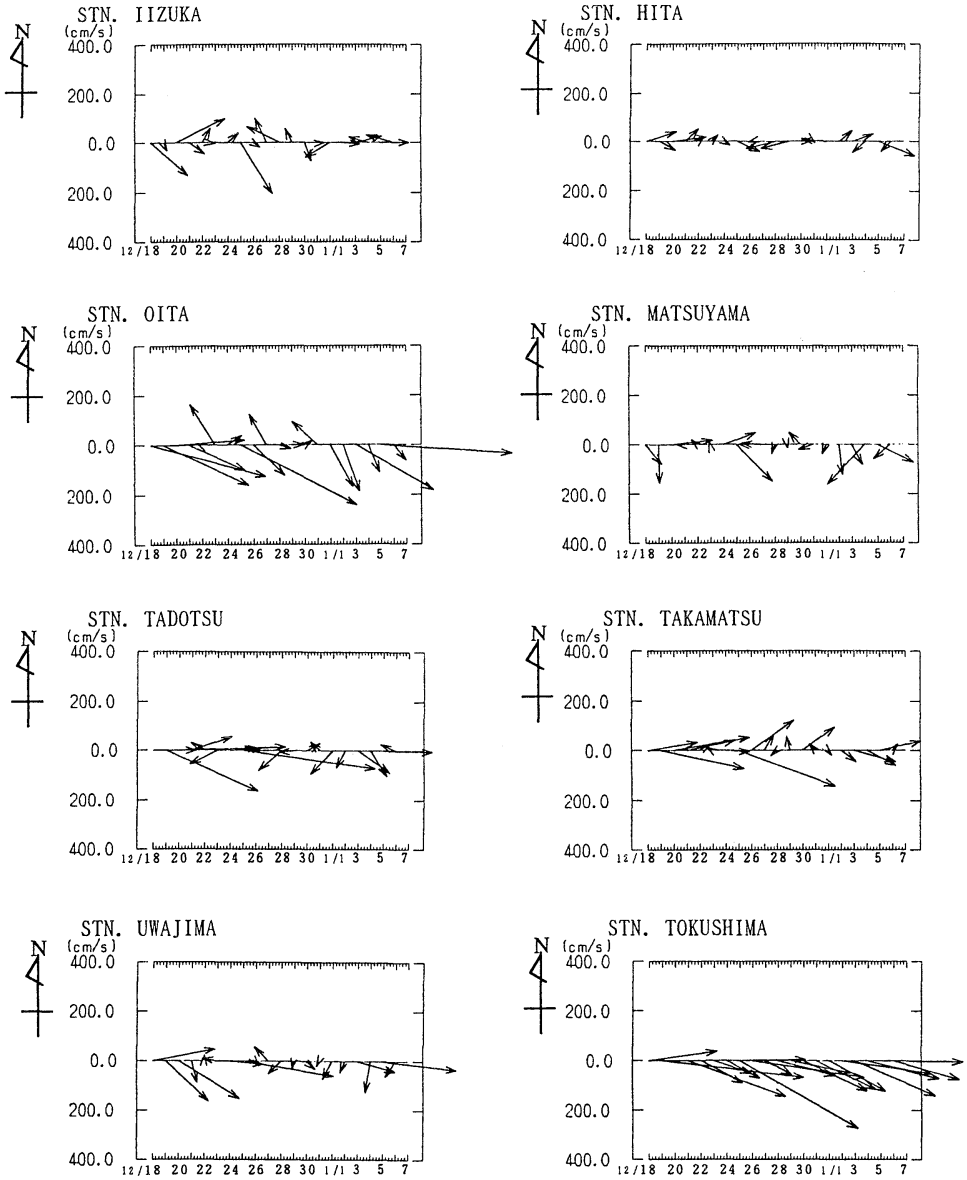

Fig. 6c. Same as Fig. 6b except for stations.

for the first 6 days. The difference is, however, striking between Figs. 7c and 8c 20 days after, probably because of the water content increase in oil droplet with time, which enhances entrainment into deeper layers through the oil density increase. While there is no significant difference in oil extent between days 6 and 20 in the case of entrainment (Figs. 8b, c), there is in the case of no entrainment (Figs. 7b, c); in other words, the expanding speed is very small between days 6 and 20 in the former case but still significant in the latter case because it remains a small amount of oil on the surface with entrainment, but a large amount of oil on the surface without entrainment.

The distribution of oil concentration at the 1st layer (0–2m depth) is shown in Figs. 9a, b, c. Comparison of Fig.8 with Fig.3 shows that the

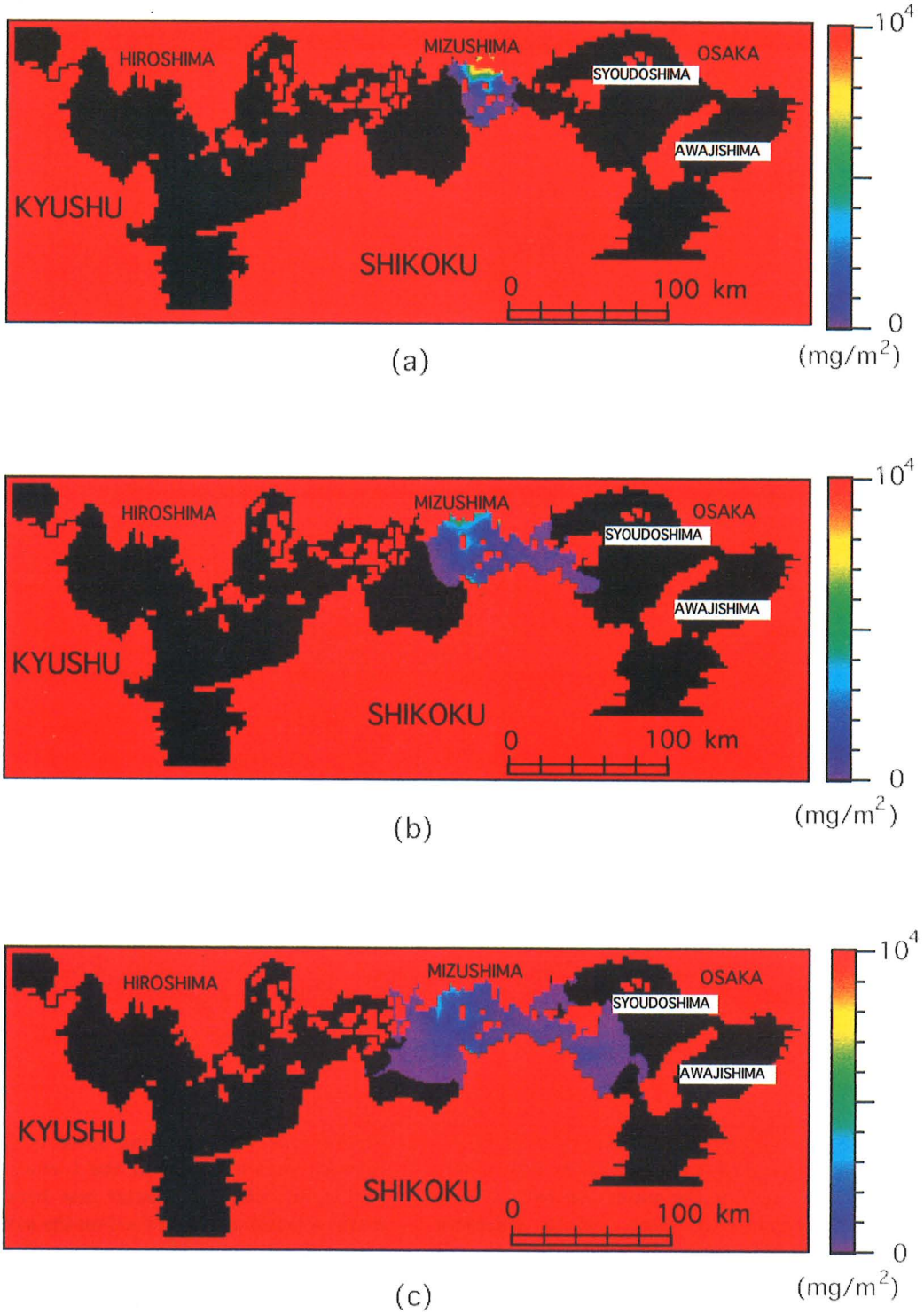

Fig. 7. Distribution of the oil concentration in the surface sheet. (a) one day, (b) 6 days and (c) 20 days after oil spill without oil entrainment.

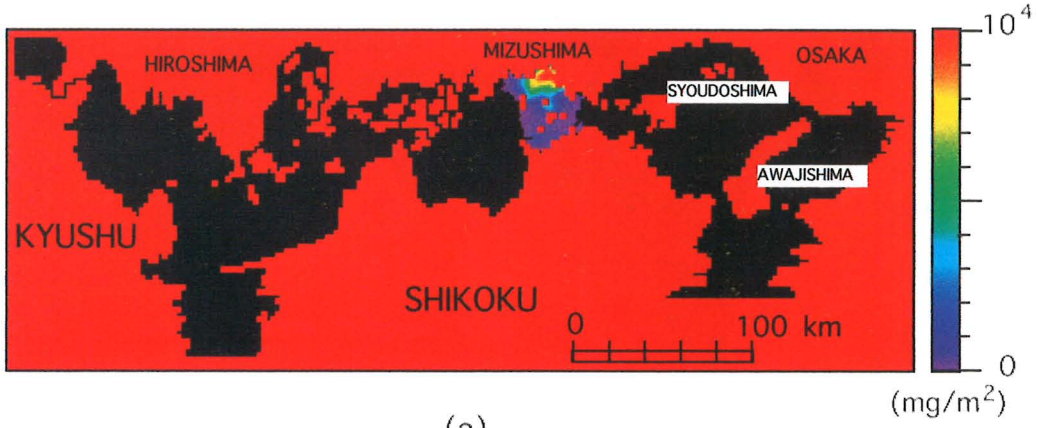

(a)

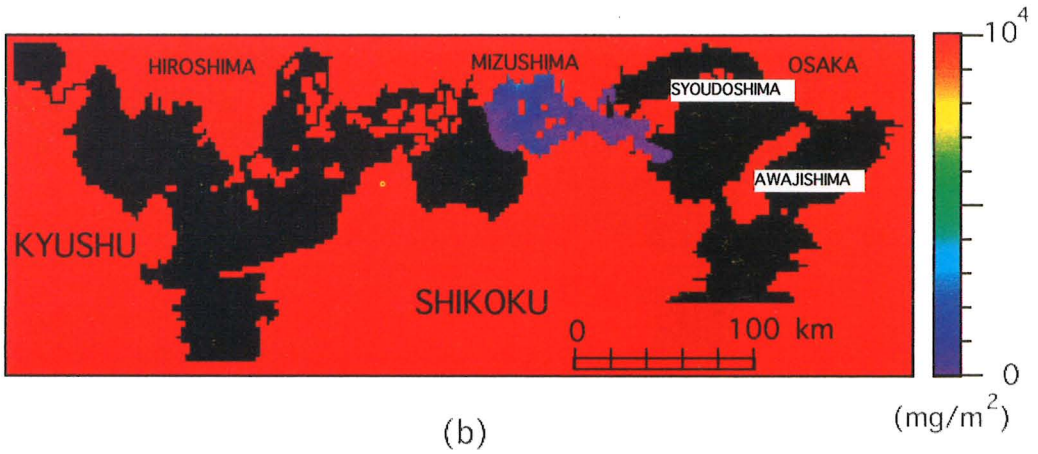

(b)

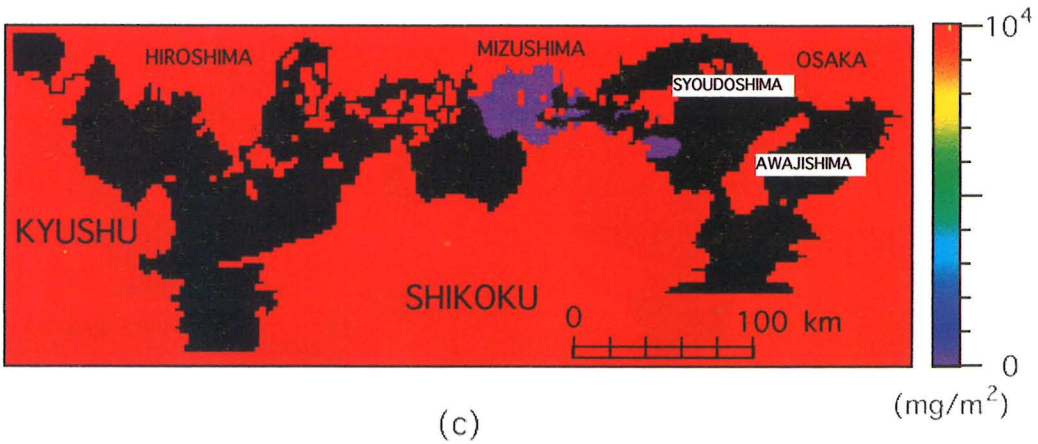

(c)

Fig. 8. Same as Fig. 7 except for the case of oil entrainment.

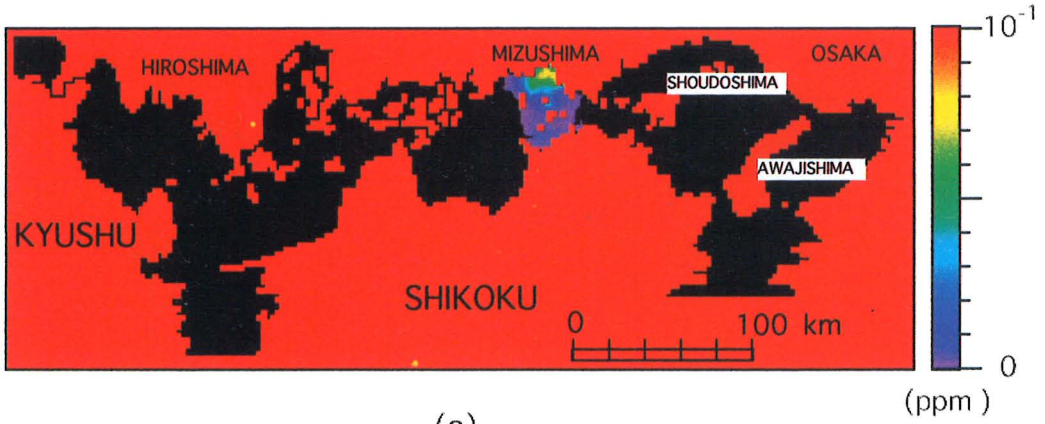

(a)

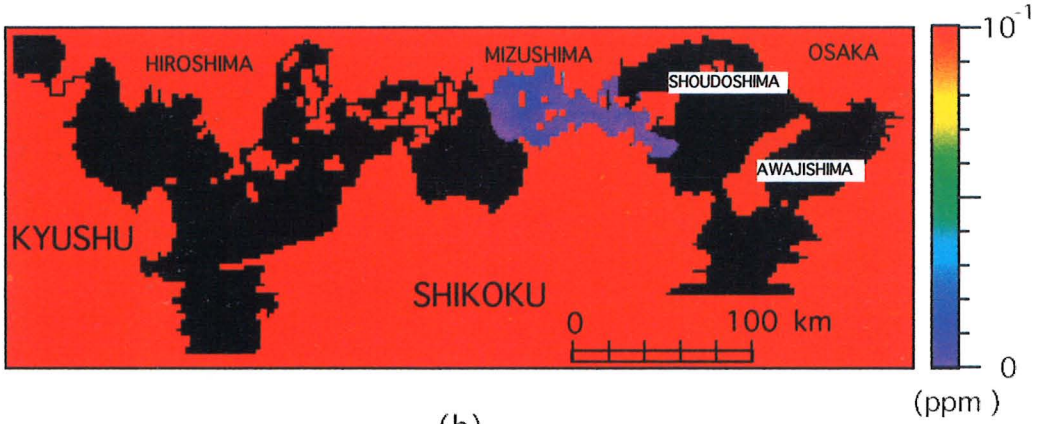

(b)

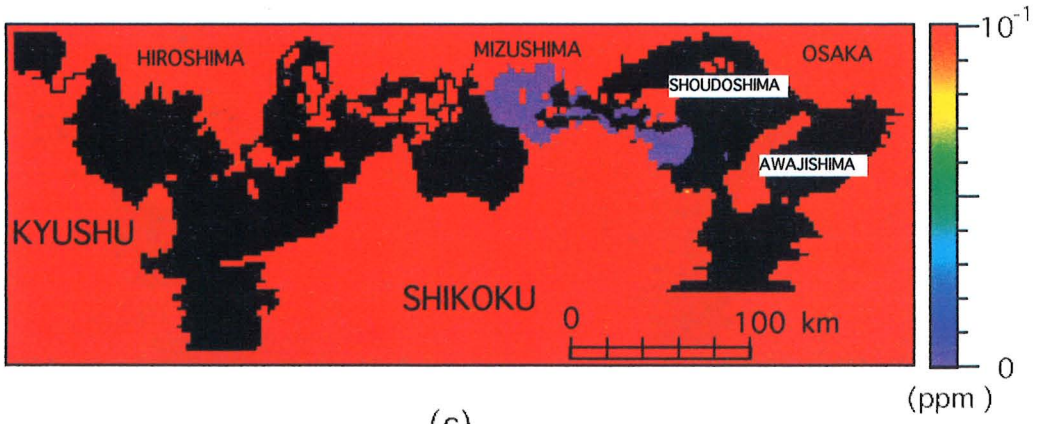

(c)

Fig. 9. Same as Fig. 8 except for the 1st layer.

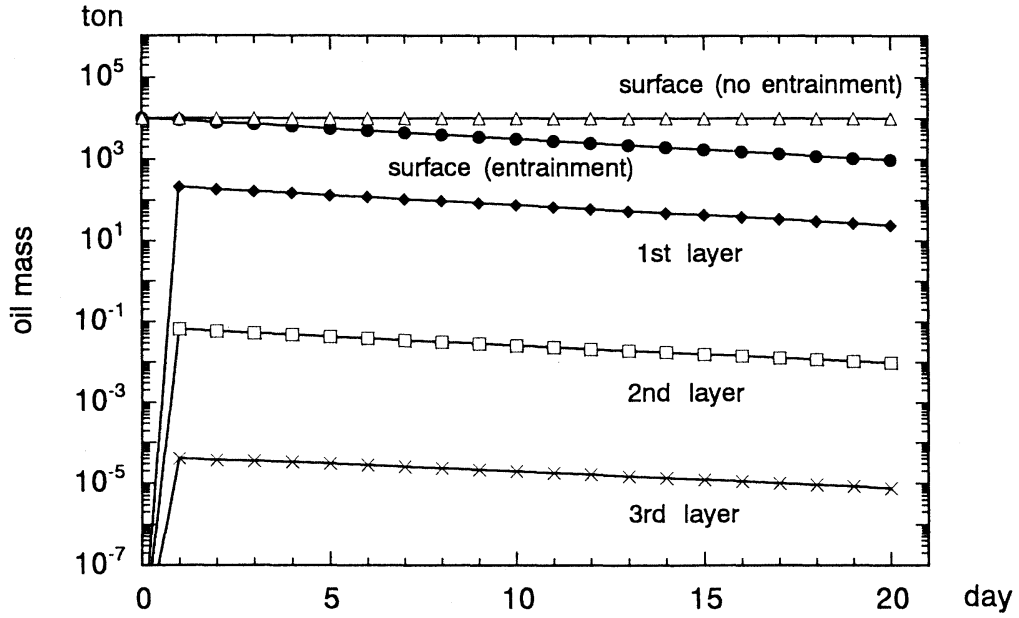

Fig. 10. Time variations of the oil amount in the surface sheet and the 1st to 3rd layers.

calculated extent of oil at the 6th day agrees fairly well with the observed one at the 4th day (22 Dec.). But the calculated extent is much wider to the west of Mizushima, probably due to the underestimated wind speed and wind drift factor. Results of previous studies on the drift factor range from 2.5% to 5.3% (REED, 1992). If it is specified as 5–6% instead of 3% with the wind speed used above, or if it is about 4% with the wind speed intensified above the sea surface by about 50%, the calculated extent will be wider to the east and narrower to the west than that calculated above, and agree better with the observed one. As to the westward dispersion, Fig. 3 gives 4.3 cm/s (mean distance 15km divided by 4 days) and the simulation gives 7.7 cm/s averaged over the first 6 days. If the wind factor is assumed to be 6%, the simulated speed will be about 3.8cm/s, which fairly agrees with the observed speed.

Time variations of the oil amount in the surface sheet with and without entrainment, and in the 1st to 3rd layers with entrainment are shown in Fig.10. The oil amount at the 4th, 5th layers and on the bottom are less than 10^{-5}t. At the end of time integration (day 20) in the case of entrainment, the oil amount is 1079t (10.8% of the initial amount) in the surface sheet and about 27t in the underlying layers. In the case of no entrainment, it is 9996t (99% of the initial amount) in the surface sheet. Most of oil in the surface sheet and in the underlying layers is decreased by weathering: evaporation and biodegradation in the surface sheet, and biodegradation in the underlying layers.

3. Concluding remarks

A 3-D oil dispersion model (SPILOR) is applied to the oil spill accident happened at Mizushima in Dec. 1974 in the two cases; with and without oil entrainment.

The striking difference between the results in the two cases emphasizes importance of the oil entrainment in predicting the oil extent for time scales longer than several days.

The simulated extent agrees fairly well with observation, but improvements are needed to correctly imbed the processes of concern in the model. For the present, the model validation is not easy because very few data are available on the concentration and property change of spilled oil. Only a limited amount of data are available from laboratory experiments. In the meantime, more numerical experiments are useful for understanding how sensitive the model is to various processes and parameters such as the wind drift factor, weathering, entrainment, emulsion formation. In addition, the oil

thickness should be explicitly dealt with as a prognostic variable, and the biodegradation should be properly modeled, though it is treated together with evaporation in the present study. While these problems are approached with numerical and/or laboratory experiments, carefully designed field experiments are crucial for the model validation and improvement.

References

Environment Agency (1975): Oil spill accident at Mizushima: pollution survey. Rept. No.6, Environ. Agency, Tokyo. (in Japanese)

FAY, J. A. (1971): Physical processes in the spread of oil on a water surface. Proc. Joint Conf. on the Prevention and Control of Oil Spills, API, 463–467.

HORIGUCHI, F., K. NAKATA, T. KOJIMA, S. KANAMAKI and S. SUGIOKA (1991): Fate of oil spill in the Persian Gulf. Pollution Control, **26** (4), 39–62. (in Japanese)

Hydrographic Department (1989): Tidal harmonic constants table. 42–78. Hydrogr. Dept., Tokyo.

JOIA (Japan Ocean Development Industry Association) (1988): Technical report on the environmental impact assessment associated with oil development in the sea. JOIA, Tokyo, 310pp. (in Japanese)

MACKAY, D. and C. D. MCAULIFFE (1988): Fate of hydrocarbons discharged at sea. Oil & Chemical Pollution, **5**, 1–20.

MACKAY, D., I. BUIST, R. MASCARENHAS and S. PATERSON (1979): Experimental studies of dispersion and emulsion formation from oil slicks. Workshop on phys. behavior of oil in the mar. environ. Princeton Univ., National Weather Service, Silver Spring, Maryland, **1**, 17–40.

MACKAY, D., S. PATERSON, P. D. BOEHM and P. L. FIEST (1981): Physical-chemical weathering of petroleum hydrocarbons from the Ixtoc I blowout. Chemical measurements and a weathering model. Proc. 1981 Oil Spill Conf., 453–460.

Ministry of Construction (1988a): Annual report of fluvial discharge. Japan River Association, Tokyo. (in Japanese)

Ministry of Construction (1988b): Annual report of water quality. Kanto Kensetu Kouseikai Publ., Tokyo. (in Japanese)

NAKATA, H. and T. HIRANO (1978): On the dispersion and convergence of properties in straits and approaches. Bull. Coast. Oceanogr., **16**, 31–42.

Oceanographical Society of Japan (1985): Coastal Oceanography of Japanese Islands. 694–698. Tokai Univ. Press, Tokyo. (in Japanese)

REED, M. (1992): Modeling of physical and chemical process governing fate of spilled oil. ASCE Workshop on oil spill modeling, Charleston, South Carolina, 26pp.

SHEN, H. T., P. D. YAPA, D. S. WANG, and X. Q. YANG (1991): A mathematical model for oil slick transport and mixing in rivers. Dept. Civil and Environ. Eng., Clarkson Univ., Rept. 91–1, 118pp.

U.S. Army Coastal Engineering Research Center (1966): Shore protection, planning and design. Tech. Rept. No.4.

YANAGI, T. and Y. OKAMOTO (1984): A numerical simulation of oil spreading on the sea surface. La mer, **22**, 137–146.

La mer 32: 307–324, 1994
Société franco-japonaise d'océanographie, Tokyo

Preliminary evaluation of a Gulf of Mexico circulation model at 92°W

Christopher N. K. MOOERS*, San JIN* and Dong-Shan KO*

Abstract: As part of the U. S. Minerals Management Service (MMS) Gulf of Mexico Modeling Program, the efforts to assess preliminarily the skill of an exploratory application of the BLUMBERG-MELLOR (1983) model to the Gulf of Mexico by OEY and ZHANG (1993) are described. Three years of model output are analyzed and compared to current meter records, typically of one-year duration, along 92°W, allowing demonstration of some of the skill assessment methodology. The model was driven with ocean climatology on its open boundaries, climatological mean winter atmospheric forcing, and climatological mean river runoff from the Mississippi and Atchafalaya Rivers. The salient results of the preliminariy assessment are

—the model output and observed data have comparable mean and rms amplitudes, and generally similar space-time structure
—the model output indicates a strong eastward jet at the shelfbreak, which is also the locus of high variability, requiring further observational confirmation
—the eddy passages apparently impact substantially the shelfbreak region
—the shelfbreak region, due to its concentration of mean flow and variability (and presumably shelf-Gulf of Mexico exchange), must be accounted for in designing model and observational domains and grids for the LATEX (Louisiana-Texas shelf) region.

1. Introduction

As numerical circulation models for marginal and semi-enclosed seas are under rapid development, it is important to begin to evaluate them thoroughly relative to observations. Realizing that there are parallels to be drawn between the circulation of the Gulf of Mexico and the circulation of the East Asian Seas, especially the Sea of Japan, this paper illustrates a contemporary effort in the USA to evaluate a numerical circulation model relative to observations in the Gulf of Mexico. Hopefully, future works in evaluating numerical circulation models for the East Asian Seas will be stimulated by the present paper, and will lead to comparisons with Gulf of Mexico circulation models.

A preliminary skill assessment of a Gulf of Mexico circulation model is made by comparing model output to observations from a moored current meter array deployed over the continental shelf and slope along 92°W. (This assessment is preliminary in the sense that soon a more advanced version of the model from Dynalysis of Princeton, and more complete observations from the Louisiana-Texas Shelf Physical Oceanography Program (LATEX) field program will be available for skill assessment.) The objectives are (1) to seek a preliminary validation of the model, (2) to examine model design issues associated with shelfbreak variability and exchange processes, and (3) to demonstrate several skill assessment methodologies.

The Gulf of Mexico circulation model utilized is the BLUMBERG-MELLOR (often known as the Princeton Ocean Model) sigma coordinate, primitive equation model (BLUMBERG and MELLOR, 1983) implemented on a ca. 20km rectangular grid (and with 21 sigma levels) by OEY and ZHANG (1993). The model was initialized with hydrographic climatology (LEVITUS, 1982), and it was driven by climatological mean winter wind forcing (HELLERMAN and ROSENSTEIN, 1983), climatological mean winter surface heat and evaporative fluxes (from Surface

* Ocean Prediction Experimental Laboratory, Rosenstiel School of Marine and Atmospheric Science, University of Miami, 4600 Rickenbacker Causeway, Miami, Florida 33149-1098, U.S.A.

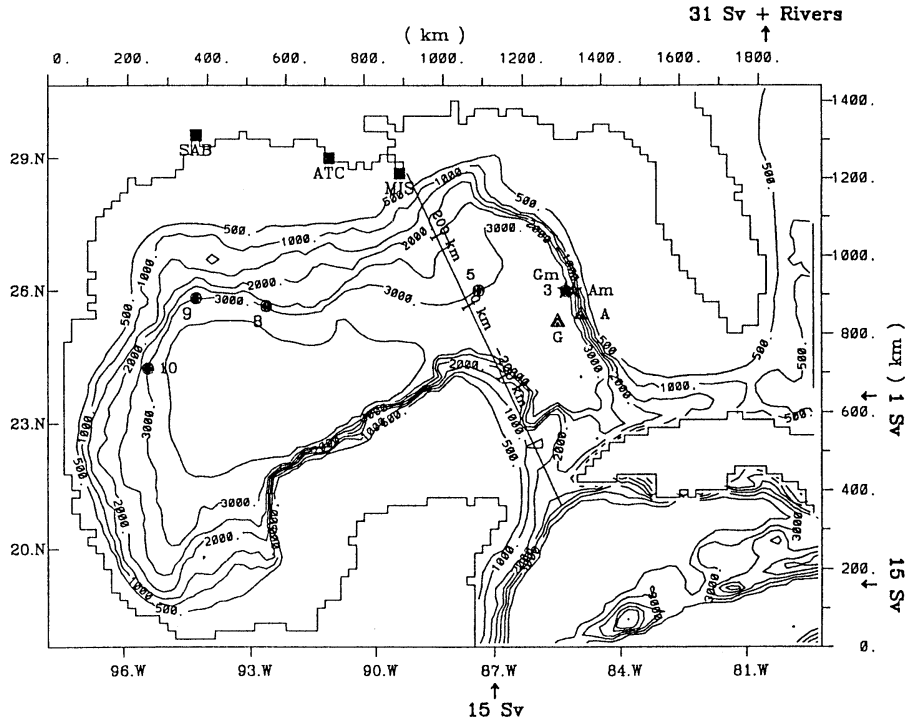

Fig. 1. Gulf of Mexico model domain. Isobaths are in meters; squares indicate river discharge points: MIS – Mississippi, ATC–Atchafalaya, SAB–Sabine.

Marine Observations data set, National Climate Data Center) and mean river runoff (based on stream gauge data from the U.S.Army Corps of Engineers, W. WISEMAN, Louisiana State Univ., personal communications); the model was also relaxed to climatological winter surface temperature and salinity (LEVITUS, 1982); see OEY and ZHANG (1993) for more details. Thus, neither tidal nor synoptic (or seasonal) wind and thermohaline forcing were applied to the model. Three years of five-day averaged model output data were analyzed from year four-to-seven of the model simulation, i.e., after the model had spun-up (based on the realistic broadband frequency of Loop Current eddy-shedding exhibited by the model). Since the forcing was not time-specific, only statistical comparisons between model and observations can be performed, i.e., phase comparisons are meaningless.

The moored current meter array had been deployed along 92°W from 1987 through 1989 by Science Applications Incorporated (SAIC) (sponsored by the Mineral Managements Service). (Analyses of some of these and additional data have been provided by HAMILTON (1990, 1992).) There were 29 current meters mounted on seven moorings. The sampling rate was half-hourly. The maximum common record length of credible data for several current meters was about one year. The focus in this paper is on one current meter mooring (upper-slope station) located near the shelfbreak; data from the outer-shelf station are introduced where essential.

Hence, the model output lacked the realism afforded by synoptic or seasonal atmospheric, seasonal runoff, and tidal forcing. Furthermore, the current meter data were limited in horizontal and vertical resolution, record durations, and temporal continuity. One consequence is that no seasonality can be inferred in the comparisons and interpretations, only gross comparisons and interpretations. A more fine-grained analysis will become possible when more realistic forcing is applied to the more advanced model, and when more comprehensive observational data sets are available. However, the

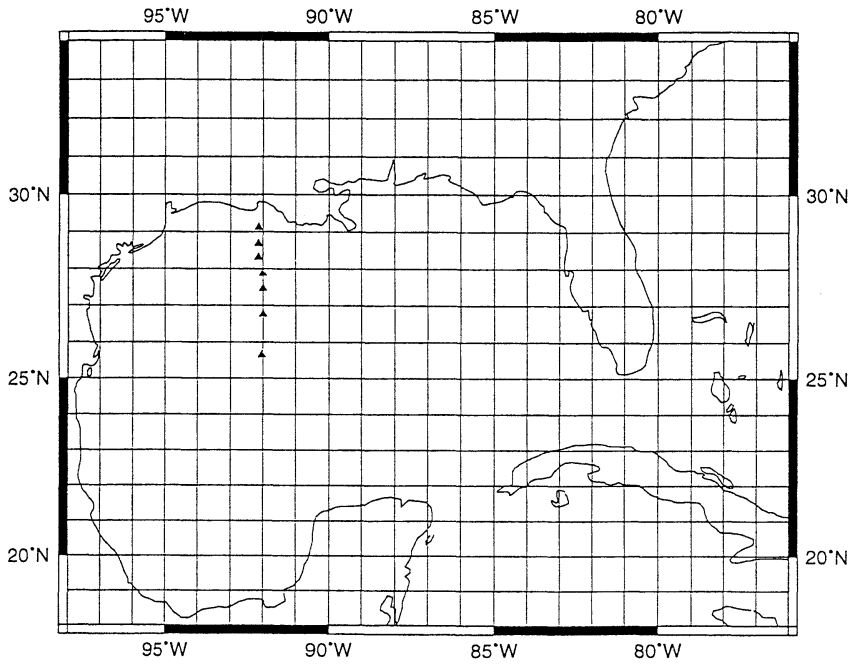

Fig. 2. Location of current meter mooring along 92°W. Triangles indicate moorings.

model was sufficiently realistic, and the observed data were sufficiently complete, to enable a worthwhile preliminary skill assessment of the model. In turn, this preliminary skill assessment allows demonstrating some of the skill assessment methodology developed under the Gulf of Mexico Modeling Program.

2. Background

This preliminary skill assessment has been performed, in part, to assess the results of OEY and ZHANG (1993), and, in part, to develop, test, and demonstrate some of the methods useful in model evaluation. The focus here is on the use of kinematical and statistical comparisons. Due to data availability, the emphasis is placed on time series comparisons at a specific location, vertical section analyses, and cross-shore transect analyses. There is an entire additional class of analyses to be applied to horizontal (2–D) data sets and 3–D data sets that will be possible when LATEX data become available.

Model and observational configurations. The model domain covers the Gulf of Mexico, Straits of Florida, and the northwest Caribbean Sea (Fig.1). The bottom topography is a smoothed version of DBDB5 (National Geophysical Data Center, 1986) and includes the continental shelves and quite realistic representations of major topographic features. The moored current meter array along 92°W (Fig. 2) extends from nearshore to the central Gulf.

The model is driven by the constant wind, heat, and runoff forcing mentioned above, plus specified (constant) inflows (a total of 30 Sv based on the Levitus climatology) along the southern and eastern boundaries in the Caribbean Sea, so that the model can organize its own Yucatan Current, which is not necessarily steady in time, and 1 Sv through the Bahama Islands. The model develops a Loop Current which aperiodically sheds anticyclonic eddies (Fig. 3; from OEY and ZHANG, 1993). These eddies subsequently propagate to the western Gulf and impinge upon the continental margin off Texas and Mexico (Fig. 4; from OEY and ZHANG, 1993). The mean eddy propagation path of eight model eddies falls within the envelope of observed (by satellite IR imagery from VUKOVICH at SAIC) decadal-mean trajectories (not shown). This qualitative agreement suggests that it would be

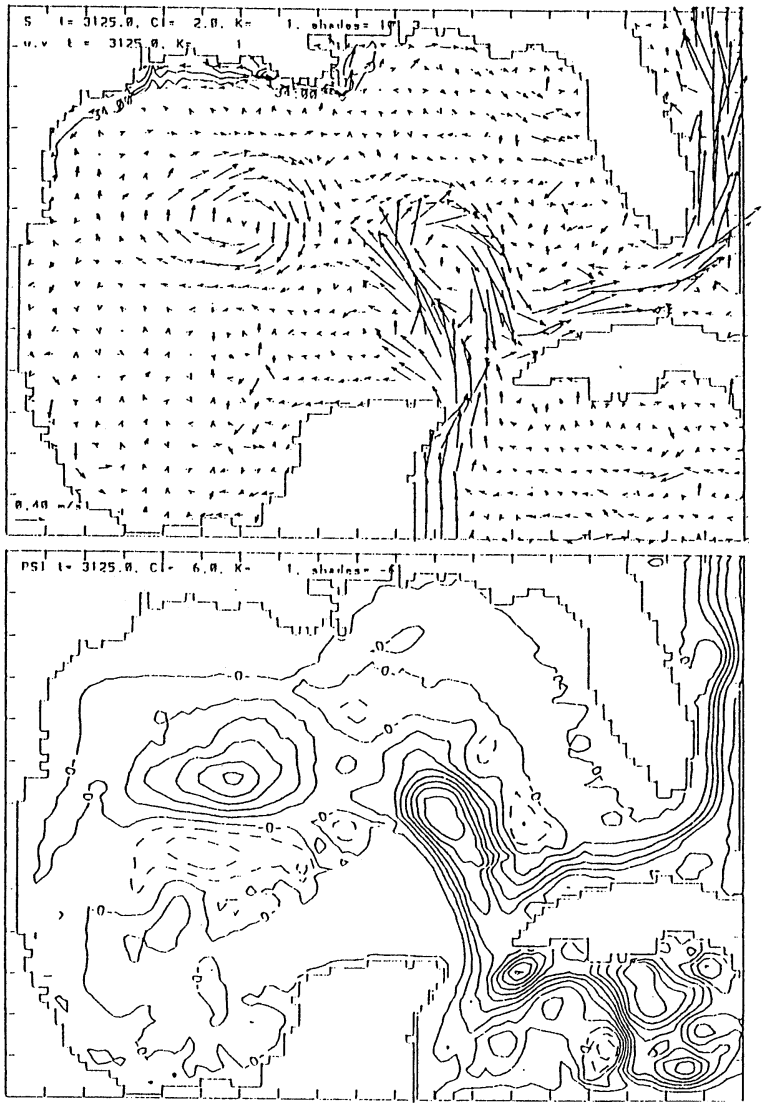

Fig. 3. Model output (OEY and ZHANG, 1993). Upper: synoptic surface currents at model day 3152, lower: corresponding synoptic total stream function (contour interval: 6 Sverdrups).

worthwhile to examine further the level of realism in the model output.

The model's sigma coordinate and rectangular grid system (Fig. 5) is intended to provide horizontal and vertical resolution adequate to describe the Loop Current, its eddy-shedding, and the eddy propagation and decay in the open Gulf. It is also intended to provide vertical resolution adequate to resolve wind-driven and buoyancy-driven transient circulation over the continental shelf and slope. The design of the moored current meter array had similar objectives over the continental margin. In particular, the moored array had three elements between the mid-shelf and upper-slope (Fig. 5), spanning a distance of ca. 100 km. Each of these moorings had typically three-to-four current meters on any one deployment.

For the purposes of this preliminary assessment, the analysis will focus on one station near the shelfbreak: the upper-slope station at 27.88°N in a water depth of 210m. For compari-

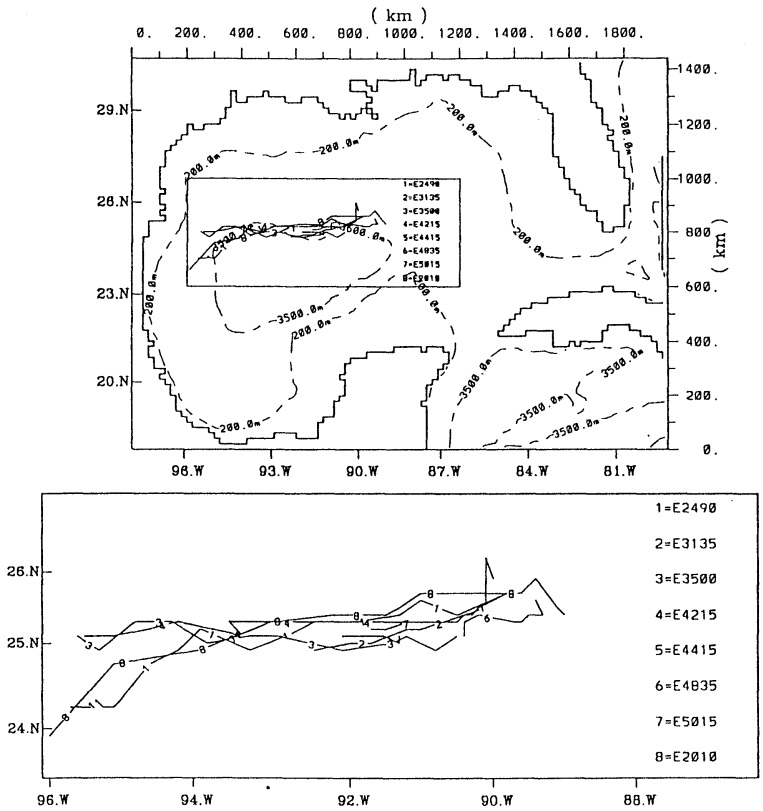

Fig. 4. Loop Current spin-off anticyclonic eddy trajectories. Upper: eight model eddy trajectories (solid lines), lower: the eight model eddy trajectories at expanded scale.

son with the observations, model output was chosen at the grid point whose water depth was closest to that of the observational station water depth. In particular, the upper-slope station is compared to model output at the grid point at 27.89°N in a water depth of 217m.

The time-continuity of the observational data is somewhat problematic. For example, at the upper-slope station (Fig. 6), there were records (with small gaps) at the upper levels for the majority of 1987 and 1988, while there was nearly a two-year record at the mid-levels, but the record length was less than a year at the lower level.

3. Overview of model output along 92°W

To demonstrate the character, structure, and spatial scales of variability in the model output, the mean and standard deviation fields are examined along 92°W (Fig. 7). Ideally, there would be sufficient observational data to evaluate these fields comprehensively. However, that is not the case, yet these model output fields provide a perspective for the preliminary assessment.

The zonal (along-shore) flow (Fig. 7a) is dominated by a mean eastward jet (with speeds up to 30 cms^{-1}) located over the shelfbreak (between ca. 50 and 1200m isobaths) and confined to the upper 800m. There is a maximum (up to 6 cms^{-1}) in the rms zonal velocity co-located with the shelfbreak jet. A secondary feature is the pair of mean inner-shelf (water depth of 15 to 30m), nearsurface (upper 10m) westward jets (up to 20 cms^{-1}). The mean westward flow nearshore is consistent with the buoyant coastal jets anticipated from the discharges of the Mississippi and Atchafalaya Rivers. The mean eastward flow over the shelfbreak region is qualitatively consistent with the return flow inferred from hydrography by COCHRANE and KELLY (1986).

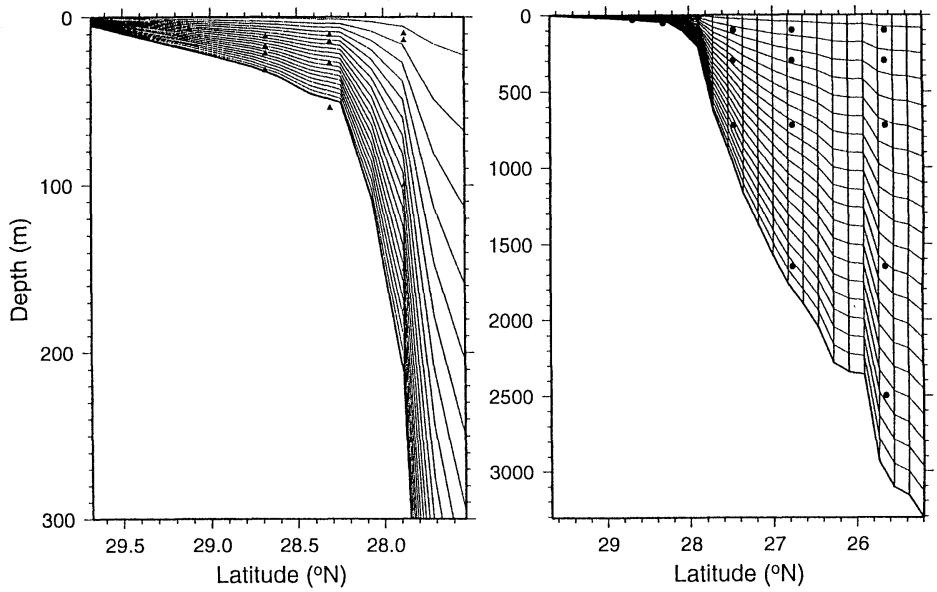

Fig. 5. Model grid and current meter positions along 92°W. Left: expanded shelf domain; right: full coastal ocean domain. Solid triangles and circles indicate current meter locations.

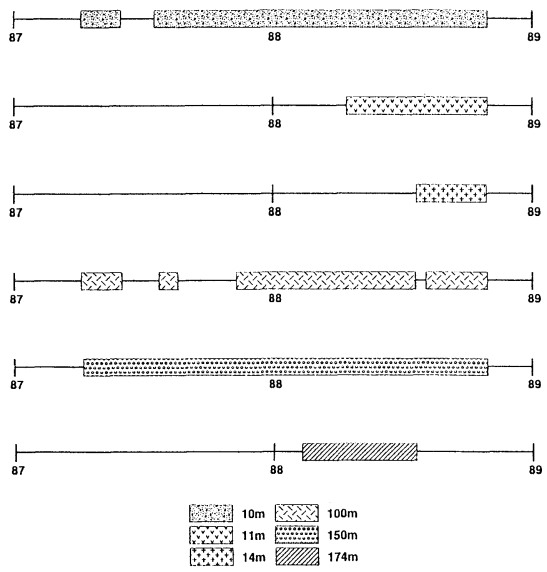

Fig. 6. Time-line of current meter data along 92°W. Upper-slope station (27.9°N; 210m water depth)

Over the inner-shelf, the meridional (cross-shore) flow (Fig. 7b) is dominated by mean nearsurface onshore flow and nearbottom onshore flow, which are consistent (in an Ekman sense) with the applied westward wind stress and predominant nearbottom eastward flow, respectively. A secondary feature consists of a subsurface divergent mean flow (ca. ± 2 cms^{-1}) over a domain of 100km zonally by 1,000m vertically over the continental slope. The rms meridional velocity has maxima (ca. 3 cms^{-1}) over the outer-shelf, upper-slope, and in the upper 500m at 300 km from the shelfbreak.

The vertical velocity (Fig. 7c) is dominated by mean strong, alternating upwelling and downwelling cells in the lower half of the water column over the lower and upper continental slope, seemingly in association with steep topography. The rms vertical velocity field follows closely the general pattern of the rms meridional velocity field. The vertical velocity field is a prime example of a field which is difficult to observe and independently validate, and, hence, if the model can be otherwise validated, this model field would be valuable for many purposes; e.g., ocean dynamical, water quality, and marine ecosystems studies.

The mean temperature field (Fig. 7d) is dominated by the permanent thermocline and baroclinicity over the continental slope. A secondary feature is the inner-shelf frontal zone (cool water nearshore). The rms temperature field has maxima (ca. 1.2°C) nearbottom over

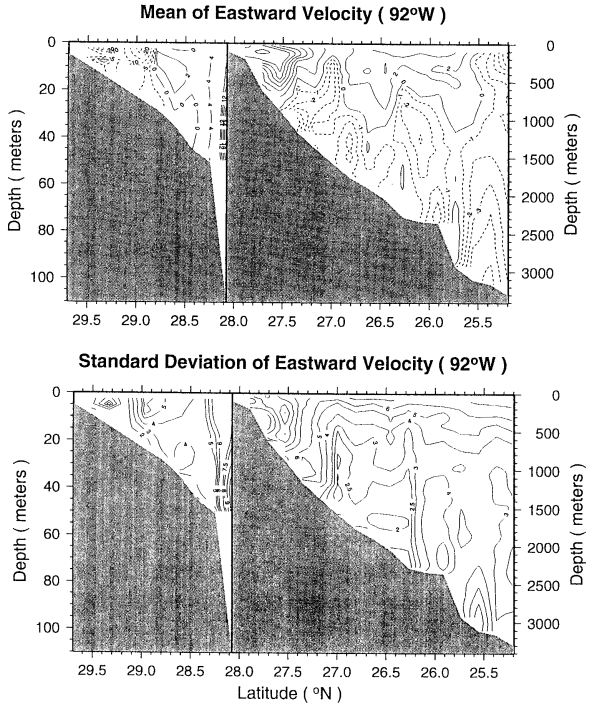

(a) Zonal velocity (u) (positive east; cms^{-1})

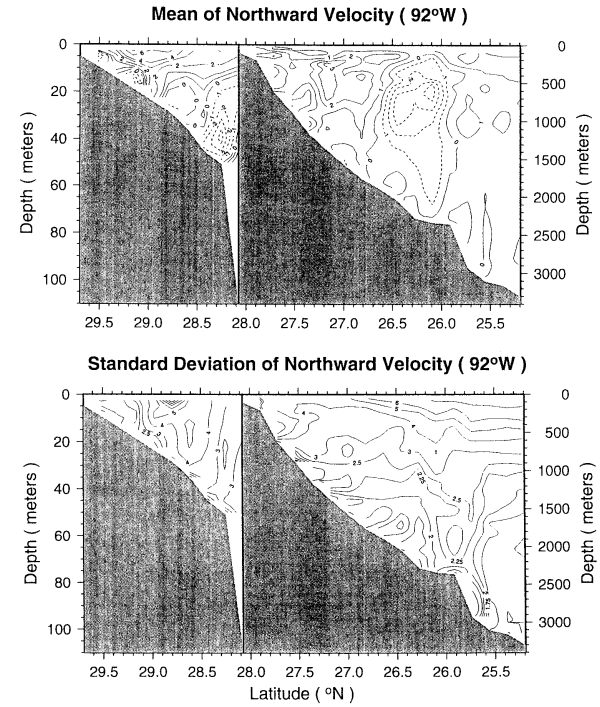

(b) Meridional velocity (v) (positive north; cms^{-1})

Fig. 7. 92°W mean and rms transects for model output. Left: expanded shelf domain; right: full coastal ocean domain.

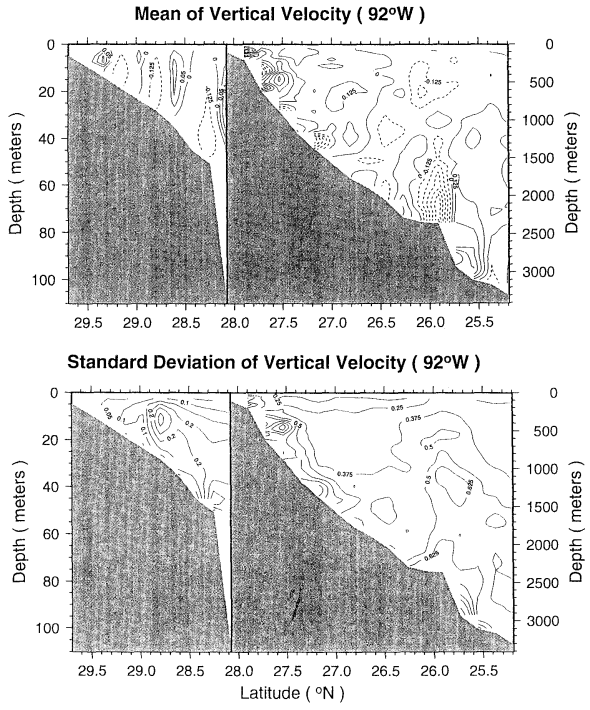

(c) Vertical velocity (w) (positive up; cms^{-1})

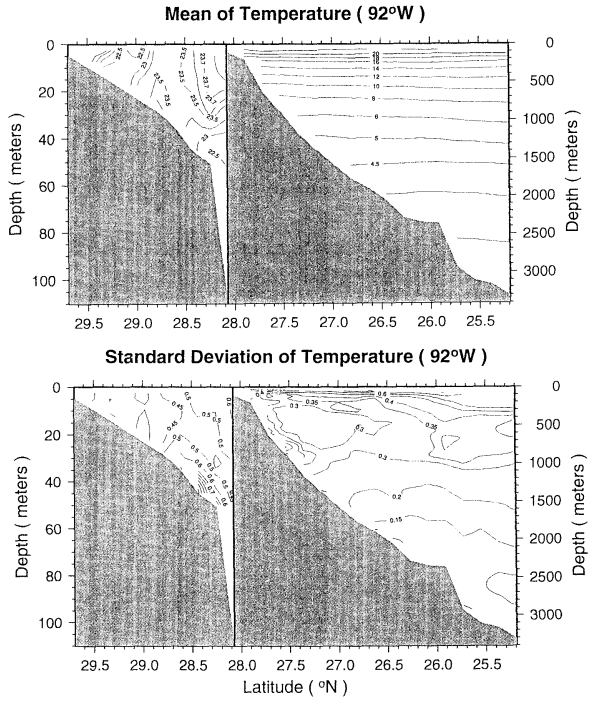

(d) Temperature (T; ˚C)

Fig. 7. 92˚W mean and rms transects for model output. Left: expanded shelf domain; right: full coastal ocean domain.

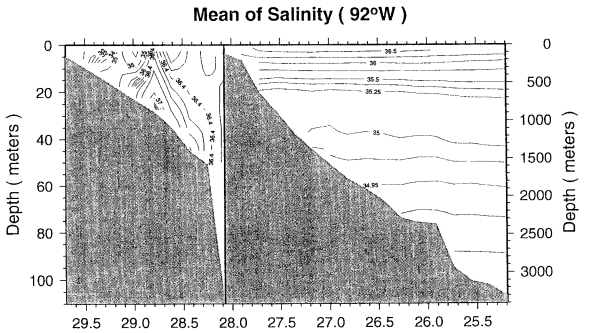

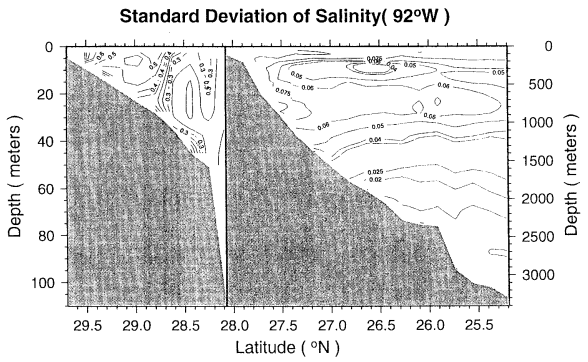

(e) Salinity (ppt)

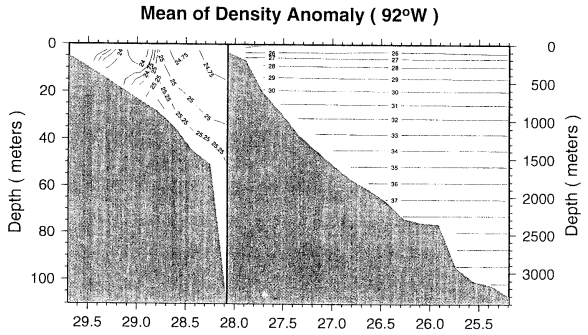

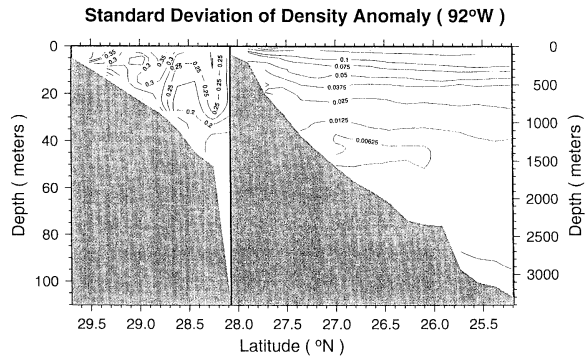

(f) Density (σ_t)

Fig. 7. 92°W mean and rms transects for model output. Left: expanded shelf domain; right: full coastal ocean domain.

the outer-shelf, consistent with transient bottom Ekman flow, and nearsurface (upper 200m) over the continental slope (on the scale of 200km), consistent with eddy passages. The mean salinity field (Fig. 7e) is dominated by a permanent halocline and relatively fresh nearsurface cores over the inner-shelf. The rms salinity field has maxima over the inner-shelf. The mean density field (Fig. 7f) is dominated by the permanent pycnocline, baroclinicity over the slope, and two nearsurface, inner-shelf buoyant cores. The nearshore mean structure of the temperature, salinity and density fields is consistent with the presence of the buoyant coastal jets derived from the Mississippi and Atchafalaya Rivers. The corresponding nearshore rms maxima suggest these jets are highly variable.

Overall, the mean and rms fields appear plausible given what is known of the general circulation in this region; e. g., westward flow along the inner-shelf and return flow over the outer-shelf and slope (COCHRANE and KELLY, 1986). Since the model is driven by mean and not synoptic wintertime atmospheric forcing, it is unable to provide vertical homogenization of the mass field characteristic of the shelf regime during winter (NOWLIN and PARKER, 1974). A most prominent feature is the eastward jet at the shelfbreak which needs independent confirmation and validation. In particular, based on the material presented here, it is unclear whether the jet is attributable to the wind-driven circulation, buoyancy-driven circulation, eddy-induced Reynolds stresses, or the model artifact due to steep topography. With the result from the full ten-year run, OEY and ZHANG (1993) found that the jet was not permanent and was, thus, attributable to eddy passages during the three-year period treated here.

4. Model output-observation data comparisons near the shelfbreak

Comparisons are made of time series, vertical profiles, and spectra at the upper-slope station. The raw half-hourly observations were filtered with a half-power frequency of 5.8 cpd to remove high-frequency internal waves and observational noise, and subsampled to three-hourly values for autospectrum analyses (Fig.12). The three-hourly subsampled observations were then filtered with a half-power frequency of 0.14 cpd to remove tidal and inertial motions, and subsampled to five-day values (to be commensurate with the model output) for time series plots, vertical profile means, standard deviations, and choerence analyses (Fig. 13).

Time domain comparisons. Time series of the zonal (along-shore) velocity (Fig. 8a), meridional (cross-shore) velocity (Fig. 8b), and temperature (Fig. 8c) for three levels at the upper-slope station indicate, most fundamentally, that the current meter and model output data have a common range of values. Since the time axis for the model output has no absolute meaning relative to the time axis of observations (due to the steady forcing applied to the model), the origin of the model output time axis has been adjusted to maximize the overall visual correlation of the zonal and meridional velocities. The major events seen in each are associated with anticyclonic eddy passages, as determined independently from the analysis of surface topography and current maps. The time series of the surface velocity at 92° W versus latitude (Fig. 9) demonstrates eddy passages, as well as the continuous (though variable) nearshore westward jets and the intermittent eastward jet near the shelfbreak. The model output from days 1560 to 2755 is analyzed statistically. The model output from days 1910 to 2645 in Fig. 9 (0 to 735 in Fig. 8) is compared in time series plots with observations, and the eddy passages centered on days 2210 and 2510 are important features in these comparisons; they correspond to eddies 8 and 1, respectively (Fig. 4). From independent studies of satellite AVHRR imagery and in situ observations, two Loop Current anticyclonic eddies were shed during the period of moored current meter data availability in April to October 1987 and April to May 1988 (Tom BERGER, SAIC, personal communications). Hence, the large observed perturbations in zonal velocity during October 1987 and May 1988 (Fig. 8a) possibly correspond to the passage of these eddies.

The amplitudes (ca. 10 to 20 $cm\,s^{-1}$) of the eddy-related perturbations are similar in the observations and model output, as is the interval (ca. 300 days) between eddy passages. In both

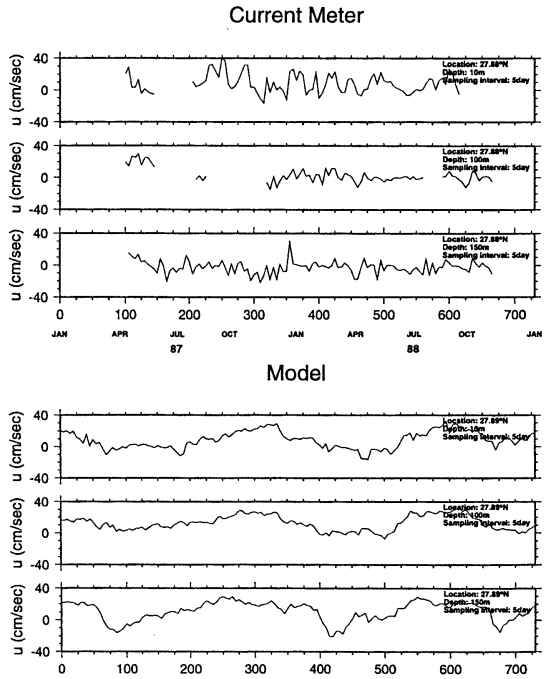

(a) Zonal velocity (u; cm s^{-1}). Upper-slope station (27.9°N; 210m water depth).

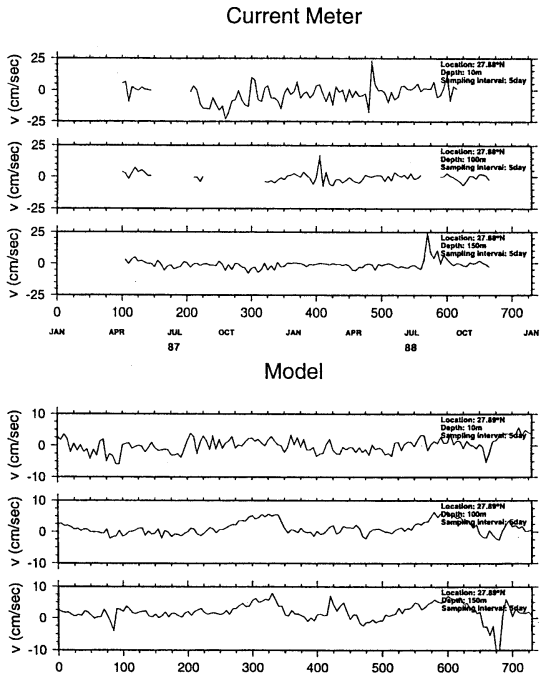

(b) Meridional velocity (v; cm s^{-1}). Upper-slope station (27.9°N; 210m water depth).

Fig. 8. Time series of model output and observed data. Focus is on manifestations of eddy passages at days 300 and 600 near 28°N.

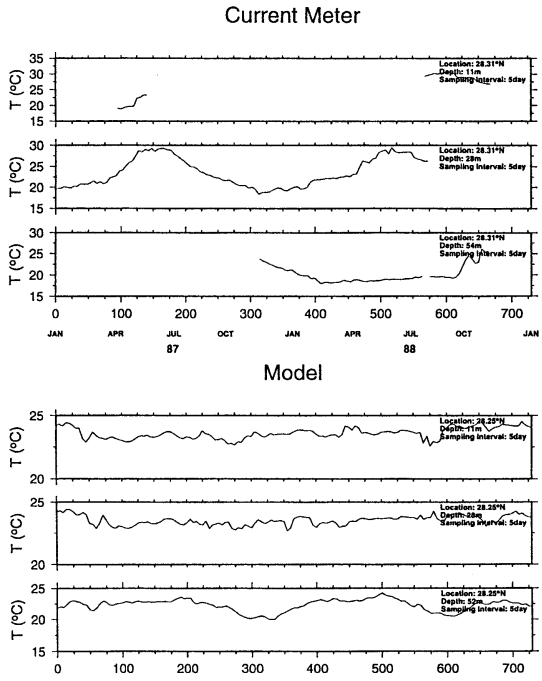

(c) Temperature (T; °C). Upper-slope station (27.9°N; 210m water depth).

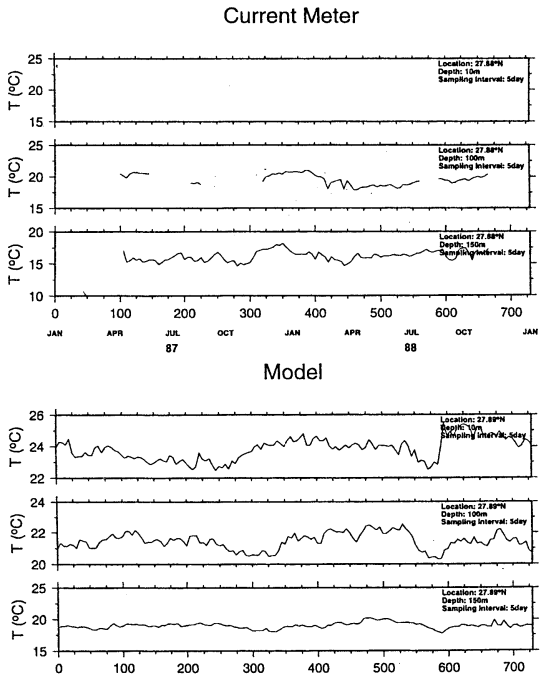

(d) Temperature (T; °C). Outer-shelf station (28.3°N; 60m water depth).

Fig. 8. Time series of model output and observed data. Focus is on manifestations of eddy passages at days 300 and 600 near 28°N.

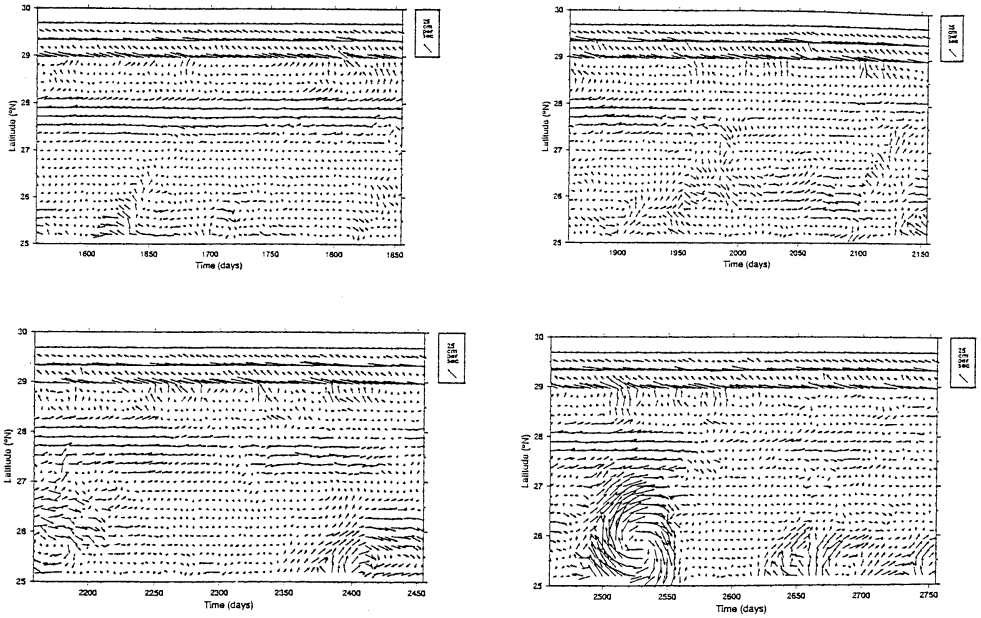

Fig. 9. Time series of model output surface velocity at 92°W versus latitude. Focus is on manifestations of eddy passages at days 2210 and 2510 near 28°N.

the observations and the model output, the large (20 cm s^{-1}) eddy-perturbation zonal velocities are eastward and are confined to the upper water column while the nearbottom perturbations at the outer-shelf station (not shown here) are only a few cm s^{-1}. Not surprisingly, the meridional perturbations are weaker and more variable.

At the upper-slope station (Fig. 8c), there are temperature perturbations of a few degrees associated with eddy passages in the model output. In contrast, the mid-depth temperature observations at the outer-shelf station (Fig. 8d) are dominated by an annual cycle, which, of course, is absent in the model output. There is not an obvious manifestation of the eddy passages in the upper layer temperature of the model output, probably because the eddies barely penetrate to the shelfbreak. However, there is a nearbottom temperature decrease (ca. 2°C) with each eddy passage, probably due to the onshore bottom Ekman transport of cooler water from over the slope.

Vertical profile comparisons. The mean vertical profiles (together with standard deviation bars) calculated from one year of observations and three years of model output are compared (Fig. 10) at the upper-slope station. The mean observed profile is a few cm s^{-1} eastward in the upper half of the water column, but the mean model profile is 10 to 20 cm s^{-1} eastward. The mean profiles of observed and model meridional velocity are similarly weak (1 to 2 cm s^{-1}), but opposite in sign at two of the three observed depths. The mean vertical velocity is upwards in the upper 50 m, downwards between 50 and 125 m, and upwards from 125 to 220 m. The mean model temperature profile is nearly linear with depth, is 4°C cooler than the mean observed temperature nearsurface, and is 2 to 3°C warmer at mid-depths. The model reached a ststistical steady-state by the end of year four, and the next three years of model output have been analyzed here. Hence, these discrepancies in the temperature profiles may reflect flaws in the climatology with which the model was initialized and the artificial thermal forcing applied to the model. (The density profiles are not discussed because they follow from the temperature and salinity profiles.)

The vertical profiles of Reynolds stress for observed and model output data are compared (Fig. 11) at the upper-slope station. The ob-

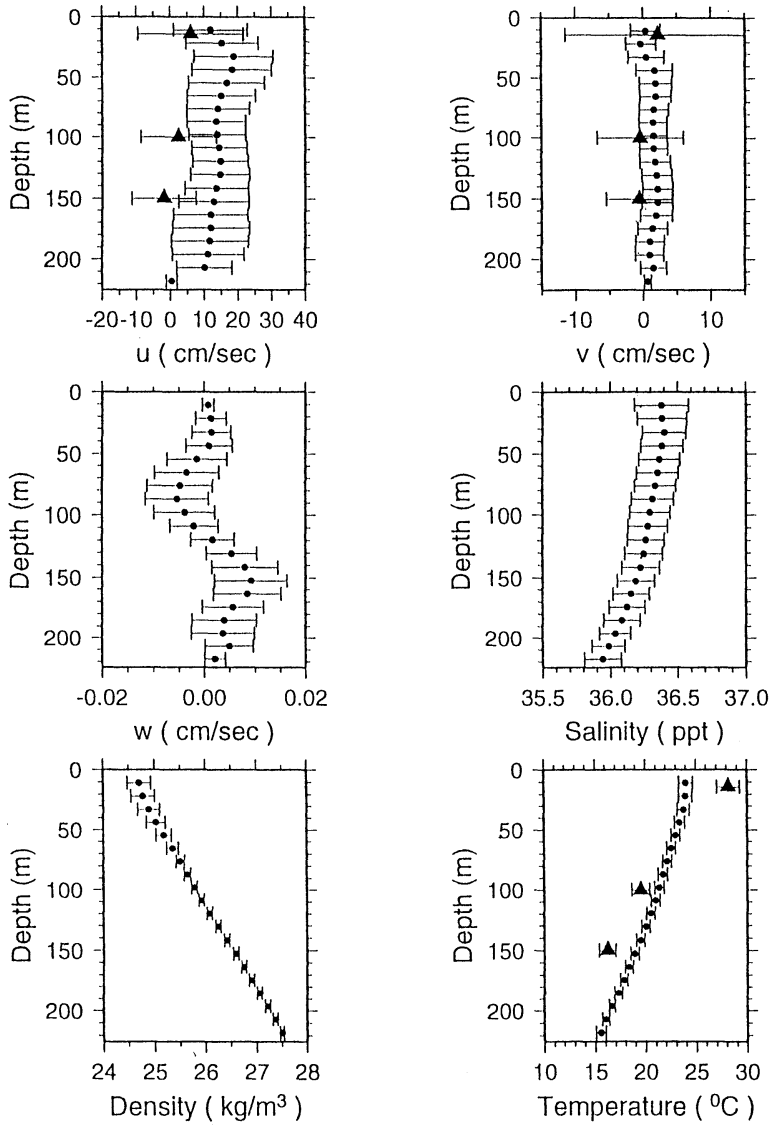

Fig. 10. Mean vertical profiles of model output (solid dots) and observed data (solid triangles) and plus/minus standard deviation bars. Upper-slope station (27.9°N; 210m water depth) (density in σ_t).

served and model values for ⟨u'u'⟩, ⟨v'v'⟩, and ⟨u'v'⟩ agree in order of magnitude. The u', etc. notation is applied to deviations from the record mean.). In contrast, the observed values are generally much greater than the model values for ⟨T'T'⟩, probably due to annual cycle fluctuations in the observations. (Note: temperature was not successfully observed at the upper current meters; thus, these values are missing for ⟨T'T'⟩, etc.) Observed and model values for ⟨u'u'⟩ have double maxima, and for ⟨v'v'⟩ they are generally near zero, except nearsurface for the observed value. Some of the discrepancies in Reynolds stresses may be due to the lack of synoptic atmospheric forcing (especially the manifestations of wintertime cold front passages) applied to the model.

Overall, the mean profiles are generally similar in magnitude and structure, though the eastward jet is much stronger in the model output

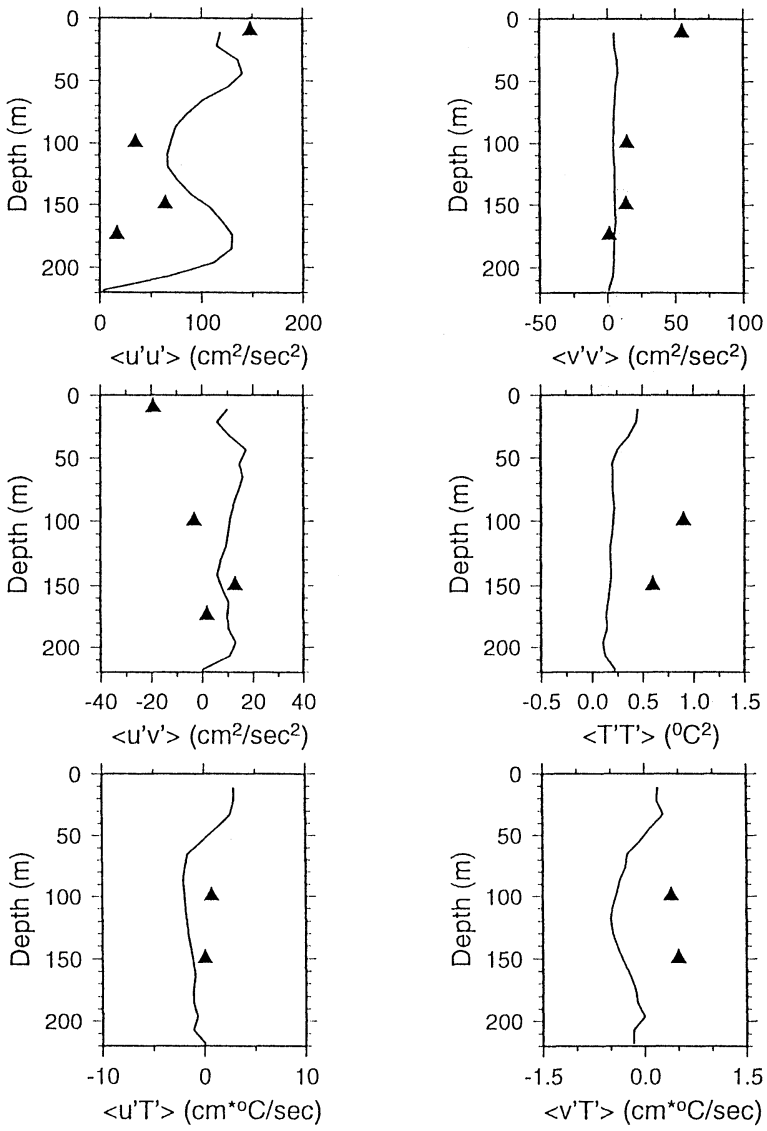

Fig. 11. Mean vertical profiles for Reynolds stress of model output (solid lines) and observed data (solid triangles). Upper-slope station (27.9°N; 210m water depth).

than in the observations. Also, there is a large variation in mean profiles between the outer-shelf (not shown) and upper-slope stations, a distance of ca. 40km, indicative of the need for higher spatial resolution in observations. Similarly, there is more vertical structure in the mean model flow profiles than the vertically sparse observations can define.

Spectrum analysis comparisons. The energy spectra for the model output (solid dots) and observed data (solid triangles), zonal and meridional velocity components are compared (Fig. 12). The Nyquist sampling frequency for the observed data is 1 cycle per hour, while for the model output it is 1 cycle per 10 days. As described earlier, the observed data were filtered and subsampled to a Nyquist sampling frequency of 4 cycles per day for autospectrum analyses (Fig.12); they were further filtered

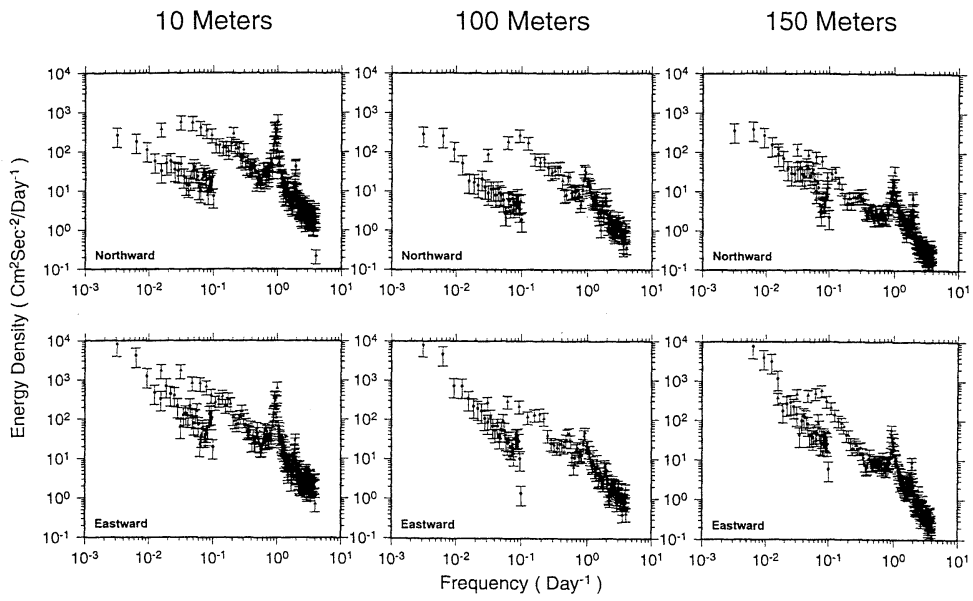

Fig. 12. Energy density spectra of model output (solid dots) and observed velocity data (solid triangles) and plus/minus standard deviation bars. Upper: meridional component; lower: zonal component; at upper-slope station (27.9°N; 210m water depth).

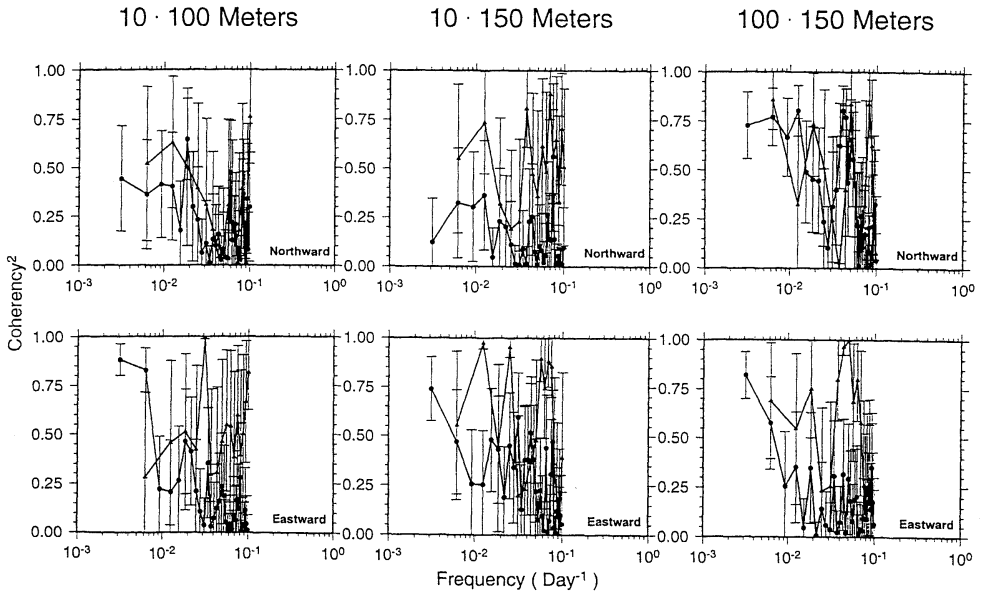

Fig. 13. Vertical coherence of model output (solid dots) and observed velocity data (solid triangles) and plus/minus standard deviation bars. Upper: meridional component; lower: zonal component; at upper-slope station (27.9°N; 210m water depth).

and subsampled to a Nyquist sampling frequency of 0.1 cycles per day for coherence analyses (Fig. 13). The lowest frequency resolved is 1 cycle per 100 days for the observed data and 1 cycle per 300 days for the model output. Standard deviation bars are shown for the ensemble-averaged spectra. As a consequence of the different sampling rates and record lengths,

the observed and model spectra only overlap in a spectral band between 0.02 and 0.1 cpd.

At the upper-slope station, there is an order of magnitude difference in energy levels at 10 and 100m, and even in the eastward component at 150m, in the 0.02 to 0.1 cpd spectral band. (Presumably, there may be better agreement when the model is forced with synoptic winds.) Overall, the energy level of the model output changes less with depth than does the energy level of the observed data. The spectra of observed data are a reminder that considerable energy exists at the diurnal-inertial (especially in the upper 10m), and some at the semidiurnal time scale which is not yet treated by the model. Similarly, there is considerable energy in the several-day band in the observed data which, if it existed in the model output, has been averaged out in the archival process. However, the energy in this band is likely generated by wind variations which the model could not reproduce at this stage due to the constant wind forcing.

The vertical coherence for the model output (solid dots) and of the observed data (solid triangles), zonal and meridional velocity components are compared (Fig.13). At the upper-slope station, the vertical coherence of the model output and observed data are, with a few exceptions, in qualitative agreement. For example, the vertical coherence generally decreases from time scales of 100 days to 30 days, but with a tendency for the observed values to rise near 10 to 20 days, probably reflecting the response to synoptic atmospheric forcing.

Overall, the observed spectra and vertical coherence results suggest that model results must account for the vigorous inertial and tidal motions over the Louisiana/Texas shelf, especially considering their probable importance to turbulent mixing.

5. Summary and conclusions

The Gulf of Mexico circulation model has means and variances which are commensurate with those of the observations on 92°W. However, there are important differences in detail. For example, the upper layer variance in the synoptic (spectral) band (3- to-10 days periods) is an order of magnitude less in the model output than in the observations. As another, the vertical coherence of the observed data considerably exceeds that of the model output in the 10- to -20 days band. The differences are probably mainly due to the model being forced by constant rather than synoptic winds.

Major features of the model output include two westward nearshore, nearsurface buoyant jets; an eastward shelfbreak, full-water-column zonal jet; and high variability at the shelfbreak, including that due to eddy passages. Strong patterns exist in model output fields over the continental slope, presumably due to eddy passages. Mean and variance fields from the model have coherent patterns on scales of 50 km horizontally and 50 m vertically. However, available observations lack sufficient resolution to validate such patterns.

The present results must be updated with results from improved model runs from the Gulf of Mexico Modeling Program, especially those runs with seasonal and synoptic atmospheric forcing, plus tidal forcing. They also need to be updated when more comprehensive observations become available from the LATEX field program. It will be important to archive at least portions of the model output at daily (or even hourly) intervals. The skill assessment methodology needs to be extended to include horizontal coherence, 3-D analyses, and diagnostics for dynamics and energetics.

Acknowledgements

This research is sponsored by the Minerals Management Service as part of the Gulf of Mexico Modeling Program under subcontract from Dynalysis of Princeton. It is also supported by the Ocean Pollution Research Center of the University of Miami under a bequest from the Brenauer Estate. Comments on a draft manuscript by Drs. Leo OEY, Rich PATCHEN, Fred VUKOVICH and Bill WISEMAN are highly appreciated.

References

BLUMBERG, A. F. and G. L. MELLOR (1983): Diagnostic and prognostic numerical circulation studies of the South Atlantic Bight. J. Geophys. Res., 88, 4579-4592.

COCHRANE, J. D. and F. J. KELLY (1986): Low frequency circulation on the Texas-Louisiana

continental shelf. J. Geophys. Res., **91**, 10645–10659.

HAMILTON, P. (1990): Deep currents in the Gulf of Mexico. J. Phys. Oceanogr., **20**, 1087–1104.

HAMILTON, P. (1992): Lower continental slope cyclonic eddies in the central Gulf of Mexico. J. Geophys. Res., **97**, 2185–2200.

HELLERMAN, S. and M. ROSENSTEIN (1983): Normal monthly wind stress over the world ocean with error estimates. J. Phys. Oceanogr., **13**, 1093–1104.

LEVITUS, S. (1982): Climatological atlas of the world ocean. NOAA Professional Pap. 13, NOAA, Rockville, Maryland, 173 pp.

National Geophysical Data Center (1986): World-wide gridded bathymetry–DBDB 5. Boulder, Colorado.

NOWLIN, W. D. and A. PARKER (1974): Effects of a cold-air outbreak on shelf water of the Gulf of Mexico, J. Phys. Oceanogr., **4**, 467–486.

OEY, L. -Y. and Y. -H. ZHANG (1993): Loop Current and eddies: model sensitivity experiments and analyses. Ocean Modeling Group Technical Report No. 15, Stevens Institute Tech., 37pp., 30 figs.

Minutes of the Steering Committee and Plenary Meeting

I. Steering Committee

May 13, 1993 at 6:30 pm in Qingdao, China.

Chaired by K. TAKANO and attended by B.H. CHOI, K.L. FAN, Y. HSUEH, K. KIM, S. MIZUNO, Y. YUAN and F. ZHANG.

The Steering Committee reached following resolutions.

(1) Decide to arrange the publication of the Proceedings of the JECSS-PAMS VII Workshiop in La mer. K. KIM and K. TAKANO are responsible for editing and publication of the proceddings. Dr. ZHANG agrees to pay US $1,600 to La mer as part of expenses. Prof. TAKANO reported that the best solution to cover the expense is for authors to become members of the French-Japanese Society of Oceanography.

(2) Accept the invitation from Prof. YANAGI of Ehime University to hold the eighth workshop at Matsuyama, Japan in 1995. The Steering Committee expressed its thanks to Prof. YANAGI and Prof. TAKANO for the invitation. Changes in organization of the workshop in future are adopted as follows:

a. Abstracts of papers are received in advance and selected for oral presentation after review.

b. Poster sessions are arranged, if necessary.

c. A 4-day workshop is organized instead of a 6-day workshop.

(3) Members of the Steering Committee for 1993-1995 are nominated as follows:

Kuh KIM (Seoul National University, Korea), chairman
Byung-Ho CHOI (Sung Kyun Kwan University, Korea)
Ya HSUEH (Florida State University, USA)
Gil JACINTO (University of the Philippines, the Philippines)
Kazuo KAWATATE (Kyushu University, Japan)
Hsien-Wen LI (National Taiwan Ocean University, China)
Absornsuda SIRIPONG (Chulanongkorn University, Thailand)
Gennady YURASOV (Pacific Oceanological Insititute, Russia)
Fagao ZHANG (Institute of Oceanology, Academia Sinica, China)

II. Plenary Meeting

May 14, 1993 at 4:30 pm in Qingdao, China.

Chaired by K. TAKANO and K. KIM,

Accepted the resolutions adopted by the Steering Committee on May 13, 1993.

La mer 32: 327–332, 1994
Société franco-japonaise d'océanographie, Tokyo

JECCS-PAMS VII Workshop

May 9–14, 1993
Qingdao, China

Organization

Steering Committee

Kenzo TAKANO (University of Tsukuba), Chairman
Kuang-Lung FAN (National Taiwan University)
Ya HSUEH (Florida State University)
Kazuo KAWATATE (Kyushu University)
Kuh KIM (Seoul National University)
Gil JACINTO (University of the Philippines)
Absornsuda SIRIPONG (Chulalongkorn University)
Gennady I. YURASOV (Pacific Oceanological Institute)
Fagao ZHANG (Institute of Oceanology, Academia Sinica)
Takashi ICHIYE (Texas A & M University), Honorary Chairman

Local Organizing Committee

Yunshan QIN (Institute of Oceanology, Academia Sinica), Chairman
Dunxin HU (Institute of Oceanology, Academia Sinica), Vice-Chairman
Fagao ZHANG (Institute of Oceanology, Academia Sinica), Secretary
Zeshi CHEN (First Institute of Oceanolography, State Oceanic Administration)
Yuanbing FAN (National Natural Science Foundation of China)
Guohong FANG (Institute of Oceanology, Academia Sinica)
Zhongxin GUO (South China Sea Institute of Oceanology, Academia Sinica)
Xiuwen HAN (Department of Resources and Environment, Academia Sinica)
Ronghui HUANG (Institute of Atmospheric Physics, Academia Sinica)
Yusong SU (Ocean University of Qingdao)
Yaochu YUAN (Second Institute of Oceanography, State Oceanic Administration)
Shijin ZHAO (Institute of Oceanology, Academia Sinica)

Sponsors

Institute of Oceanology, Academia Sinica
National Natural Science Foundation of China
Department of Resources and Environment, Academia Sinica
Department of International Cooperation, State Oceanic Administration
Chinese Society of Oceanology and Limnology
LASG, Institute of Atmospheric Physics, Academia Sinica
Ocean University of Qingdao
First Institute of Oceanography, State Oceanic Administration
Second Institute of Oceanography, State Oceanic Administration
South China Sea Institute of Oceanology, Academia Sinica

Program

Sunday, May 9 **Registration**

Monday, May 10 **Opening Ceremony**

08:00	Y. QIN	Host remarks
08:10	T. TAKANO	Opening address

Special Lecture

Chairmen: Y. HSUEH/D. HU

08:30	W.S. WOOSTER	Decadal changes in the Eastern Subarctic Pacific, their origin and their possible effects on fish stocks
09:00	S.-Y. CHAO	Progress in numerical studies of the East China Sea current system in the last decade
09:30	J.-H. HU	Drifter programs in Taiwan: Studies on Kuroshio from South China Sea to East China Sea
10:00		(Coffee and Tea Break)
10:20	W.S. WOOSTER	The purpose and current status of the North Pacific Marine Science Organization (PICES)
10:50	J. SU & X. LIU	A numerical study of the winter circulation over the shelf seas adjacent to China
11:20	B.-H. CHOI	A review of tidal models for the East China and Yellow Seas
12:00		(Lunch Break)

Kuroshio and Shelf Circulation in the East China Sea

Chairmen: K. D. CHO/H. CHOI

13:30	Y. YUAN & Z. PAN	The Kuroshio in the East China Sea and the currents east of the Ryukyu Islands during autumn 1991
13:50	T. YANAGI & S. TAKAHASHI	Seasonal variation of circulation in the East China Sea and the Yellow Sea
14:10	M. SAKURAI, A. MAEDA & T. YAMASHIRO	Relation between velocity fluctuation at a site south of Nakanoshima Island and the Kuroshio front migration in the Tokara Strait
14:30	N. GOHDA, A. KANEKO, K. KAWATATE & S. MIZUNO	A countercurrent of the Kuroshio on the East China Sea shelf slope
14:50	H. ICHIKAWA, M. CHAEN & S. TAKAYA	The southward current in the western region of Kyushu
15:10	H. NAKAJIMA & A. KANEKO	Near-inertial oscillation in the Kuroshio west of Okinawa
15:30	H. PAN & F. LIU	An analytical model for steady circulation of the East China Sea
15:50	Z.Y. YANG	Tide-induced Stokes drift in the East China Sea
16:10		(Coffee and Tea Break)

Chairmen: G. FANG/J.Y. NA

16:30	Y. YUAN, J. SU & Z. PAN	A prognostic model of the Kuroshio and the eddies in the East China Sea
16:50	T.Z. YAN	An analytic model on coastal upwelling

Tsushima/Korea Strait

17:10	H.-J. LIE, C.-H. CHO & H.-R. SHIN	Origin of Tsushima Warm Current

Reception
Monday, May 10, 18:30

Tuesday, May 11
Chairmen: B.-H. CHOI/J. SU
Water Mass and Circulation in the Japan Sea (East Sea)

08:30	I. BANG, M.-S. SUK & S.-Y. NAM	Oceanographic condition of the Korea Strait
08:50	K. TAKANO	A numerical simulation of the circulation in the western North Pacific
09:10	C.-H. KIM, J.-H. YOON & J.-Y. NA	Numerical experiment on the circulation in the Japan Sea (East Sea) using a reduced gravity model
09:30	Y. H. SEUNG & K. KIM	Numerical modeling of the East (Japan) Sea circulation
09:50	C. KIM, H.-R. SHIN & S.-K. BYUN	Anticyclonic warm eddy in the western part of the East Sea (Japan Sea)
10:10		(Coffee and Tea Break)

Chairmen: K.-L. FAN/Y.-H. SEUNG

10:30	K. KIM & Y.-G. KIM	Physical properties of the North Korea Cold Water
10:50	K. KIM, Y.-K. CHO & Y.-G. KIM	Observation of the East Sea Intermediate Water in the Ulleung Basin
11:10	J.H. LEE	The vertical thermohaline structure in the southwestern East Sea
11:30	J.Y. CHUNG & K.A. PARK	SST variability in the East Sea by the satellite images
12:00		(Lunch Break)

Chairmen: S. MIZUNO/N.A. MAXIMENKO

13:30	Y. ISODA	Year-to-year variability of SST across the polar front in the Japan Sea
13:50	A. KANEKO, G. YUAN & I. NAKANO	A numerical approach to the Japan Sea acoustic tomography
14:10	H. CHOI, K.-W. KOU, Y.-K. LEE & S.N. PARK	Formation of sea fogs at the coastal stations in the passage of the East Korea Warm Current
14:30	I.K. CHUNG & M.G. KIM	Seasonal variation of photosynthetic activities and heavy metal toxicities on *Ulva pertusa* Kjellman

Water Mass and Circulation in the Yellow Sea

14:50	Y. SU	A study of water system at sea surface in the Yellow Sea
15:10	J. QI	The numerical simulation of the three-dimensional baroclinic circulation in Yellow and Bohai Seas
15:30	D.-J. KANG, K.-R. KIM, J.-Y. CHUNG, S.-H. KIM & G.H. HONG	Identification of water masses in the Yellow Sea employing ^{18}O as a tracer
15:50	S.-K. BYUN	Seaward extension of Chinese coastal water at the mouth of Yellow Sea
16:10		(Coffee and Tea Break)

Chairmen: R. HUANG/S.Y. CHAO

16:30	K. LE & Y. WANG	A study on the heat and salt transports by currents in the southern Yellow Sea in winter

Circulation and Water Temperature in the South China Sea, Taiwan Strait and East of the Philippines

16:50	D. XU & Y. YUAN	Calculation of the circulation east of the Philippines
17:10	T.-C. HUNG & CHARLEY C.H. TSAI	Upwelling phenomena off the southwestern coast of Taiwan
17:30	K.-L. FAN & H.-J. LI	A study on water temperature in Nan-Wan Bay on southern tip of Taiwan
17:50	C.-T. LIN, K.-L. FAN & S.-Y. CHAO	Small-scale plume from a semi-enclosed basin: Yen Yang Bay

Wednesday, May 12

08:00		Excursion to Laoshan Mountain

Thursday, May 13

Chairmen: A. KANEKO /Y. YUAN

08:30	S. JAN, C.-S. CHERN & J. WANG	A numerical simulation of current in Taiwan Strait during summertime

Special Lecture

08:50	R. HUANG	Impact of Asian Monsoon on the ENSO Event

Air-Sea Interaction

09:20	R. ZHANG	Coupled waves in simple tropical air-sea interaction models and their instabilities
09:40	W.T. LIU	Synergistic application of satellite data to study ocean-atomosphere interaction in the Western Pacific
10:00		(Coffee and Tea Break)

Chairmen: S. SAKAI/C.S. KIM

10:20	C.N.K. MOOERS, L. OEY, D.-S. KO & S. JIN	Circulation model development and evaluation: Possible parallels for Asia coastal seas
10:40	H.-W. LI	A method of calculating absolute geostrophic current
11:00	Y. ZHAO, Y. CHEN & L. YANG	The oceanic heat transport in the upper ocean of the western Pacific in winter

Sea Level, Tides and Tidal Current

11:20	B.-H. CHOI & J.S. KO	Modeling of tides in the East Asian Marginal Seas
11:40	Y.-S. RYU & B.-G. LEE	Numerical analysis of free harbor oscillation with finite element method
12:00		(Lunch Break)

Chairmen: C.N.K. MOOERS/T.-C. HUNG

13:30	G. FANG & D. CAO	A numerical model for tides and tidal currents in the South China Sea
13:50	J.C. LEE & B.-H. CHOI	Tidal computations for Seohan Bay
14:10	R.C. XIU & Y.H. GU	A new forecasting method for tidal flow field and the basic characteristics of tidal motion in the Bohai Sea and Huanghai Sea
14:30	J. NA & J. CHOI	Laboratory modelling of wind and tide driven circulation
14:50	T.YAMASHIRO, A.MAEDA & M. SAKURAI	Tidal current off southeast Nakano-Shima in the Tokara Strait

15:10	W.O. SONG, S.K. KANG, K.-D. YUM & S.-R. LEE	A study of tides in Jindo waterway, Korea
15:30	H. LI & G.H. FANG	Wind-driven current in Bohai Sea and Yellow Sea, using irregular grid finite difference technique

Waves, Storm Surges and Tsunami

15:50	B.-G. LEE, H.-J. KIM, K.D. CHO & H. CHOI	An application of integrated finite difference method to two-dimensional free oscillation analysis
16:10		(Coffee and Tea Break)

Chairmen: H.-W. LI/S. NAKAMOTO

16:30	P. GUO, P. SHI & H. WANG	The statistical distribution of wind speeds and significant wave heights by GEOSAT altimetry on the China Seas and the Northwestern Pacific
16:50	H. CHOI	Thermal internal boundary layer in the coastal sea under the prevailing offshore flow
17:10	C.H. HONG & J.H. YOON	The effect of typhoon on the sea level variations in the East Sea /the Japan Sea
17:30	Y.J. RO & I.K. YOU	Numerical investigation of wind driven current and their implication in pollutant dispersions in the Yellow Sea
17:50	S.K.KANG, U.-Y.CHUNG, K.-D. YUM & S.-R. LEE	A study on the tidal phenomena in the Korea Strait

Friday, May 14

Chairmen: S.-K. BYUN/A. MAEDA

08:30	J. TIAN, D. HU, F. ZHANG & Y. HOU	The study of wave breaking
08:50	J.Y. CHUNG & H.W. KANG	Mesoscale variability of the SST pattern off the east coast of Korea by the EOF analysis of AVHRR data
09:10	Y. NOH	Onset of stratification in the mixed layer subjected to stabilizing buoyancy flux

Measurement, Experiment and Data Management

09:30	S. MIZUNO, A. KANEKO, T. NAGAHAMA & K. KAWATATE	Subsurface current measurements of the Kuroshio
09:50	N.A. MAXIMENKO	A cold lens observed in the Kuroshio Extension during Megapolygon Experiment
10:10		(Coffee and Tea Break)

Chairmen: H. ICHIKAWA/Y. SU

10:30	A.MAEDA, K.KUSUHARA & T. YAMASHIRO	Velocity section measured by ADCP installed in a ferryboat regularly crossing the Kuroshio in the Tokara Strait
10:50	K.TAKANO, Y. YUAN, K.KAWATATE, S.IMAWAKI, J. SU, Z. PAN & H.ICHIKAWA	Direct current measurements at mid and abyssal depths southeast of Okinawa
11:10	S.NAKAMOTO, T.KAWANO, Y. KASHINO & K. MUNEYAMA	On turbulent mixing and parameterization with use of current meter and drifter tracking data
11:30	Y. DU	The comparison between the sea surface temperature from satellite and the SST from ship in north sea

Mixing, Stratification and Boundary Layer

11:50	B. ZHAO	Characteristics of tidal residual current and tidal mixing in the East China Sea
12:10		(Lunch Break)
Chairmen: K. KIM/R. ZHANG		
13:30	H.ICHIKAWA, K.FUJIMOTO & M. CHAEN	Benthic boundary layer current on the continental shelf edge
13:50	T. MATSUNO, S. KANARI, C.KOBAYASHI & T.HIBIYA	Bottom mixed layer near the shelf break of the East China Sea

Sedimentology and Chemistry

14:10	Y.A. PARK & K.S. CHOI	Depositional environments of the late pleistocene marine deposits off the western coast of Korea
14:30	S. SUGIOKA, T. KOJIMA & K. NAKATA	Numerical model development for oil spill in the marine environment

Special Lectures

14:50	S. SAKAI	Global oceanography from Asia
15:20		(Coffee and Tea Break)
Chairmen: W.T. LIU/J.Y.CHUNG		
15:40	Y. HSUEH	The blocking of the Kuroshio in the East China Sea
16:10	D. HU	A program on margin flux in the East China Sea

La mer (Bulletin de la Société franco-japonaise d'océanographie)
Tome 32 (1994)

Sommaire

Numéro 1

うみ（日仏海洋学会誌）
第32巻（1994年）
総　目　次

第1号

Numéro 2

Numéro 3

第2号

第3号

Numéro 4

Proceedings of the Seventh Japan and East China Seas Study Workshop

賛　助　会　員

阿　部　嘉　方	東京都練馬区春日町 2-15-6
株式会社 内田老鶴圃　内田　悟	東京都文京区大塚 3-34-3
有限会社　英和出版印刷社	東京都北区中里 2-7-7
株式会社　カイジョウ	東京都西多摩郡羽村町栄町 3-1-5
㈶ 海洋生物環境研究所	東京都千代田区内神田 1-18-12　北原ビル内
株式会社　川合海苔店	東京都大田区大森本町 2-31-8
株式会社　自然・情報環境研究所	横浜市栄区桂町 1-1，3-401
新日本気象海洋株式会社	東京都世田谷区玉川 3-14-5
全日本爬虫類皮革産業連合会	東京都足立区梅田 4-3-18
株式会社　高　岡　屋	東京都台東区上野 6-7-22
株式会社東京久栄技術センター	埼玉県川口市芝鶴ケ丸 6906-10
株式会社西日本流体技研	長崎県佐世保市棚方町 283
日本アクアラング株式会社	神奈川県厚木市温水 2229-4
㈱ 三菱総合研究所 (社会情報システム部)	東京都千代田区大手町 2-3-6
㈱　本　地　郷	東京都千代田区神田須田町 2-2-4　須田町藤和ビル７F
株式会社読売広告社	東京都中央区銀座 1-8-14
渡辺機開工業株式会社	愛知県渥美郡田原町神戸大坪 230
株式会社　渡部計器製作所	東京都文京区向丘 1-7-17

日仏海洋学会入会申込書

（正会員・学生会員）

	年度より入会	年　月　日申込
氏　名 ローマ字		年　月　日生
勤務先　住所 〒 機関名 電話		
自宅　住所 〒 電話		
紹介会員氏名		
送付金額　円	送金方法	
会誌の送り先（希望する方に○をつける）	勤務先　自宅	

（以下は学会事務局用）

受付	名簿 原簿	会費 原簿	あて名 カード	学会 記事

入会申込書送付先：〒101　東京都千代田区神田駿河台 2-3

(財)日仏会館内

日仏海洋学会

郵便振替番号：00150−7−96503

投稿の手引

1. 「うみ」（日仏海洋学会機関誌；欧文誌名 La mer）は，日仏海洋学会正会員およびそれに準ずる非会員からの投稿（依頼稿を含む）を，委員会の審査により掲載する。
2. 原稿は海洋学および水産学両分野の原著論文，原著短報，総説，書評，資料などとする。すべての投稿は，本文，原図とも正副2通とする。副本は複写でよい。本文原稿用紙はすべてA4判とし，400字詰原稿用紙（和文）に，または厚手白紙にダブル・スペース（和文ワープロでは相当間隔）で記入する。表原稿および図説明原稿は，それぞれ本文原稿とは別紙とする。
3. 用語は日，仏，英3カ国語の何れかとする。ただし，表および図説明の用語は仏文または英文に限る。原著論文（前項）には約200語の英文または仏文の要旨を，別紙として必ず添える。なお，欧文論文には，上記要旨の外に，約500字の和文要旨をも添える。ただし，日本語圏外からの投稿の和文要旨については編集委員会の責任とする。
4. 投稿原稿の体裁形式は最近号掲載記事のそれに従う。著者名は略記しない。記号略号の表記は委員会の基準に従う。引用文献の提示形式は，雑誌論文，単行本分載論文(単行本の一部引用を含む)，単行本などの別による基準に従う。
5. 原図は版下用として鮮明で，縮尺（版幅または1/2版幅）に耐えられるものとする。
6. 初校に限り著者の校正を受ける。
7. 正会員に対しては7印刷ページまでの掲載を無料とする。ただし，この範囲内であっても色彩印刷を含む場合などには，別に所定の費用を著者負担とすることがある。正会員の投稿で上記限度を超える分および非会員投稿の印刷実費はすべて著者負担（10,000円/頁）とする。
8. すべての投稿記事について，1篇あたり別刷50部を無料で請求できる。50部を超える分は請求により，50部単位で作製される。別刷請求用紙は初校と同時に配布される。
9. 原稿の送り先は下記の通り。

〒108 東京都港区港南4-5-7 東京水産大学　山口征矢 気付
日仏海洋学会編集委員会

1994年11月25日 印刷
1994年11月28日 発行

うみ　第32巻 第4号

定価 ¥1,600

編集者　山口征矢
発行所　日仏海洋学会
財団法人 日仏会館内
東京都千代田区神田駿河台2-3
郵便番号：101
電話：03(3291)1141
振替番号：00150-7-96503
印刷者　佐藤一二
印刷所　㈲英和出版印刷社
東京都北区中里2—7—7
郵便番号：114
電話：03(5394)4856

(本誌出版費の一部は平成5年度文部省科学研究費補助金「研究成果公開促進費」による.)
Publication of La mer has been supported in part by a Grant-in-Aid for Publication of Scientific Research Result from the Ministry of Education, Science and Culture, Japan.

Tome 32 N° 4

SOMMAIRE

Proceedings of the Seventh Japan and East China Seas Study Workshop